Spatially Resolved Infrared Spectroscopy For Spintronics

Christopher Stephen Kelley

Doctor of Philosophy

University of York
Physics

February 2014

Abstract

Magnetoresistance, a change in the resistance of a material in an externally applied magnetic field, is an extremely important property of magnetic materials. The discovery of giant magnetoresistance has led to a revolution in computing, driving increases in storage density of hard disks and paving the way for commerical spintronic devices. Conventionally, magnetoresistance is measured by sourcing a current through a material and measuring the voltage. Ohm's law is used to calculate the resistance of the material with and without an external magnetic field, the difference between these results being the magnetoresistance. This technique is limited as it does not offer spatial resolution, so variations in magnetoresistance in a material can not be detected. Electrical contact must also be made to the material, which can cause damage to the material being measured. The magnetorefractive effect, the change in the reflection spectrum of a material in an external magnetic field, can be used as an alternative to the electrical measurement of magnetoresistance. The magnetorefractive effect allows non-contact measurements of magnetoresistance to be made, so the material remains undamaged, whilst also offering the possibility of spatial resolution. Modelling the spectral magnetorefractive effect can also aid in understanding the underlying physical mechanism behind the magnetoresistance, which is impossible with an electrical measurement. Infrared reflection microspectroscopy was used to observe variations in reflectivity across Fe_3O_4 thin films. By modelling these variations, it was possible to estimate the chemical composition of the samples as well as observe any variations in composition across them. A spatial variation in magnetoresistance was observed across a CoFe/Cu multilayer using the magnetorefractive effect, whilst also obtaining the spectral resolution necessary to model the system, the first time such a measurement has been performed. The correlation between the magnetorefractive effect and magnetoresistance had been predicted to be strong in the far-infrared by previous theoretical work. The magnetorefractive effect in the far-infrared was measured for a series of spin valves, demonstrating this strong correlation in the far-infrared for the first time, providing long awaited experimental confirmation of this theoretical prediction.

Contents

List of Tables

List of Figures

Acknowledgements

I have thoroughly enjoyed my time studying in York, so much so that I decided to do it twice. My decision to stay was primarily thanks to (or the fault of, depending on who you speak to) Prof. Mike Bentley, my undergraduate supervisor. Cheers Mike, I hope I didn't give you too much of a headache and I've done you proud. The students in the group in 2010 when I started were fantastic in helping me settle in to the new experience of full time academia, in particular Dr. James Naughton, who was exceptionally patient during my conversion from astrophysicist to nanophysicist. I would also like to thank Dr. "Handy" Andy Vick for his ability to fix anything and everything and his example of calmness under pressure, it helped us all. Prof. Jim Matthew also deserves a special mention, for taking time from his retirement to regularly see me and read through my papers and talks. Your insight was always valuable and meetings with you were always fun, thanks for all your help. I would like to thank all the students who I ever shared an office with, especially Daniel Gilks and James Sizeland who helped me enormously with TEM and VSM measurements. I had a great time working with you and I wish you all well for the future. Thanks also go to the staff in the group, especially Drs. Steve Tear, Andrew Pratt, Siew Wai Poon and Vlado Lazarov, who have helped me along the way. I'd also like to thank all the other students, the admin staff and anyone else I might have missed, you were all fantastic.

This work would not have been possible without a great deal of technical expertise. The mechanical workshop in York were fantastic in helping me build my electromagnet, in particular John Clapham, who took on a lot of the work. I would also like to acknowledge the contributions of Drs. Paul Dumas and Stéphane LeFrançois from the SMIS beamline at the SOLEIL synchrotron. Without their technical expertise this thesis would not exist. Their exceptional hospitality has led me to go career in the world of synchrotron physics,

merci beacoup mes amis!

Thanks to my Mum, for convincing me to take physics instead of psychology at A-level. Ever supportive and always there to help. My family have always been there to look after me, Tony, Richard, Matt and James, cheers guys! Finally, I thank my supervisor Prof. Sarah Thompson, for giving me the opportunity to work with her. I'm not sure if Sarah's patience is genuinely infinite but I never found the limit! Her guidance and support were always delivered with a smile and I will miss working with her, hopefully there will be possibility for collaboration in the future.

Declaration

The research presented in this doctoral thesis is the work of the author, Christopher Stephen Kelley, except where explicitly acknowledged or referenced in the text, in accordance with the examination regulations of the University of York. A list of publications based on research in this thesis is below.

Kelley, C. S., Thompson, S. M., Poon, S-W., Matsuzaki, K., LeFrançois, S., Hosono, H., Susaki, T. and Dumas, P. "Mapping Spatial Variations in Iron Oxide Phases in Magnetite Thin Films Using Infrared Reflectance Microspectroscopy." *Manuscript in preparation* - Chapter 5

Kelley, C. S., Thompson, LeFrançois S. and Dumas, P. "Experimental Confirmation of a Strong Correlation Between the Magnetorefractive Effect and Giant Magnetoresistance in the Far Infrared." *Manuscript in preparation* - Chapter 7

Kelley, C. S., Naughton, J., Benson, E., Bradley, R. C., Lazarov, V. K., Thompson, S. M., Matthew, J. A. D. "Investigating the Magnetic Field Dependent Conductivity in Magnetite Thin Films by Modelling the Magnetorefractive Effect." *J. Phys.: Condens. Matter* **26** 036002 (2014) - Chapter 4

Kelley, C. S.,Thompson, S. M., Illman, M. D., LeFrançois, S., and Dumas, P. "Spatially Resolving Variations in Giant Magnetoresistance, Undetectable With Four-Point Probe Measurements, Using Infrared Microspectroscopy." *Appl. Phys. Lett.* **101**(16) 2402 (2012) - Chapter 6

Presentations

Oral Presentations

3/11/2013 - 8/11/2013: 58th Conference on Magnetism and Magnetic Materials, Denver, USA

"Mapping Spatial Variations in Iron Oxide Phases in Magnetite Thin Films Using Infrared Reflectance Microspectroscopy."

3/11/2013 - 8/11/2013: 58th Conference on Magnetism and Magnetic Materials, Denver, USA

"Infared Remote Sensing of Giant Magnetoresistance: Experimental Confirmation of a Strong Correlation Between the Magnetorefractive Effect and Giant Magnetoresistance in the Far Infrared."

30/10/2011 - 3/11/2011: 56th Conference on Magnetism and Magnetic Materials, Scottsdale, USA

"Spatially Resolved Remote Sensing of Giant Magnetoresistance Using an Infrared microscope."

21/9/2011: Current Research in Magnetism 2011, Durham, UK

"Spatially Resolved Remote Sensing of Magnetoresistance Using the Magnetorefractive Effect."

Poster Presentations

10/6/2013 - 12/6/2013: 2nd York-Tohoku Symposium, York, UK

"Spatially Resolved Probing of Giant Magnetoresistance Using Non-Contact Infra-Red Remote Sensing Techniques."

27/6/2011 - 29/6/2011: 1st York-Tohoku Symposium, York, UK

"Spatially Resolved Remote Sensing of Magnetoresistance Using an Infrared Microscope."

14/12/2010 - 16/12/2010: Condensed Matter and Materials Physics 2010, Warwick, UK

"The Magnetorefractive Effect in Thin Films of Fe_3O_4/MgO(111)."

Chapter 1

Introduction

1.1 Why do we want to build spintronic devices?

Spintronics has become a well established research area in the field of condensed matter physics[1,2,3,4,5,6]. Spintronics involves controlling and manipulating the intrinsic spin angular momentum of electrons, as well as their charge, in order to create devices that have properties and perform functions that are impractical (or impossible) with conventional electronics. Quicker, more energy efficient computers with increased functionality are on the horizon. Advances in spintronics such as spin qubits[7] in spin quantum computation, spin diodes[8], spin quantum field effect transistors[9] and reprogrammable magnetic logic are all exciting, active frontiers of research in modern computing. Spintronics has already been commercially successful for the data storage industry. The discovery of giant magnetoresistance (GMR), and the subsequent development of GMR based magnetic read heads for computer hard drives, drove the increase in areal density of data storage at the beginning of the 21st century. Intensive research in magnetic storage continues today, primarily focusing on spin transfer torque magnetic random access memory (STT-MRAM)[10], racetrack memory[11] and heat assisted magnetic recording (HAMR)[12].

1.2 Giant magnetoresistance (GMR)

GMR is a large change in a material's electrical resistivity in the presence of an applied external magnetic field, an effect discovered independently by Albert Fert[13] and Peter Grünberg[14] for which they shared the 2007 Nobel prize in physics[15]. Materials which

display magnetic order necessarily have a density of states which is distinct for each spin carrier at the Fermi level. It is useful to treat the two spin carriers independently as two separate current channels[16], this is a good approximation as long as the spin relaxation length is sufficiently long so that the spin of each carrier is preserved when passing through the material. Spin up and spin down electrons have different scattering probabilities in a magnetic material as the density of states at the Fermi energy is different for up and down spins in magnetic materials. The simplest type of system that exhibits GMR is a magnetic bilayer consisting of two layers of a ferromagnetic material separated by a non-magnetic spacer layer. This system can exist in either a parallel or antiparallel state as shown in figure 1.1a[17].

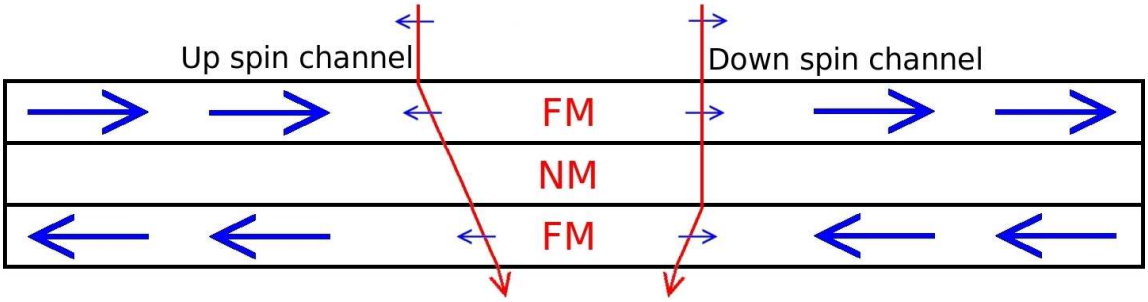

(a) Ferromagnetic layers aligned antiparallel

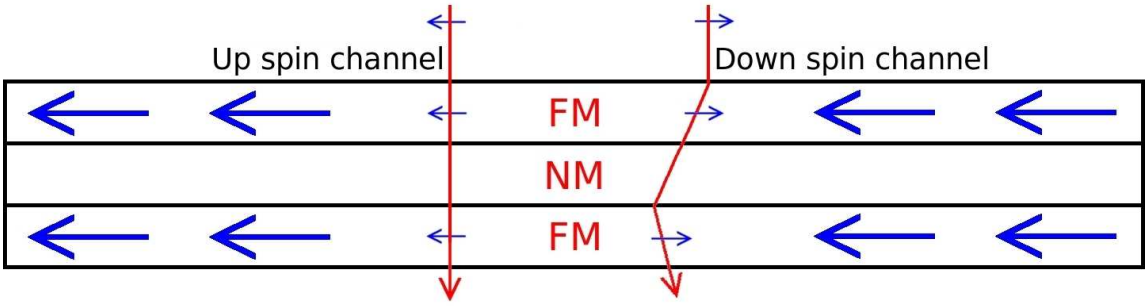

(b) Ferromagnetic layers aligned parallel

Figure 1.1: There is a difference in scattering between an antiparallel and a parallel alignment. In the antiparallel case the up spin channel and down spin channel experience a similar degree of scattering but in the parallel case the up spin channel dominates the conductivity as the down spin electrons experience an increased degree of scattering.

When a current is passed through the material in the antiparallel state as in figure 1.1b, both spin channels have an equal resistance as both experience an increase in scattering in one of the layers. In this situation neither spin carrier dominates the resistivity. Defining $\rho^{\uparrow}$ as the up spin channel resistivity and $\rho^{\downarrow}$ as the down spin conductivity, the resistivity of the antiparallel arrangement is:

$$\rho_{\text{ap}} = \frac{\rho^{\uparrow} + \rho^{\downarrow}}{2} \tag{1.1}$$

If the current is passed through the material in the parallel state as in figure (1.1a) then one of the spin carriers experiences an increased degree of scattering at both layers while the other carrier is subject to a much reduced quantity of scattering. In this instance the resistivity is dominated by the spin carrier which has experienced the least scattering, the overall resistivity of the material has decreased:

$$\rho_{\text{p}} = \frac{2\rho^{\uparrow}\rho^{\downarrow}}{\rho^{\uparrow} + \rho^{\downarrow}} \tag{1.2}$$

The difference between the two resistivities is often expressed as a ratio:

$$\text{GMR} = \frac{\Delta\rho}{\rho} = \frac{\rho_{\text{ap}} - \rho_{\text{p}}}{\rho_{\text{p}}} = \frac{(\rho^{\downarrow} - \rho^{\uparrow})^2}{4\rho^{\uparrow}\rho^{\downarrow}} \tag{1.3}$$

There are many areas where GMR is used in spintronics, including development of magnetic random access memory[18], magnetoresistive sensors[19], magnetometers[20] and for spin injection[21].

1.3 The magnetorefractive effect (MRE)

The magnetorefractive effect (MRE) is a magneto-optical technique used to probe the magnetotransport properties of magnetic materials[22]. It uses the fact that a material's reflectivity is determined by its complex dielectric function, which is in turn determined by the material's optical conductivity. If a material exhibits magnetoresistance, its conductivity changes with the applied magnetic field. If the conductivity of the material is changing, this should therefore be measurable as a variation in the reflectivity spectrum of the material. This variation in reflectivity with externally applied magnetic field, the MRE, was first observed experimentally by Jacquet and Valet in NiFe/Cu/Co/Cu multilayers[23]. The MRE can therefore be used as a non-contact optical technique for the remote sensing of magnetoresistance. Since this initial observation, the MRE has been used to probe the magnetoresistance of materials such as magnetite[24], manganites[25], Fe/Cr superlattices[26]

and granular materials[27].

The magnetoresistance of a material is usually measured by performing an electrical four-point probe measurement[28], a technique which has two main limitations. Firstly, it is extremely difficult to routinely obtain spatial resolution with a four-point probe measurement, as the contact pins have to be thick enough ($\sim$1 mm) to not buckle under the pressure of being pressed against the sample surface with springs. This makes any measurement of the MR of a sample an average over several millimetres of the sample. The MRE has previously been shown to be able to provide spatial resolution, by measuring the variation in emissivity (rather than reflectivity) of CoFe/Cu and Co/Cu multilayers in the presence of an externally applied magnetic field[29]. The second problem is the physical damage and potential surface contamination to the sample caused by the spring loaded contacts. As the MRE is non-contact, it can remotely probe the MR of a material quickly, without causing any contamination or damage to the sample, with the potential to be performed *in situ* after deposition of the material[30]. It is also possible to model the spectral MRE of magnetic materials, which can reveal information about the physical mechanism of the MR in the material[31] that is impossible to obtain with an electrical measurement. Attempts have been made to correlate the MRE and MR in an effort to use the MRE to quantitatively determine the MR, with some success.

1.4 Aims of this thesis

This doctoral thesis ultimately aims to demonstrate the utility of the MRE as a measure of the MR of a magnetic material. Spatially resolved MRE experiments will be demonstrated for the first time, whilst also collecting the necessary spectral information to probe the underlying MR mechanisms, which is impossible with current methods of measuring the MR. The ability to characterise these parameters is critical for the development of GMR materials for use as spin injectors, especially Fe_3O_4 as it is predicted to be an ideal spin injector. It is first necessary to be able to obtain reflectivity spectra of magnetic materials and to be able to accurately model these spectra. In chapter 4, simulated reflection spectra of a series of Fe_3O_4 thin films are produced and compared to their experimental analogues. With the ability to obtain experimental reflection spectra, as well as the ability to simulate the spectra, the spatial variation in reflectivity across different Fe_3O_4 thin films was measured using an IR microscope. In chapter 5, these infrared microspectroscopy results are

used to probe the spatial variation in chemical composition across each sample. A variation in composition will result in a variation in MR, giving insight into the growth quality of each of the films. With the ability to measure spatial variations in reflectivity demonstrated, spatial variations in MRE, and therefore MR, were probed with the IR microscope. In chapter 6, a bespoke electromagnet was used with the IR microscope to perform magnetic field-dependent reflection spectroscopy measurements. A CoFe/Cu multilayer was annealed to create a gradient in MR across the sample, which was subsequently detected as a gradient in MRE across the sample. This is the first time a spatially and spectrally resolved MRE measurement has been attempted, allowing both the variation in MR across the multilayer to be observed as well as providing insight into the physical origin of the underlying MR mechanism. The MR and MRE are linked in the mid-IR by a correlation factor, which is obtained from information of the MRE spectral shape, material parameters and fitting parameters. In the far-IR, this correlation is predicted to be much simpler, dependent only on material parameters. In chapter 7, MRE spectra in the mid and far-IR of a series of spin valves with different MR are used to experimentally confirm this theoretical prediction for the first time.

Chapter 2

Theory of the MRE and the Link to Spin-Dependent Electron Transport in Magnetic Materials

2.1 Physical properties of magnetic materials

The magnetic materials studied in this thesis are Fe_3O_4 thin films, CoFe/Cu multilayers and CoFeGe based spin valves. Fe_3O_4 is predicted to be half-metallic, making it an ideal spin injector. This makes it an excellent candidate material for building spintronic devices. CoFe/Cu multilayers have a very high MR, making it easier to detect variations in MR across the sample. Spin valves switch in a very low field, making them ideal for studies where strong magnetic fields are difficult to achieve, as is the case in the experiments detailed in this thesis. The behaviour of these material systems is examined in detail in the following sections.

2.1.1 Physical properties of Fe_3O_4

Fe_3O_4 single domain particles have the highest remanent magnetisation of any naturally occurring magnetic material, leading to Fe_3O_4 being the first magnetic material to be discovered by ancient civilisations[32]. It is named for Magnesia in northern Greece, the site of its discovery by the ancient Greeks. Fe_3O_4 has the inverse spinel structure[33] shown in figure 2.1. This is a face centred cubic (FCC) O^{2-} lattice with Fe^{3+} ions filling 1/8 of the available tetrahedral sites. Half of the remaining octahedral lattice sites are occupied, there are an equal number of Fe^{2+} and Fe^{3+} ions occupying these sites. The average charge on

the octahedral sites is $Fe^{2.5+}$ as the Fe^{3+} ions exchange electrons with their Fe^{2+} neighbours. The Fe_3O_4 unit cell comprises four $\{100\}$ planes which between them contain all of the O^{2-} and octahedral ions, while the tetrahedral ions are halfway between the planes[34].

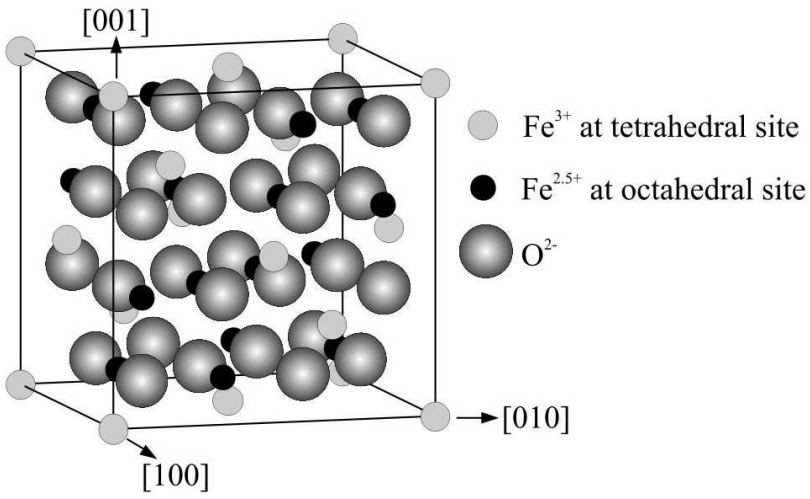

Figure 2.1: Diagram showing the inverse spinel structure of Fe_3O_4. The O^{2-} ions are arranged in an FCC structure, whilst the $Fe^{2.5+}$ ions display octagonal symmetry and the Fe^{3+} ions display tetragonal symmetry. Image courtesy of Wilma Eerenstein[35].

The lattice constant of Fe_3O_4 is 8.397 Å[36] and MgO has a lattice constant of 4.212 Å, which is almost exactly half that of Fe_3O_4. MgO has the rocksalt structure, so two MgO unit cells will share a common O^{2-} FCC sub-lattice with Fe_3O_4, with a very low lattice mismatch of -0.3%[37]. There is therefore little strain at the interface facilitating almost perfect epitaxial growth of Fe_3O_4 films on MgO substrates.

In ordered magnetic materials, the unpaired electron spins align parallel (ferromagnetism) or antiparallel (antiferromagnetism) in order to minimise the exchange energy[38]. The ions in Fe_3O_4 are separated by too great a distance for the exchange interaction to propagate and align the electron spins, so another exchange mechanism is required. This extra energy minimisation arises from superexchange[39]. In the ground state, the 2p orbital of the O^{2-} ion is filled and can exchange electrons with the partially filled 3d orbitals in the neighbouring $Fe^{2.5+}$ or Fe^{3+} ions. This leads to an indirect exchange coupling across the O^{2-} ion which leads to antiferromagnetic ordering between unpaired electrons on the $Fe^{2.5+}$ and Fe^{3+} ions. As these ions have differing numbers of electrons this leads to imperfect cancellation of the electron magnetic moments. Hence, Fe_3O_4 exhibits ferrimagnetic behaviour. Superexchange also makes it difficult for an external magnetic field to couple

to the electron magnetic moments, resulting in the very high (>100 kOe) saturation field of Fe_3O_4 [40].

The band structure of ordered magnetic materials is split at the Fermi energy, E_F, such that one spin carrier has a greater number of occupied states at E_F [41]. The band structure of these materials is said to be spin polarised. Fe_3O_4 is of particular interest as the bulk band structure is predicted theoretically to be 100% spin polarised at E_F [42,43], materials with this property are called half-metals as the conduction is of only one type of spin carrier. This is a vital material property as it allows the possibility of injecting a 100% spin polarised current into a non-magnetic material, which is particularly important for devices based on tunnel magnetoresistance (TMR). TMR, first discovered by Julliere[44], occurs when two ferromagnetic layers are separated by a thin insulating layer in a magnetic tunnel junction (MTJ). The probability of tunnelling through the gate oxide is dependent on whether the layers are parallel or antiparallel, one having a low resistance and the other having a very high resistance. The TMR ratio is dependent on the spin polarisation, P, in each of the ferromagnetic layers[45]:

$$\text{TMR} = \frac{2P_1P_2}{1 - P_1P_2} \tag{2.1}$$

where the spin polarisation in each ferromagnetic layer is dependent on the density of states at E_F in each layer:

$$P = \frac{D^{\uparrow}(E_F) - D^{\downarrow}(E_F)}{D^{\uparrow}(E_F) + D^{\downarrow}(E_F)} \tag{2.2}$$

For Fe_3O_4, $P_1 = P_2 = 1$ as there are only down spin states available to occupy at E_F. For a perfect MTJ, this would result in one state with low resistance and one with an infinite resistance, resulting in extremely high MR values. Experimentally, MR values in excess of 500% have been observed in an Fe_3O_4/MgO/Fe_3O_4 MTJ[46]. However, previous research[47] suggests that the band structure is not 100% polarised at the interface which is critical in thin films. The degree of spin polarisation is critically dependent on the crystal direction of the substrate as this determines the termination plane of Fe_3O_4 at the interface which leads to different spin polarisations. Efficient spin injection is an important precursor to the construction of many spintronic devices such as spin transistors and magnetic logic gates, so the ability to deposit high quality Fe_3O_4 thin films is crucial

if it is to be used in these types of devices.

2.1.2 Physical properties of CoFe/Cu multilayers and CoFe/Cu based spin valves

Rapid advances in GMR materials have been made since Fert and Grünberg first demonstrated the effect for Fe/Cr multilayers. CoFe/Cu is currently more widely used for GMR multilayer structures and is the basic structure of the multilayers considered in this thesis. Alloying cobalt and iron reduces the saturation field of the magnetic layers, allowing them to reverse in lower fields, whilst also safeguarding against thermal instability[48]. For hard disk applications, this is useful as it allows a lower write field to be used, reducing the energy cost of writing bits in a hard disk, making it more efficient if it used as a storage medium. Copper is used as a non-magnetic spacer as it is does not alloy well with cobalt or iron[49], maintaining sharp interfaces.

CoFe/Cu has been used as the basis of spin valves, materials with the structure antiferromagnet/pinned ferromagnet/non-magnetic spacer/free ferromagnet[50]. The antiferromagnet pins the magnetisation of the ferromagnetic layer it is in contact with, preventing its magnetisation from reversing in low magnetic fields. This pinning creates exchange anisotropy, causing an asymmetric hysteresis loop[51], a phenomenon referred to as exchange bias in contemporary literature[52]. The free ferromagnetic layer magnetisation may reverse in an externally applied magnetic field. This allows a system to be engineered where a very small external magnetic field is required to switch the system from a very high resistance to a very low resistance, making them ideal for hard drive applications[53]. There has been a push for current-perpendicular-to-plane (CPP) GMR rather than current-in-plane (CIP) GMR, as the CPP GMR was shown to be double the CIP GMR in a CoFe/Cu multilayer[54]. Recently, it has been shown that introducing germanium into a spin valve increases its CPP GMR, whilst reducing its CIP GMR[55].

2.2 Theory of the MRE

The MRE makes use of the conductivity dependence of the complex dielectric function of a material to probe changes in MR. In this section, the origin of this conductivity dependence is explored and is used to define expressions for the MRE in terms of the emissivity

and reflectivity of a material. Finally, the finer details of how the theory behind the MRE in the reflection geometry is implemented into the MRE models that were developed during this work is discussed.

2.2.1 Response of dielectric materials to IR radiation

When IR radiation is incident on a dielectric material, the electrons in the material experience an excitation due to the electromagnetic field of the propagating photons. The electric field generated in the material by the incoming photons is oscillatory, giving rise to a harmonic oscillator electric field, $\mathbf{E}(\omega, t)$, of the form[56]:

$$\mathbf{E}(\omega, t) = \Re\left[|\mathrm{E}| \exp\left(i\omega t\right)\right] \tag{2.3}$$

Where ω is the angular frequency of the incident radiation and *t* denotes the time-dependence. The effect of the magnetic field is insignificant in this non-relativistic limit and is neglected. This electric field results in an oscillatory displacement of the electrons in the material about their lattice sites, characterised by a displacement field $\mathbf{D}(\omega, t)$:

$$\begin{aligned} \mathbf{D}(\omega, t) &= \epsilon_0 \epsilon(\omega) \mathbf{E}(\omega, t) && (2.4) \\ &= \epsilon_0 \epsilon(\omega) \Re\left[|\mathrm{E}| \exp\left(i\omega t\right)\right] && (2.5) \end{aligned}$$

Where ϵ_0 is the vacuum permittivity and $\epsilon(\omega)$ is the dielectric function of the material. The conductivity of the material, σ, now depends on the oscillatory nature of the electric field and therefore must be (in general) complex. An expression for the complex dielectric function, $\epsilon^*(\omega)$, in terms of σ can be derived from the Maxwell-Ampère law:

$$\begin{aligned} \nabla \times \mathbf{H} &= \mathbf{J_d} + \mathbf{J_f} = \mu_0 \mathbf{J} && (2.6) \\ &= \frac{\partial \mathbf{D}(\omega, t)}{\partial t} + \sigma \cdot \mathbf{E}(\omega, t) && (2.7) \end{aligned}$$

The first term, $\mathbf{J_d}$, represents the current density due to the displacement field generated by the incoming photons while the second term, $\mathbf{J_f}$, is the current density of free conduction

electrons. **J** represents the total current density in the material and μ_0 is the vacuum permeability. Substituting the expression for the displacement field into the Maxwell-Ampère law and performing the differentiation yields:

$$\nabla \times \mathbf{H} = i\omega\epsilon_0\epsilon(\omega)\cdot\mathbf{E}(\omega,t) + \sigma\cdot\mathbf{E}(\omega,t) \quad (2.8)$$

$$= [\sigma + i\omega\epsilon_0\epsilon(\omega)]\cdot\mathbf{E}(\omega,t) \quad (2.9)$$

$$= \sigma^*(\omega)\cdot\mathbf{E}(\omega,t) \quad (2.10)$$

Where $\sigma^*(\omega)$ is the total complex a.c. conductivity. $\epsilon^*(\omega)$ may now be defined in terms of the real (d.c.) dielectric function and an imaginary conductivity contribution:

$$\epsilon^*(\omega) = \epsilon(\omega) - \frac{i\sigma}{\omega\epsilon_0} \quad (2.11)$$

The complex dielectric function can now be used to calculate the MRE in the reflection and emission geometries. There are many different conduction mechanisms so the exact form of $\epsilon^*(\omega)$ depends on the material being considered. A description of the various methods of conduction that were considered is given in section 2.4, where their implementation into different MRE models is discussed in detail.

2.2.2 The link between resistivity and emissivity

The emissivity as a function of wavelength, ϵ_λ, is defined as the radiated intensity from the material, I_λ, to that of a black body at the same temperature, $I_{\lambda,\mathrm{b}}$[57]:

$$\epsilon_\lambda = \frac{I_\lambda}{I_{\lambda,\mathrm{b}}} \quad (2.12)$$

If $\epsilon_\lambda = 1$, then the object is a blackbody and the true temperature of the object, T_{true}, is the same as the temperature observed, T_{obs}. However, $\epsilon_\lambda < 1$ in general, so $T_{\text{true}} \neq T_{\text{obs}}$. The intensity of the emitted radiation is given by the Stefan-Boltzmann law, from which the following expressions are derived:

$$I_\lambda = A\sigma\left(T_{\text{obs}}^4 - T_0^4\right) \tag{2.13}$$

$$I_{\lambda,\text{b}} = A\sigma\left(T_{\text{true}}^4 - T_0^4\right) \tag{2.14}$$

where A is the area of the emitting body, σ is the Stefan-Boltzmann constant, T_{obs} is the temperature observed by the IR camera, T_{true} is the actual temperature of the emitter and T_0^4 is the ambient temperature of the laboratory. It has been assumed that there is perfect radiative coupling and that the emission is normal to the sample. If the emissivity is a function of a magnetic field, expressions for the emissivity at two different fields, $\epsilon_\lambda(\mathbf{H}_{0/1})$, can be deduced:

$$A\sigma\left[T_{\text{true}}^4 - T_0^4\right]\epsilon_\lambda(\mathbf{H}_0) = A\sigma\left[T_{\text{obs}}^4(\mathbf{H}_0) - T_0^4\right] \tag{2.15}$$

$$A\sigma\left[T_{\text{true}}^4 - T_0^4\right]\epsilon_\lambda(\mathbf{H}_1) = A\sigma\left[T_{\text{obs}}^4(\mathbf{H}_1) - T_0^4\right] \tag{2.16}$$

The percentage difference in emissivity between the two fields, MRE$\%$, can then be calculated:

$$\text{MRE}\% = \frac{\epsilon_\lambda(\mathbf{H}_0) - \epsilon_\lambda(\mathbf{H}_1)}{\epsilon_\lambda(\mathbf{H}_1)} \times 100\% = \frac{T^4(\mathbf{H}_0) - T^4(\mathbf{H}_1)}{T^4(\mathbf{H}_1) - T_{\text{obs}}^4} \times 100\% \tag{2.17}$$

In general, there is a correlation factor, γ, linking the MRE to the MR. If the form of γ is known, then it is possible to measure a variation in conductivity as a variation in the emissivity of a material.

$$\text{MR}(\%) = \gamma \times \text{MRE}(\%) \tag{2.18}$$

2.2.3 The link between resistivity and reflectivity

If a black body is in thermal equilibrium with its environment, then its emissivity is equal to its absorptivity, α. The absorptivity of a material is related to its reflectivity, R, and its transmissivity, T, as[58]:

$$\epsilon_\lambda = \alpha = 1 - R - T \tag{2.19}$$

The reflectivity of a material is determined by its complex dielectric function, $\epsilon^*(\omega)$[57]:

$$R = \left(\frac{\sqrt{\epsilon^*(\omega)} - 1}{\sqrt{\epsilon^*(\omega)} + 1}\right)\left(\frac{\sqrt{\epsilon^*(\omega)} - 1}{\sqrt{\epsilon^*(\omega)} + 1}\right)^* \tag{2.20}$$

$\epsilon^*(\omega)$ is dependent on the conductivity, σ, of the material:

$$\epsilon^*(\omega) = \epsilon(\omega) - \frac{i\sigma}{\epsilon_0\omega} \tag{2.21}$$

As σ is the optical conductivity, changes in the conductivity can lead to measurable changes in the reflection spectra of the material. The percentage difference between the reflectivity in two magnetic fields, MRE$(\%)$, is defined as:

$$\text{MRE}(\%) = \frac{R(\mathbf{H}_0) - R(\mathbf{H}_1)}{R(\mathbf{H}_1)} \times 100\% \tag{2.22}$$

The correlation between the change in conductivity and the change in reflectivity with magnetic field is defined in the same way as for the emission geometry, although the correlation factor will be different:

$$\text{MR}(\%) = \gamma \times \text{MRE}(\%) \tag{2.23}$$

Reflection MRE measurements are performed using mid-far infra-red radiation as in this wavelength regime the photons cause *intra*band rather than *inter*band transitions, allowing only the conduction electrons (which can be treated as a nearly free electron cloud) to contribute. This is important as these electrons are responsible for the magnetism of the material, so exciting electrons out of this band affects the magnetic behaviour of the material which is undesirable. The skin depth of metals is $\sim$10 nm in this regime, for metallic films $>$10 nm this means the reflection is primarily from the film which is desirable. For oxides and metallic films $<$10 nm the reflection from the substrate must be accounted for.

2.3 Modelling the MRE of metallic multilayers

In MR metallic multilayer films, structures and devices the dominating conductivity contribution is Drude metallic conduction. The Jacquet-Valet model[59] of multilayer reflections may be used to model the MRE provided the spin-dependent Drude conductivities, $\sigma^{\uparrow/\downarrow}$, are in the self-averaging limit (SAL). $\sigma^{\uparrow/\downarrow}$ are in the SAL if the average spin-independent electronic mean free path is far longer than the average distance between spin-selective scattering sites such as interfaces and defects in the magnetic lattice. If this condition is met, the average electron travels through several layers of the multilayer before experiencing a spin-selective scattering event, so the global conductivity process can be assumed to be independent of any local variations in scattering potential in the multilayer. The Drude conductivity is therefore:

$$\sigma^{\uparrow/\downarrow} = \frac{Ne^2\tau_{\mathrm{SAL}}}{m} \tag{2.24}$$

The key material parameters that will determine the conductivity in the multilayer are the average carrier number density across the multilayer, N, and the SAL scattering time, τ_{SAL}. N is calculated by taking the individual carrier number densities of each layer and taking a weighted mean, with the layer thickness as the weighting factor. τ_{SAL} is calculated from the scattering times in the ferromagnetic (τ_{FM}) and non-magnetic (τ_{NM}) layers as well as an interfacial contribution, τ_{i}. Each scattering time is weighted by the relative concentration of ferromagnetic (c_{FM}) and non-magnetic (c_{NM}) material in the multilayer. An interfacial concentration, c_{i}, representing the area between layers where the behaviour is not bulk-like, is summed in parallel with the magnetic and non magnetic layer contributions to give an expression for τ_{SAL}:

$$\tau_{\mathrm{SAL}} = \left(\frac{c_{\mathrm{FM}}}{\tau_{\mathrm{FM}}} + \frac{c_{\mathrm{NM}}}{\tau_{\mathrm{NM}}} + \frac{c_{\mathrm{i}}}{\tau_{\mathrm{i}}}\right)^{-1} \tag{2.25}$$

Although dependent on τ_{FM} and c_{FM}, τ_{SAL} itself is spin-independent. The spin dependence is introduced into a modified τ_{SAL} by weighting the contributions of the ferromagnetic layer and the interfacial region according to the spin polarisation in the bulk ferromagnet and the interfaces respectively. This is done by introducing a bulk spin asymmetry coefficient, β, as well as an interface spin asymmetry coefficient, γ. The overall spin asymmetry coefficient, β_{SAL}, is given by the weighted τ_{SAL}:

$$\beta_{\mathrm{SAL}} = \tau_{\mathrm{SAL}} \left[\beta \left(\frac{c_{\mathrm{FM}}}{\tau_{\mathrm{FM}}} \right) + \gamma \left(\frac{c_{\mathrm{i}}}{\tau_{\mathrm{i}}} \right) \right] \tag{2.26}$$

As the spin-dependence is contained within β_{SAL}, it is this parameter that will eventually contribute to the MRE.

β_{SAL} and τ_{SAL} are then used to calculate the real and imaginary parts of the dielectric function of the material in zero field and an applied field. The dielectric functions consist of two terms. Firstly, the static dielectric constant, ε_{∞}, which determines the high frequency response of the material. The second term is a Drude conductivity term dependent on $\beta_{\mathrm{SAL}}/\tau_{\mathrm{SAL}}$ and the fraction of saturation magnetisation ($\mathbf{m}_{\mathrm{s}}$) in the two applied magnetic fields between which the greatest change in resistance is expected, $m_{0/1}$. The Drude term is also dependent on the plasmon frequency, ω_{p}, which is dependent on N as well as the angular frequency of the incident IR radiation which gives the wavelength dependence. The real and imaginary parts of the dielectric function in the magnetic field, $\Re\left[\epsilon(\omega, \mathbf{H}_{0/1})\right]$ and $\Im\left[\epsilon(\omega, \mathbf{H}_{0/1})\right]$, can be expressed as follows:

$$\Re\left[\epsilon(\omega, \mathbf{H}_{0/1})\right] = \epsilon_{\infty} - \frac{\omega_{\mathrm{p}}^2 \tau_{\mathrm{SAL}}^2 \left(1 + \omega_{\mathrm{p}} \tau_{\mathrm{SAL}}^2 + m_{0/1} \beta_{\mathrm{SAL}}^2\right)}{\left(1 - \omega_{\mathrm{p}} \tau_{\mathrm{SAL}}^2 + m_{0/1} \beta_{\mathrm{SAL}}^2\right)^2 + 4\omega^2 \tau_{\mathrm{SAL}}^2} \tag{2.27}$$

$$\Im\left[\epsilon(\omega, \mathbf{H}_{0/1})\right] = \frac{\frac{\omega_{\mathrm{p}} \tau_{\mathrm{SAL}}}{\omega} \left(1 + \omega_{\mathrm{p}} \tau_{\mathrm{SAL}}^2 + m_{0/1} \beta_{\mathrm{SAL}}^2\right)}{\left(1 - \omega_{\mathrm{p}} \tau_{\mathrm{SAL}}^2 + m_{0/1} \beta_{\mathrm{SAL}}^2\right)^2 + 4\omega^2 \tau_{\mathrm{SAL}}^2} \tag{2.28}$$

These dielectric functions can be used to calculate the reflectivity spectra in s and p polarisation in each field, $R_{\mathrm{s/p}}(\mathbf{H}_{0/1})$. The MRE is calculated from these reflectivity spectra, as shown in equation 2.29.

$$\mathrm{MRE}\% = \frac{[R_{\mathrm{s}}(\mathbf{H}_0) - R_{\mathrm{s}}(\mathbf{H}_1)] + [R_{\mathrm{p}}(\mathbf{H}_0) - R_{\mathrm{p}}(\mathbf{H}_1)]}{[R_{\mathrm{s}}(\mathbf{H}_1) - R_{\mathrm{p}}(\mathbf{H}_1)]} \times 100\% \tag{2.29}$$

2.4 Modelling the MRE of iron oxide thin films

2.4.1 Constructing the Fe_3O_4 and MgO dielectric functions

Modelling the MRE of Fe_3O_4 is more complicated than modelling metallic multilayers as the Drude conductivity is not the dominant conduction mechanism across the whole

wavelength regime. The dielectric function is built from all of the contributing conductivity processes, which are discussed in the following section. Fe_3O_4 is not a very good conductor so the skin depth is very long, leading to significant reflection from the substrate. It is therefore necessary to incorporate the dielectric function of the MgO substrate into the model and consider how the radiation reflected from the substrate interacts with the radiation reflected from the film.

Deriving the Drude contribution to the Fe_3O_4 dielectric function

There are four conductivity processes in Fe_3O_4; Drude conduction, hopping conduction, increased conduction due to d-s transitions and increased conduction around phonon resonances. Following equation (2.11), the dielectric function takes the following form:

$$\epsilon_{Fe_3O_4} = \epsilon_\infty + \epsilon_{\text{Drude}} + \epsilon_{\text{phonon}} + \epsilon_{\text{ds}} + \epsilon_{\text{hopping}} \tag{2.30}$$

Where ϵ_∞ is a material constant representing the real, high frequency dielectric response of Fe_3O_4. The form of the a.c. Drude conductivity can be obtained from Ohm's law[60]:

$$\mathbf{J} = \sigma\mathbf{E} = -Ne\mathbf{v} \tag{2.31}$$

The equation of motion is found by substituting in the d.c. Drude conductivity from equation 2.24 and taking $\mathbf{v}$ to be the time derivative of the electron displacement from equilibrium, $\dot{\mathbf{r}}$:

$$\begin{aligned} -Ne\mathbf{v} &= \frac{Ne^2\tau}{m}\mathbf{E} \\ \frac{m}{\tau}\dot{\mathbf{r}} &= -e\mathbf{E} \end{aligned} \tag{2.32}$$

This equation relates the damping ($\gamma = \tau^{-1}$) to the force exerted on the electron by an external electric field. The photon electric field is oscillatory, therefore the equation of motion can be approximated as a forced, damped harmonic oscillator driven by a time-varying electric field:

$$m\ddot{\mathbf{r}} + m\gamma\dot{\mathbf{r}} + m\omega_0^2\mathbf{r} = -e|\mathrm{E}|\exp\left[i\left(\omega t - \mathbf{k}\cdot\mathbf{r}\right)\right] \tag{2.33}$$

It is assumed that the electron motion is non-relativistic allowing the negligible magnetic effects of the time-varying electric field to be ignored. The form of the electric field can be simplified by making the assumption that the average displacement of an electron is far smaller than the wavelength of the incident radiation ($r \ll \lambda, \mathbf{r}\cdot\mathbf{k} \ll 1$) leading to an expression of the form:

$$m\ddot{\mathbf{r}} + m\gamma\dot{\mathbf{r}} + m\omega_0^2\mathbf{r} = -e|\mathrm{E}|\exp\left(i\omega t\right) \tag{2.34}$$

Making the additional assumption that the electric field in the material is isotropic ($\mathbf{E}||\mathbf{r}$) reduces the problem to one dimension:

$$\frac{\partial^2 r(t)}{\partial t^2} + \gamma\frac{\partial r(t)}{\partial t} + \omega_0^2 r(t) = -\frac{e}{m}|\mathrm{E}|\exp\left(i\omega t\right) \tag{2.35}$$

To obtain a steady state expression for $r(t)$ it is required that the driving force dominates the motion of the electrons, that is that the period of oscillation is much faster than the average scattering time. In this limit, the solution to the differential equation is the simple harmonic motion solution:

$$r(t) = A\exp\left(i\omega t\right) \tag{2.36}$$

$$\frac{\partial r(t)}{\partial t} = i\omega A\exp\left(i\omega t\right) = i\omega r(t) \tag{2.37}$$

$$\frac{\partial^2 r(t)}{\partial t^2} = i^2\omega^2 A\exp\left(i\omega t\right) = -\omega^2 r(t) \tag{2.38}$$

Substituting in the derivatives leads to the following expression:

$$\left(-\omega^2 + i\gamma\omega + \omega_0^2\right)\mathbf{r}(t) = -\frac{e}{m}\mathbf{E}(t) \tag{2.39}$$

Calculating the time derivative of this equation and rearranging for $\mathbf{v}(t)$:

$$\mathbf{v}(t) = \left[-\frac{e}{m}\frac{i\omega}{\omega_0^2 - \omega^2 + i\gamma\omega}\right]\mathbf{E}(t) \tag{2.40}$$

The equation of motion is recovered if both sides of the equation are multiplied by $-\widetilde{N}e$, where $\widetilde{N}$ is the number of electrons displaced by the electric field, so that the Drude conductivity modified for the oscillatory electric field is given by:

$$\sigma = \frac{\widetilde{N}e^2}{m}\frac{i\omega}{\omega_0^2 - \omega^2 + i\gamma\omega} \tag{2.41}$$

This directly leads to the complex dielectric function of the material in an external, time-varying electric field:

$$\epsilon^*(\omega) = \epsilon(\omega) + \frac{1}{\epsilon_0}\frac{\widetilde{N}e^2}{m}\frac{1}{\omega_0^2 - \omega^2 + i\gamma\omega} \tag{2.42}$$

This expression can be rewritten in terms of the electron plasma frequency, $\omega_{\mathrm{p}}^2 = \frac{\widetilde{N}e^2}{m\epsilon_0}$, which is a measure of how effective the screening of the conduction electrons is due to the electrons oscillating in the electric field:

$$\epsilon^*(\omega) = \epsilon(\omega) + \frac{\omega_{\mathrm{p}}^2}{\omega_0^2 - \omega^2 + i\gamma\omega} \tag{2.43}$$

By making the assumption that the band conduction is relatively flat and therefore resonance free ($\omega_0 = 0$), rearranging leads to the form of the Drude dielectric function used in the MRE models used in this thesis:

$$\epsilon^*(\omega) = \epsilon(\omega) - \frac{\omega_{\mathrm{p}}^2}{\omega^2 - i\gamma\omega} \tag{2.44}$$

$$\epsilon_{\mathrm{Fe_3O_4}} = \epsilon_\infty + \epsilon_{\mathrm{Drude}} \tag{2.45}$$

Deriving the d-s transition, phononic and hopping contributions to the Fe_3O_4 dielectric function

As discussed previously, Fe_3O_4 is not a good conductor. When deriving the form of the Drude contribution to the dielectric function, the assumption was made that the band structure is flat and that there are no resonances. Modifications to the dielectric function have to be made to account for contributions to the conductivity from resonant sources, in this case

from phonons and the d-s transition. The conductivity can be increased due to electron-phonon scattering at certain frequencies that are dependent on the bonding energies between different atoms in the Fe_3O_4 film. These phonon resonances are introduced into the dielectric function as Lorentz oscillators:

$$\epsilon_{\text{phonon}} = \sum_{\text{j=1}}^{\text{n}} \frac{S_{\text{j}}\omega_{\text{j}}^2}{\omega_{\text{j}} - \omega^2 - i\gamma_{\text{j}}\omega_{\text{j}}} \tag{2.46}$$

where S_{j} is the strength, ω_{j} is the resonant frequency and γ_{j} the collisional damping factor of the j-th resonance. There is also an overlap of the 3d and 4s bands on the Fe^{2+} sites. There is a resonance in the conductivity as electrons oscillate between the more conducting 4s band and the less conducting 3d band, known as the d-s transition, which can also be modelled as a Lorentz oscillator:

$$\epsilon_{\text{ds}} = \sum_{\text{j=1}}^{\text{n}} \frac{S_{\text{j-ds}}\omega_{\text{j-ds}}^2}{\omega_{\text{j-ds}} - \omega^2 - i\gamma_{\text{j-ds}}\omega_{\text{j-ds}}} \tag{2.47}$$

It is also possible for electrons to tunnel between Fe^{2+} and Fe^{3+} lattice sites. These electrons couple with phonons to form polarons that "hop" between the octahedral sites causing an increase in the conductivity. Modelling the polaron hopping conductivity is a difficult quantum mechanical problem and it is usually estimated from a large set of fitting parameters (such as those produced by Degiorgi *et al.*[61]). Ahn *et al.* have shown that the hopping conductivity is reasonably constant ($\sim 500\,\Omega^{-1}\text{cm}^{-1}$) in the near/mid-IR[62]. The hopping contribution to the dielectric function can be estimated as follows:

$$\epsilon_{\text{hopping}} = -\frac{4\pi}{i\omega\epsilon_0}\sigma_{\text{hopping}} \tag{2.48}$$

$$= -\frac{7.1 \times 10^{14}}{i\omega} \tag{2.49}$$

Thus, the full MgO and Fe_3O_4 dielectric functions are:

$$\epsilon_{\text{MgO}} = \epsilon_\infty + \epsilon_{\text{phonon}} \tag{2.50}$$

$$= \epsilon_{\infty_{\text{MgO}}} + \sum_{\text{j=1}}^{\text{n}} \frac{\text{S}_{\text{j}_{\text{MgO}}}\omega_{\text{j}_{\text{MgO}}}^2}{\omega_{\text{j}_{\text{MgO}}}^2 - \omega^2 - i\gamma_{\text{j}_{\text{MgO}}}\omega_{\text{j}_{\text{MgO}}}} \tag{2.51}$$

$$\epsilon_{Fe_3O_4} = \epsilon_\infty + \epsilon_{\text{Drude}} + \epsilon_{\text{phonon}} + \epsilon_{\text{ds}} + \epsilon_{\text{hopping}} \tag{2.52}$$

$$= \sum_{j=1}^{n} \frac{S_{j_{Fe_3O_4}} \omega^2_{j_{Fe_3O_4}}}{\omega^2_{j_{Fe_3O_4}} - \omega^2 - i\gamma_{j_{Fe_3O_4}} \omega_{j_{Fe_3O_4}}} \tag{2.53}$$

$$+ \sum_{j=1}^{n} \frac{S_{j\text{-}ds_{Fe_3O_4}} \omega^2_{j\text{-}ds_{Fe_3O_4}}}{\omega^2_{j\text{-}ds_{Fe_3O_4}} - \omega^2 - i\gamma_{j\text{-}ds_{Fe_3O_4}} \omega_{j\text{-}ds_{Fe_3O_4}}}$$

$$+ \epsilon_{\infty_{Fe_3O_4}} - \frac{\omega_p^2}{\omega^2 - i\gamma\omega} - \frac{7.1 \times 10^{14}}{i\omega}$$

2.4.2 Combining the MgO and Fe_3O_4 dielectric functions to model the MRE

Using the Fresnel equations, it is possible to determine the s and p polarisation reflection coefficients using the dielectric functions defined by equations 2.51 and 2.53:

$$r_s = \frac{\cos\varphi - \sqrt{\epsilon(\omega) - \sin^2\varphi}}{\cos\varphi + \sqrt{\epsilon(\omega) - \sin^2\varphi}} \tag{2.54}$$

$$r_p = \frac{\epsilon(\omega)\cos\varphi - \sqrt{\epsilon(\omega) - \sin^2\varphi}}{\epsilon(\omega)\cos\varphi + \sqrt{\epsilon(\omega) - \sin^2\varphi}} \tag{2.55}$$

where φ is the angle of incidence of the IR radiation with respect to the normal. The total reflectivity is the average of the s and p polarisation reflectivities:

$$R = \frac{|r_s|^2 + |r_p|^2}{2} \tag{2.56}$$

Equation 2.56 can be used to calculate the reflectivity from the surface of the Fe_3O_4 and from the MgO. It is also necessary to consider the effects of interference between reflections from the MgO/Fe_3O_4 interface and the Fe_3O_4 surface. The interference of the two reflections will be dependent on the thickness of the Fe_3O_4 film, the thickness of the MgO is assumed to be sufficiently large that there is no reflection from the bottom of the substrate. The total reflectivity, inclusive of the interfered reflections, can be obtained by following the procedure of McIntyre[63] and defining the following φ-dependent quantities:

$$\xi_j = \sqrt{\epsilon_j - \epsilon_1 \sin^2\varphi} \tag{2.57}$$

where j=1 for air, j=2 for Fe_3O_4 and j=3 for MgO as shown in the schematic in figure 2.2. ϵ_j is the complex dielectric function of the j-th phase.

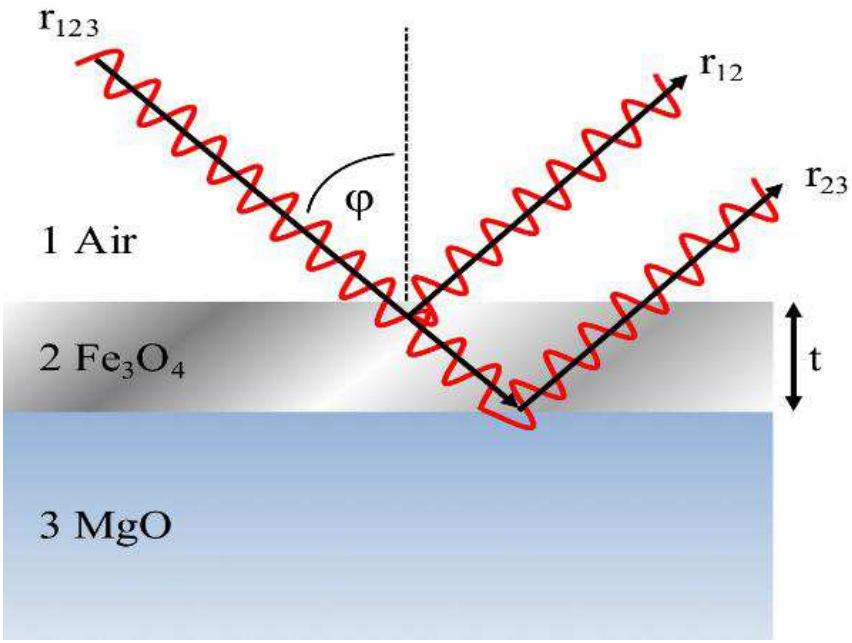

Figure 2.2: A schematic illustrating the three-phase system used in order to model the reflectivity for thin films of Fe_3O_4/MgO. The thickness of the film is t and the angle of incidence as defined from the normal is φ. The three phases are air (j=1), the Fe_3O_4 thin film (j=2) and the MgO substrate (j=3). Image courtesy of Dr. James Naughton.[64]

The reflectivity between two neighbouring phases j and k in s and p polarisation can now be determined from the Fresnel equations:

$$r_{s/jk} = \frac{\xi_j - \xi_k}{\xi_j + \xi_k} \tag{2.58}$$

$$r_{p/jk} = \frac{\epsilon_k \xi_j - \epsilon_j \xi_k}{\epsilon_k \xi_j + \epsilon_j \xi_k} \tag{2.59}$$

The influence of the magnetic field of the incident radiation is neglected as the magnetic permeabilities in the near-IR are assumed to be unity. The total reflectivity including the interfered reflections in s and p polarisation, as a function of the wavelength of the incident radiation, is:

$$r_{s/123} = \frac{r_{s/12} + r_{s/23}\exp(2i\beta)}{1 + r_{s/12}r_{s/23}\exp(2i\beta)} \tag{2.60}$$

$$r_{p/123} = \frac{r_{p/12} + r_{p/23}\exp(2i\beta)}{1 + r_{p/12}r_{p/23}\exp(2i\beta)} \tag{2.61}$$

where:

$$\beta = \frac{2\pi\xi_2 t}{\lambda} \tag{2.62}$$

The total reflectivity is again the average of the reflectivity in s and p polarisation:

$$R_{123} = \frac{|r_{s/123}|^2 + |r_{p/123}|^2}{2} \tag{2.63}$$

As $t \ll \lambda$, the expression can be simplified by assuming that the attenuation of the electric field caused by the exponential term is linear in the near-IR. Taking the second order Taylor expansion of the exponential term in equations 2.60 and 2.61 results in:

$$r_{s/123} = \frac{r_{s/12} + r_{s/23}(1 + 2i\beta)}{1 + r_{s/12}r_{s/23}(1 + 2i\beta)} \tag{2.64}$$

$$r_{p/123} = \frac{r_{p/12} + r_{p/23}(1 + 2i\beta)}{1 + r_{p/12}r_{p/23}(1 + 2i\beta)} \tag{2.65}$$

The Fresnel coefficients for three layer systems are related to the reflection coefficients of the substrate in the absence of the film in s and p polarisation, $r_{s/13}$ and $r_{p/13}$:

$$r_{s/13} = \frac{r_{s/12} + r_{s/23}}{1 + r_{s/12}r_{s/23}} \tag{2.66}$$

$$r_{p/13} = \frac{r_{p/12} + r_{p/23}}{1 + r_{p/12}r_{p/23}} \tag{2.67}$$

Dividing equations 2.64 and 2.65 by 2.66 and 2.67 respectively gives the following expressions:

$$\frac{r_{\text{s/123}}}{r_{\text{s/13}}} = \frac{1+2i\beta\left(\frac{r_{\text{s/23}}}{r_{\text{s/12}}+r_{\text{s/23}}}\right)}{1+2i\beta\left(\frac{r_{\text{s/12}}r_{\text{s/23}}}{r_{\text{s/12}}+r_{\text{s/12}}r_{\text{s/23}}}\right)} \tag{2.68}$$

$$\frac{r_{\text{p/123}}}{r_{\text{p/13}}} = \frac{1+2i\beta\left(\frac{r_{\text{p/23}}}{r_{\text{p/12}}+r_{\text{p/23}}}\right)}{1+2i\beta\left(\frac{r_{\text{p/12}}r_{\text{p/23}}}{r_{\text{p/12}}+r_{\text{p/12}}r_{\text{p/23}}}\right)} \tag{2.69}$$

Taylor expanding the denominator to second order in β and rearranging leads to expressions for the reflectivity of the interfered system in s and p polarisation:

$$r_{\text{s/123}} = r_{\text{s/13}}\left[1+\frac{4\pi i t\xi_1}{\lambda}\left(\frac{\xi_2^2-\xi_3^2}{\xi_1^2-\xi_3^2}\right)\right] \tag{2.70}$$

$$r_{\text{p/123}} = r_{\text{p/13}}\left\{1+\frac{4\pi i t\xi_1}{\lambda}\left(\frac{\epsilon_2}{\epsilon_1}\right)\left[\frac{\left(\frac{\xi_2}{\epsilon_2}\right)^2-\left(\frac{\xi_3}{\epsilon_3}\right)^2}{\left(\frac{\xi_1}{\epsilon_1}\right)^2-\left(\frac{\xi_3}{\epsilon_3}\right)^2}\right]\right\} \tag{2.71}$$

Averaging the contributions of the s and p polarisations using equation 2.63 gives the total reflectivity spectrum of the system. Taking reflection spectra at the two fields between which there is the greatest change in resistance, $R_{123}(\mathbf{H}_{0/1})$, gives the MRE of the system:

$$\text{MRE}\% = \frac{R_{123}(\mathbf{H}_0)-R_{123}(\mathbf{H}_1)}{R_{123}(\mathbf{H}_1)}\times 100\% \tag{2.72}$$

The field dependence, which is discussed in greater detail in chapter 4, is introduced as a factor of $(1+\eta h^2)$ in $R_{123}(\mathbf{H}_1)$, where h represents the change in resistance of the material and η is a fitting parameter.

Chapter 3

Experimental Techniques

In this chapter the experimental techniques used to obtain and validate data presented in this thesis are described. Firstly, sample preparation by molecular beam epitaxy is presented. This is followed by a detailed experimental description of probing GMR through electrical measurements and the MRE in the reflection and emission geometries, examining the relative merits of each technique. Different experimental procedures for synchrotron based infrared radiation experiments are highlighted and bespoke equipment and programs that were developed to facilitate those experiments are described. Finally, other relevant thin-film characterisation methods that were used alongside the main techniques are briefly outlined.

3.1 Deposition of iron oxide films by molecular beam epitaxy (MBE)

The magnetic thin films made for collecting data for this thesis were grown in the Department of Physics at York using molecular beam epitaxy (MBE) unless otherwise stated. MBE involves the very slow evaporation of metals onto a substrate so that a thin film of metal is built up, ideally, a monolayer at a time, facilitating good epitaxial growth, in ultra-high vacuum (UHV). UHV conditions are necessary to minimise the number of contaminant molecules present which may mix with the metals being deposited, compromising the uniformity of the film and introducing unwanted defects. The base pressure within the MBE chamber is held below $\sim 1 \times 10^{-10}$ mbar by a turbomolecular vacuum pump backed by a rotary vacuum pump, as well as a titanium sublimation pump and a liq-

uid nitrogen cryopump. The pressure is monitored at various points around the chamber, a schematic of which is given in figure 3.1. The pressure just before the turbomolecular pump at the base of the chamber is monitored using a cold cathode gauge, the pressure at the fast entry lock (FEL) is measured with a Penning gauge and the pressure in the main body of the chamber is monitored by an ion gauge.

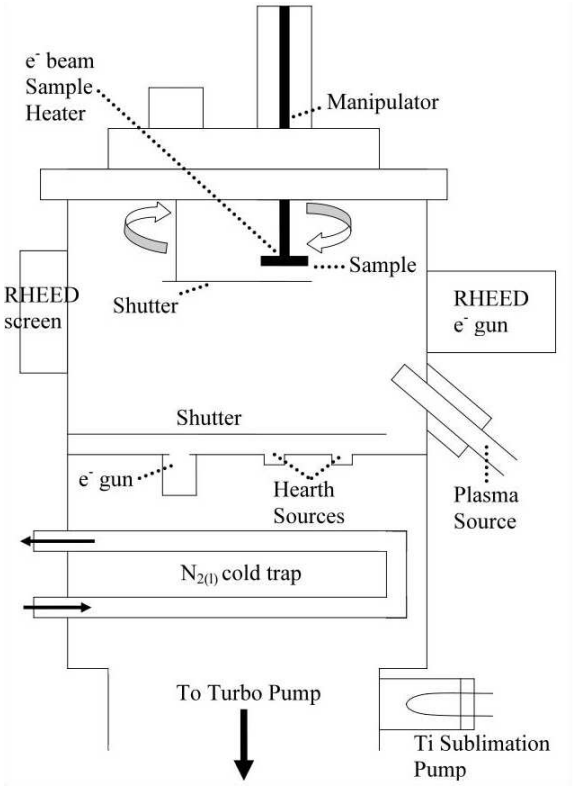

Figure 3.1: Schematic diagram of the MBE system, showing the location of some of the key equipment on the chamber including the turbomolecular pump, manipulator and sample location. The iron metal target is located in the hearth closest to the Balzers electron gun. The FEL and sample insertion arm are not shown. Image courtesy of Dr. James Naughton[64].

The metals are evaporated onto the substrate by direct heating using heat from passing current through a tungsten filament and by electron beam heating. Electron beam heating requires a high voltage to be placed on the tungsten heating filament whilst earthing the source metal. When enough current is passed through the filament, the electrons acquire enough energy to overcome the work function of the tungsten and are accelerated into the source metal crucible, causing rapid heating leading to evaporation of the metal. The metal atoms then settle on the substrate forming the film. The rate of evaporation, and therefore deposition of metal, can be controlled by varying the current in the tungsten filament and the high voltage at which the filament is held. A schematic diagram is given in figure

3.2. A slow deposition rate on the order of $1\,\text{Å s}^{-1}$ is required in order to allow the metal atoms to rearrange themselves to form monolayers producing uniform, defect free films. Sometimes it is necessary to heat the substrate in order to give the atoms enough energy to rearrange themselves, or to allow a particular stoichiometry or surface reconstruction to form. Sample heating is via direct heating and electron beam heating of the sample holder which in turn heats the substrate, up to a maximum of $\sim 1500\,^{\circ}\text{C}$. The system is currently equipped to evaporate iron, silver, gold and magnesium oxide, although these could readily be exchanged to allow deposition of other metals.

It is possible to determine how much metal has been deposited using a quartz ratemeter crystal. The crystal is piezoelectric and is vibrating at its natural frequency. The frequency of vibration is proportional to the mass of the crystal, so as metal is deposited on the crystal it is possible to measure the variation in the vibrational frequency of the crystal in order to estimate the film thickness. The ratemeter has separate calibration settings for each source, accounting for the density of the metal as well as the distance and angle from the source.

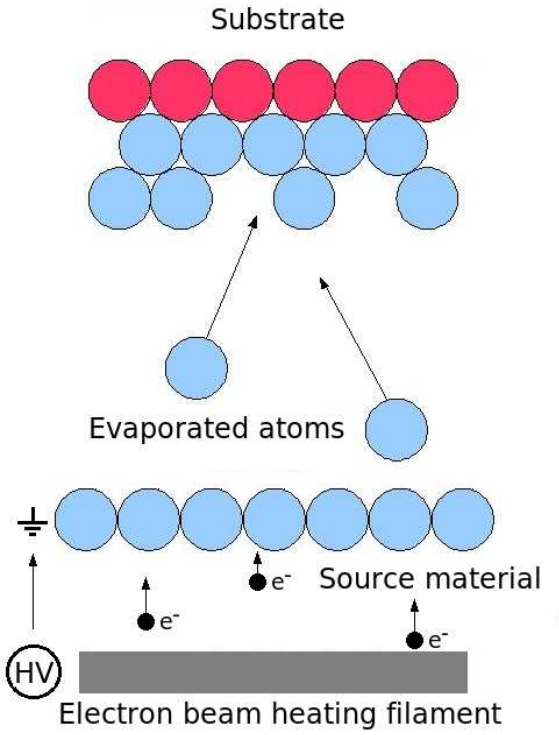

Figure 3.2: Schematic diagram of the basic principle of electron beam evaporation. Using a high voltage supply, an electron beam is accelerated into the source material. This evaporates the target metal which deposits onto the surface of the substrate.

Substrates are introduced into the vacuum through the FEL, which is separated from the main chamber with a gate valve. This allows the FEL to be vented to atmosphere without contaminating the vacuum in the main chamber. Once at atmospheric pressure, the FEL can be pumped separately to the main chamber by a secondary turbomolecular pump until the pressure has equalised and the gate valve can be opened. Substrates are transferred into the manipulator using an insertion arm, controlled externally using permanent magnets. The manipulator allows translational motion of the sample perpendicular to the sample plane, allowing the substrate to be moved from the insertion position to a predetermined growth position. The manipulator can rotate $360\,^\circ$ in the sample plane whilst allowing $\sim 45\,^\circ$ rotation out of the sample plane.

3.1.1 Growing Fe_3O_4 by MBE

Fe_3O_4 can be grown either by simultaneous oxidation or post oxidation. In simultaneous oxidation, Fe_3O_4 is grown epitaxially by co-deposition with atomic oxygen produced by an oxygen plasma source or diatomic oxygen introduced into the chamber via a leak valve. The iron deposited on the substrate reacts with the oxygen and oxidises, forming one of the phases of iron oxide. In the case of post-oxidation, a film of pure iron is deposited and is subsequently annealed in an oxygen rich environment. The surface of the film oxidises first, then the oxygen diffuses through the film, oxidising the iron in a self-limiting fashion[65]. Which oxide is produced depends on many factors including oxygen partial pressure, iron deposition rate and substrate temperature. The annealing time is an important factor for post-oxidation whilst the oxygen plasma power is important if using the plasma source for simultaneous oxidation. The difficulty arises as Fe_3O_4 can only be grown under very specific conditions. The phase diagram for iron oxide is complex as shown in figure 3.3 and any deviation from the growth conditions can cause the formation of a non-Fe_3O_4 phase. Growing Fe_3O_4 requires great precision in the growth parameters in order to achieve a uniform, epitaxial film with few defects.

The oxygen plasma source uses an RF coil to to break up molecular oxygen gas into atomic oxygen, oxygen ions and electrons. A high voltage bias deflector plate at the end of the source is used to trap the ions and electrons so only a beam of atomic oxygen leaves the source. Parameters that were varied to try and determine optimum growth conditions were the deposition rate of iron, oxygen partial pressure, the substrate temperature, the

annealing time and temperature for post-oxidation and the RF power when using the oxygen plasma source. Due to the self-limiting nature of the oxidation during post-oxidation, Fe_3O_4 films can only be grown to a thickness of ~ 3 nm whereas films that are hundreds of nanometres thick can potentially be grown by simultaneous oxidation.

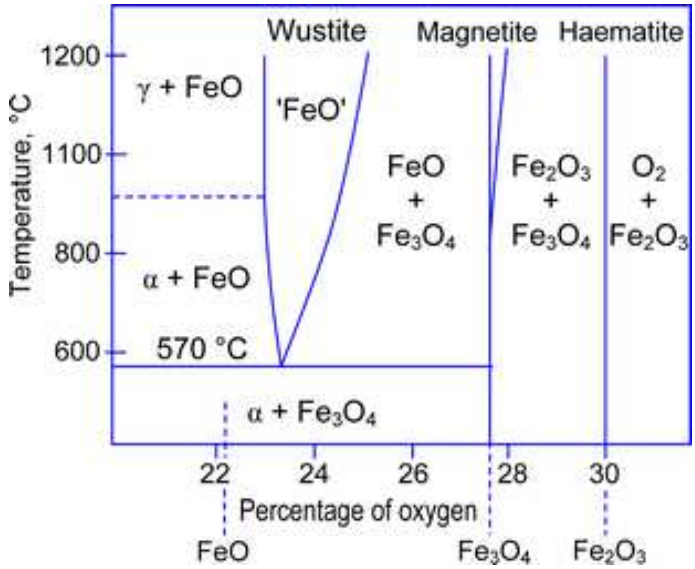

Figure 3.3: Phase diagram of iron oxide[66]. Fe_3O_4 exists in a non-mixed phase state in only a very small region between ∼900-1500 °C and $\sim 27.5 - 28.5\%$ composition of oxygen by weight, where 1500 °C is the approximate boiling point of iron oxide at these oxygen compositions[67]. The conditions of growth must therefore be accurately determined and tightly controlled in order to grow good thin films of Fe_3O_4.

3.2 Four-point probe measurements

3.2.1 Measuring GMR with an electrical four-point probe

The GMR of a material can be observed by performing a direct electrical measurement using a four-point probe. The probe has two current contacts and two voltage contacts which are tungsten spring-loaded pins sharpened to a point and held against the sample surface. A Keighley power supply is used to pass a constant current through the sample material, typically of the order $1\,\text{mA} - 1\,\mu\text{A}$, through two of the pins. The remaining two pins are used to detect the voltage across the sample as shown in figure 3.4. Having separate current and voltage pins, rather than sourcing current and sensing voltage through the same pins, gives more accurate measurements. This is because the voltage sensing circuit is now independent of the current source circuit so the impedance from that circuit

and the resistance in the contacts is eliminated from the measurement. Using the sensed voltage and sourced current the resistance of the film can be determined using Ohm's law.

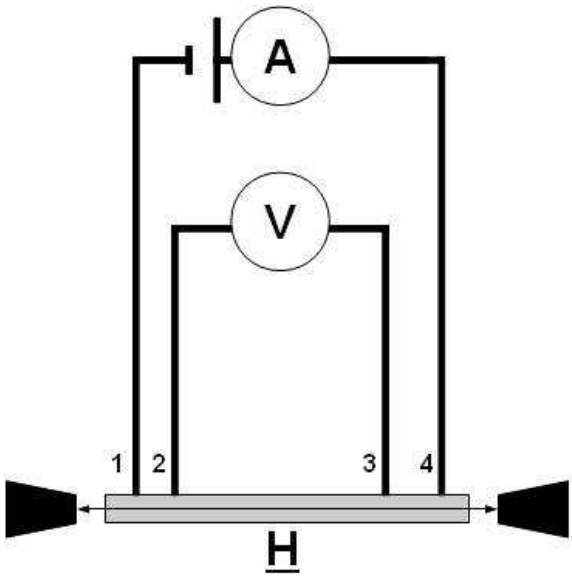

Figure 3.4: Schematic diagram of an electrical GMR measurement. The voltage sensed at pins 2 and 3 is independent of the impedence contribution from the constant current source circuit and its contact resistance. The net direction of electron travel is in the sample plane and there is little opportunity for spatial resolution.

A thin film that exhibits MR undergoes a change in resistivity in an applied field which can be detected as a change in resistance in an applied field. The difference between the resistance in an applied field, $R(\mathbf{H}_1)$, and the resistance in another applied field, $R(\mathbf{H}_2)$, is commonly expressed as a percentage change as in equation 3.1. A measurement is performed by sweeping the electromagnet through a full hysteresis loop. This allows a plot of percentage change in MR with applied field to be made. An example four-point probe MR curve for a GMR material is given in figure 3.5. For most materials, the greatest change in resistance is achieved by measuring the difference between the resistance at the saturation field and zero applied field. However, in materials that are exchange biased (such as spin valves), the greatest change in resistance is observed by taking the difference in resistance on either side of the switch of the free magnetic layer.

$$\text{GMR}(\%) = \frac{\Delta R}{R(\mathbf{H}_1)} \times 100\% = \frac{R(\mathbf{H}_2) - R(\mathbf{H}_1)}{R(\mathbf{H}_1)} \times 100\% \tag{3.1}$$

It is important to note that as all four pins are on the surface of the sample this technique is only sensitive to the current-in-plane (CIP) contribution to the GMR. Four-point

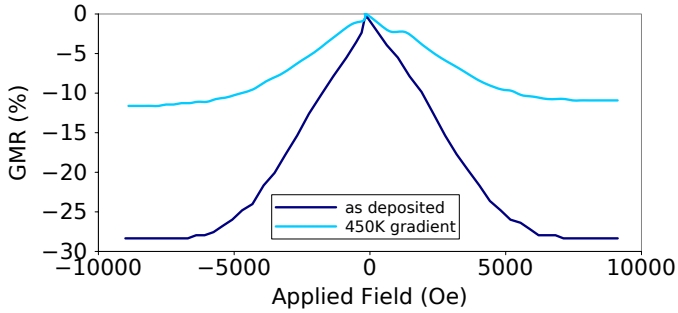

Figure 3.5: Typical GMR curves showing percentage change in GMR with applied magnetic field. For these curves $\mathbf{H}_1 = 0\,\text{Oe}$ and $\mathbf{H}_2 = 9000\,\text{Oe}$.

probe measurements offer little to no spatial resolution as the diameter of the pins and their separation distance leads to the measurement being performed over an area of several millimetres. This is a typical thin film sample size; the measurement is necessarily averaging over a significant volume of the sample.

3.3 Measuring the MRE

According to equation 2.19, the MRE can be measured in three different geometries; emission, reflection and transmission. In each case IR radiation is used to measure the change in the complex dielectric function, and therefore conductivity, of a material in an externally applied magnetic field. The MRE measurements presented in this thesis were performed in the emission and reflection geometries. The techniques and equipment used to measure the MRE in these geometries are discussed in the following sections.

3.3.1 Measuring the MRE through emissivity with an IR camera

In the emission geometry, the change in conductivity of a material in an externally applied magnetic field is measured as a change in the emissivity of the material in the applied field. The change in emissivity results in a variation in the apparent temperature of the sample with the external field. A thermal imaging camera is used to collect a map of apparent temperature across the sample in two different fields, $T(\mathbf{H}_1)$ and $T(\mathbf{H}_2)$. The MRE can now be calculated, providing the ambient temperature of the laboratory (T_0) is known. The GMR and MRE are related by a correlation factor, γ, using equation 3.2[68].

$$\begin{aligned} \text{MRE}\% &= \frac{T(\mathbf{H}_2)^4 - T(\mathbf{H}_1)^4}{T(\mathbf{H}_1)^4 - T_0^4} \times 100\% \\ \text{MRE}\% &= \gamma \times \text{GMR}\% \end{aligned} \tag{3.2}$$

For many systems, one of the fields is usually 0 Oe. It is extremely difficult to create an environment where there the external magnetic field is truly 0 Oe because of the field due to the remanent magnetisation of the electromagnet and stray fields from other electronic equipment. This leads to increased uncertainties in measurements performed at or near 0 Oe. If there is little variation in MRE in the low field regime then this effect is not important. However, if the sample has a sharp MR curve that varies significantly in low fields, then a large error can become associated with the measurement. A number of repeat spectra (25 for IR camera measurements) are obtained to minimise this error.

The sample is attached to an ohmic heating pad using thermal paste and placed between the pole pieces of an electromagnet. A bespoke heater is used to maintain a constant sample temperature in the range $\sim 35 - 40\,^{\circ}$C. At this temperature the sample thermally emits IR radiation which is collected in the CCD of a Jenoptik Varioscan 3021 IR camera, which is sensitive to radiation in the wavelength range $8-12$ μm. The camera is positioned at normal incidence to the sample at a distance of 65 cm. 25 images of the temperature distribution across the sample are taken and are averaged to create a time averaged map of temperature across the sample in two different fields. Care needs to be taken to ensure that the electromagnet is used to take the sample through its saturation magnetisation (or the highest fraction possible) when switching between the fields in order to minimise hysteretic effects and provide reproducibility. The thermal images are imported into a Python program (written by the author) which strips out the raw data, performs the averaging then produces false colour image maps of MRE across the sample. The data can then be saved both as a colour map and as a 240×360 matrix of MRE values as a .csv file. A schematic diagram of an emission geometry MRE measurement is given in figure 3.6.

3.3.2 Measuring the MRE through reflectivity

In the reflection geometry, the change in conductivity of a material in an externally applied magnetic field is measured as a change in the reflectivity of the material in the applied field. Reflection spectra are recorded at two different magnetic field strengths, $S_1(\mathbf{H}_1)$ and

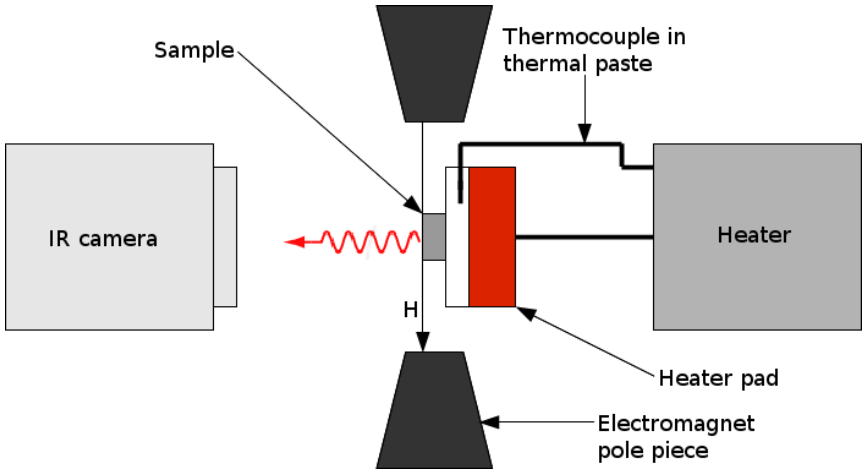

Figure 3.6: Schematic diagram of an emission MRE measurement as performed in York. A resistance heater pad is used to raise the temperature of the sample so that it thermally emits IR radiation which is detected by an IR camera. The temperature is kept stable using a negative feedback system which turns a heater on and off when the temperature of the thermocouple goes beyond set limits. A magnetic field can be applied in the direction indicated.

$S_2(\mathbf{H}_2)$. The MRE in this geometry is defined as the difference between these two spectra, expressed as a percentage (equation 3.3). Several repeat spectra are recorded at each field and averaged in order to improve the signal to noise ratio. This is critical as the percentage change in MRE is often very small, on the order of $\sim 0.1 - 1.0\%$.

$$\text{MRE}\% = \frac{S_1(\mathbf{H}_1) - S_2(\mathbf{H}_2)}{S_2(\mathbf{H}_2)} \times 100\% \tag{3.3}$$

In laboratories such as in York, which are not climate controlled, there can be drifts in reflectivity caused by variation in the ambient temperature. This could occur for many reasons but the most significant contribution would be from the gradual heating of the electromagnet during the experiment, The ohmic heating of the magnet can cause an increase in temperature at the sample location which in turn causes a change in the overall intensity of the reflected spectrum. The effect of this drift in intensity can be significantly reduced by collecting an extra spectrum, $S_3(\mathbf{H}_1)$, at one of the two fields to include in the averaging. If the drift, *x*, is linear between measurements, then the values of the three reflectivity spectra are given by S_1, $S_2 + x$ and $S_3 + 2x$. The expression for the MRE becomes:

$$\begin{aligned}
\text{MRE}\% &= \frac{\left[\frac{S_1(\mathbf{H}_1)+S_3(\mathbf{H}_1)}{2}\right] - S_2(\mathbf{H}_2)}{S_2(\mathbf{H}_2)} \times 100\% \\
&= \frac{\left[\frac{S_1(\mathbf{H}_1)+S_1(\mathbf{H}_1)+2x}{2}\right] - S_2(\mathbf{H}_2) - x}{S_2(\mathbf{H}_2) + x} \times 100\% \\
\text{MRE}\% &= \frac{S_1(\mathbf{H}_1) - S_2(\mathbf{H}_2)}{x + S_2(\mathbf{H}_2)} \times 100\% \qquad (3.4)
\end{aligned}$$

The term accounting for the drift is insignificant compared to the magnitude of the spectra so can safely be neglected. Without the additional spectrum the drift has a complicated second order presence in the equation for the MRE and becomes significant.

A schematic diagram of an MRE measurement in the reflection geometry is shown in figure 3.7. The sample to be measured is fixed substrate down, using vacuum grease, to a goniometer and placed within a 12 kOe electromagnet so that the field direction is parallel to the sample plane. The goniometer allows the sample position and orientation in 3D to be controlled, facilitating alignment of optical components. Polarisers can also be inserted during alignment if polarisation-dependent measurements are to be performed. The measurement is performed by reflecting IR radiation, sourced from a Fourier transform IR spectrometer (FTIR), off the surface of the sample at an angle of $\sim 65\,^\circ$ and collecting the radiation in a mercury cadmium telluride (MCT) detector. The source in the FTIR is an IR bulb that generates randomly polarised IR radiation in the range $2 - 25\,\mu$m, although in practice the measurable range is $\sim 4 - 20\,\mu$m as the photon count at the extremes of the range is too low to get the signal-to-noise ratio necessary to provide statistically meaningful data. The MCT detector requires a reservoir of liquid nitrogen to cool the detector to a temperature where there is minimal thermal noise, allowing a clean signal to be observed. Omnic software is used to collect and process data from the detector.

The entire experimental bench is housed within a perspex container which is purged with an N_2 atmosphere. Molecules such as CO_2 and H_2O have molecular bonding orbitals that absorb strongly in the near-IR. Displacing these molecules with N_2 stops the detected signal from being attenuated by the atmosphere and produces a signal which has far fewer contaminant spectral features. It is also possible to reduce the effect of absorption in the optics and detector by normalising the spectra against a featureless, highly reflecting reference spectrum from a material such as gold. Before a measurement is performed, the electromagnet is swept through a full hysteresis loop, to its maximum positive and negative field. This facilitates reproducibility of the measurement by minimising hysteretic

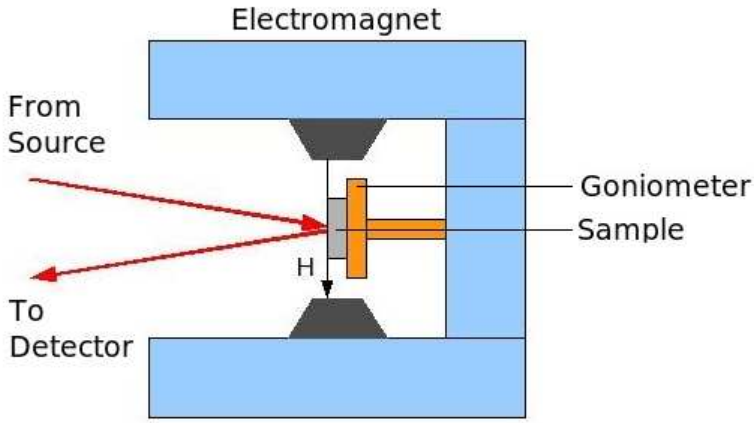

Figure 3.7: Schematic diagram of a reflection MRE measurement as performed in York. IR radiation from an FTIR is reflected from the surface of the sample and collected in an MCT detector in an N_2 atmosphere. An externally applied magnetic field (**H**) can be applied in the direction indicated using a 12 kOe electromagnet.

effects. The reproducibility is also aided by using a LabView program to control the electromagnet remotely, removing any human error in setting the correct field. Several repeat measurements are taken of each spectra in order to improve the accuracy of the measurement. The spectra are averaged before being input into equation 3.3 or 3.4. It is usually sufficient to perform 4-8 repeat measurements in high fields ($\sim$10 kOe) to obtain an error of $\pm 0.01\%$. However, in fields close to zero there can be a much greater uncertainty in the magnitude of the field. This occurs if the magnetisation of the sample varies sufficiently in zero field due to random thermal effects. It is often necessary to perform more than 8 repeat measurements in this low field regime in order to obtain sufficient precision. The data obtained from the Omnic software is exported as a .csv file and is analysed using a Python program written by the author. The program takes the raw .csv files and creates files containing averaged reflection spectra and MRE spectra which can be plotted against wavenumber in cm^{-1}, wavelength in μm and energy in eV.

3.3.3 Synchrotron based MRE experimental techniques

There are limits to the information that can be obtained from both the emission and reflection MRE measurements performed in York. In the emission geometry, the IR camera used has a very narrow spectral range $8-12$ μm. This narrow spectrum provides no spec-

tral resolution so can not be used to successfully model the MRE. It is not possible to discover anything about the underlying MR processes, only whether there is any variation in the magnitude of the MR spatially across the sample. For the reflection geometry the opposite is true. There is sufficient spectral resolution in the range $\sim 4 - 20\,\mu$m to successfully model the MRE but due to the diffuse beam spot it is impossible to spatially resolve variations in MRE across the sample. It is therefore impossible to measure spatial variations in GMR with such a reflection geometry measurement. Also, the correlation between the MRE and GMR is stronger in the far-IR, a region of the spectrum which is inaccessible with the FTIR bulb source and MCT detector in the laboratory at York.

To overcome these three limitations, a new experimental procedure was developed that offers both spectral and spatial resolution as well as sufficient IR radiation in the far-IR to perform measurements in the far-IR. These experiments took place on the SMIS beamline at SOLEIL, the French national synchrotron light source, in Saint-Aubin, Paris. Synchrotron radiation sources have high brightness, intensity and brilliance across the electromagnetic spectrum from microwaves to hard x-rays. The SMIS beamline offers sufficient radiation in the $\sim 1.5 - 50.0\,\mu$m range to obtain meaningful statistics in the far IR, overcoming the laboratory limitation of insufficient photon flux beyond $\sim 20\mu$m. The microscope is fitted with an MCT detector which is capable of detecting radiation in the range $\sim 1.5 - 20.0\,\mu$m. Far-IR radiation is detected using a liquid helium cooled bolometer which is sensitive to radiation in the range $\sim 14 - 50\,\mu$m. The second advantage of synchrotron radiation is that the beam of radiation produced is highly collimated. The electrons in the storage ring are highly relativistic, therefore the radiation emitted is strongly collimated in the direction of travel due to relativistic beaming. This produces a much less diffuse beam of radiation than the FTIR source in the laboratory at York. The problem of obtaining spatial resolution is ultimately resolved using an IR microscope. The radiation from the synchrotron is passed through a Schwarzschild objective before being focussed onto the sample and collected by an MCT detector in a similar reflection geometry that is used for the measurements in York. The combination of these advantages provides an MRE measurement which is spectrally resolved in the range $1.5-50.0\,\mu$m and the possibility of spatial resolution down to the diffraction limit ($\sim 1 \times 1\,\mu$m) in the IR). This measurement configuration provides both spectral and spatial resolution in a single measurement, which has previously been unattainable.

Design of a bespoke electromagnet

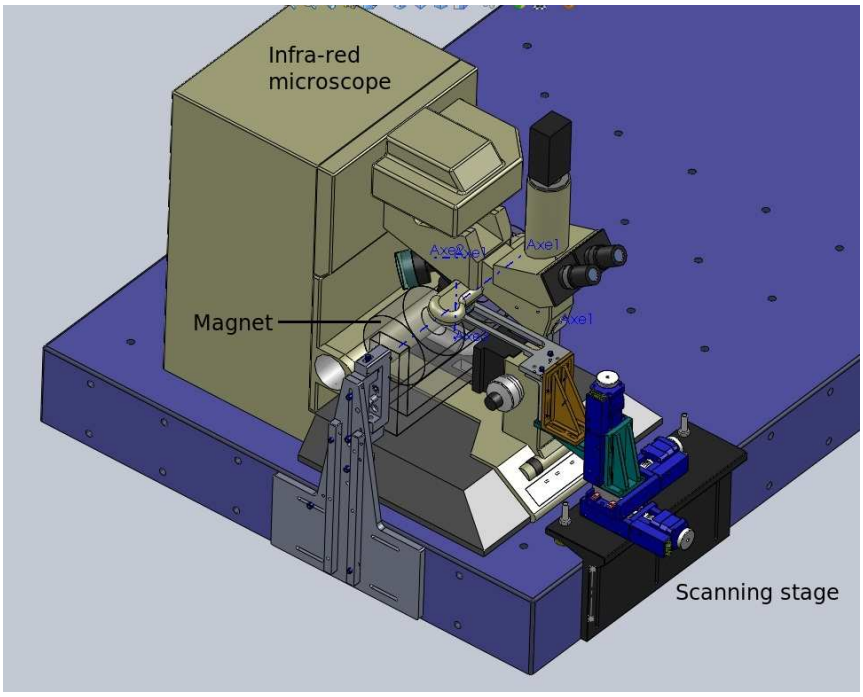

Figure 3.8: Scale diagram of the SMIS beamline IR microscope at SOLEIL, showing the bespoke electromagnet and 3D scanning stage. The detectors and beamline optics to the right of the microscope are not shown for clarity. Image courtesy of Stéphane LeFrançois.

The SMIS beamline is not designed to accommodate an electromagnet, so the microscope on the beamline had to be significantly modified in order to be able to perform spatially resolved field dependent measurements. The IR objective of the microscope has a diameter of 65 mm so a bespoke electromagnet needed to be constructed with pole pieces that fit around this objective, as well as being physically small enough to fit around the microscope and beamline optics in the vicinity of the microscope. The electromagnet was constructed with a 70 mm pole piece separation (l_g). The magnet was built to give a maximum theoretical magnetic field of 1000 Oe when operated with a 70 V/2 A power supply, a simple calculation using $B = \frac{\mu_0 NI}{l_g}$ [56] demonstrates that $N = 2785$ (turns per coil) are necessary to generate the desired field. The maximum magnetic field at the sample position was measured to be $\sim$900 Oe, slightly lower than the predicted maximum due to flux leakage in the yoke due to the sharp corners and other associated losses. A technical drawing of the electromagnet is given in figure 3.9.

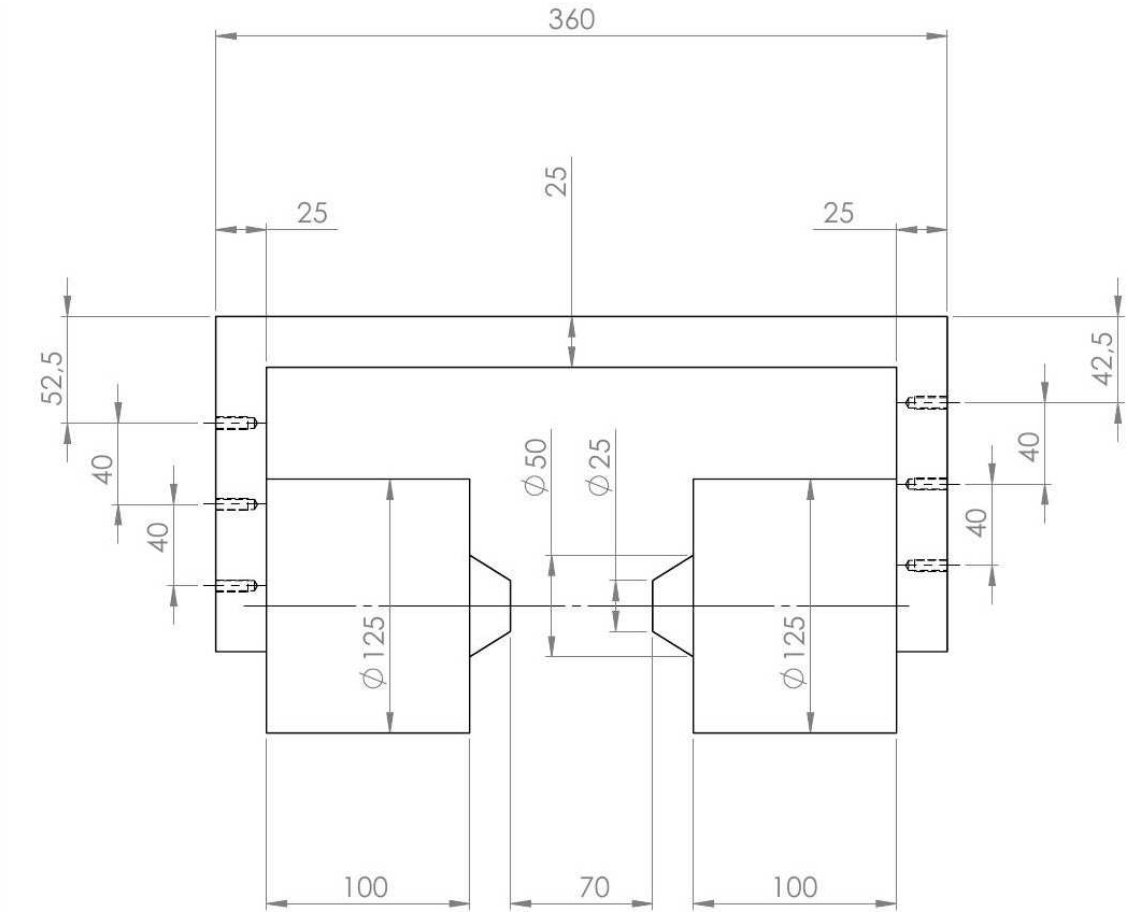

Figure 3.9: Technical drawing of the bespoke electromagnet with dimensions in millimetres. The electromagnet was built in the Department of Physics' mechanical workshop at the University of York. Image courtesy of Stéphane LeFrançois.

Writing a LabView control program to control the electromagnet

A LabView 2011 program was written in order to automate use of the electromagnet in the MRE experiments performed at SOLEIL. This allowed reproducibility when sweeping the electromagnet through hysteresis loops and in stopping at desired magnetic fields, minimising errors due to hysteresis and human error in setting the fields. The automation allows for a much quicker, simpler experiment than if the experiment was performed manually. The program sends control voltage signals to a National Instruments NI USB-6211 data acquisition (DAQ) box which controls a Kepco BOP 50-8ML 50 V power supply. The maximum control voltage sourced by the DAQ is ± 10 V, therefore the power supply scales the control voltage by a factor of 5. The program performs two main functions. Firstly, the program can sweep the magnet through an entire hysteresis loop, to a maximum field specified by the user. This is particularly useful at the beginning of an experiment to minimise errors arising due to hysteretic effects. Secondly, the program can sweep the electromagnet around a hysteresis loop in four stages, stopping at each stage in order to perform experiments at the required magnetic fields. The program goes from zero applied field to the maximum positive magnetic field, then from the maximum positive magnetic field to zero, then repeats for the negative maximum magnetic field before returning to zero field ready for the next experiment. The user decides when the electromagnet sweeps to the next field by pressing the appropriate button on the LabView front panel, shown in figure 3.10. The maximum positive and negative fields need not be the same, allowing full customisation of the hysteresis loop. The speed with which the magnet sweeps around the hysteresis loop can also be controlled, with indicators showing the time required to perform the sweep.

The modified SMIS beamline is shown in use in figure 3.11.

3.4 Other thin film characterisation techniques

3.4.1 Vibrating sample magnetometry (VSM)

Vibrating sample magnetometry (VSM) gives a direct measurement of a sample's magnetisation by tracing a hysteresis loop of magnetisation with applied field (an M/H loop). VSM is a very useful technique for characterising magnetic materials as M/H hysteresis

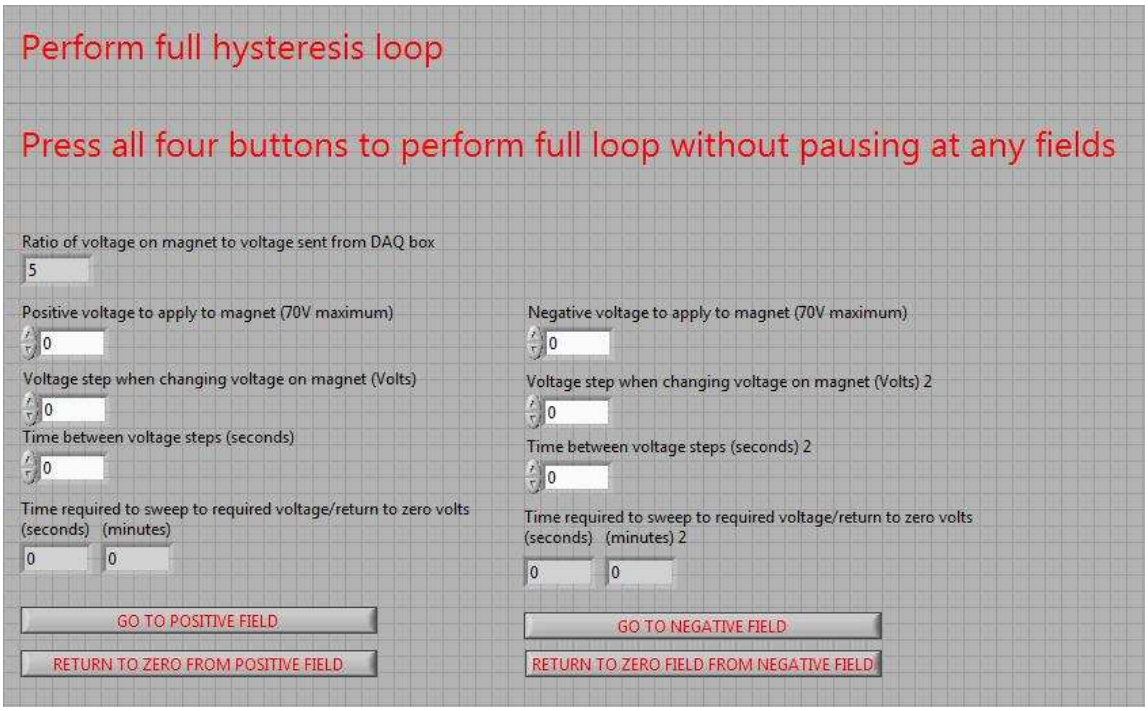

Figure 3.10: Screenshot of the LabView 2011 program that remotely controls the electromagnet for use in experiments at the SOLEIL synchrotron.

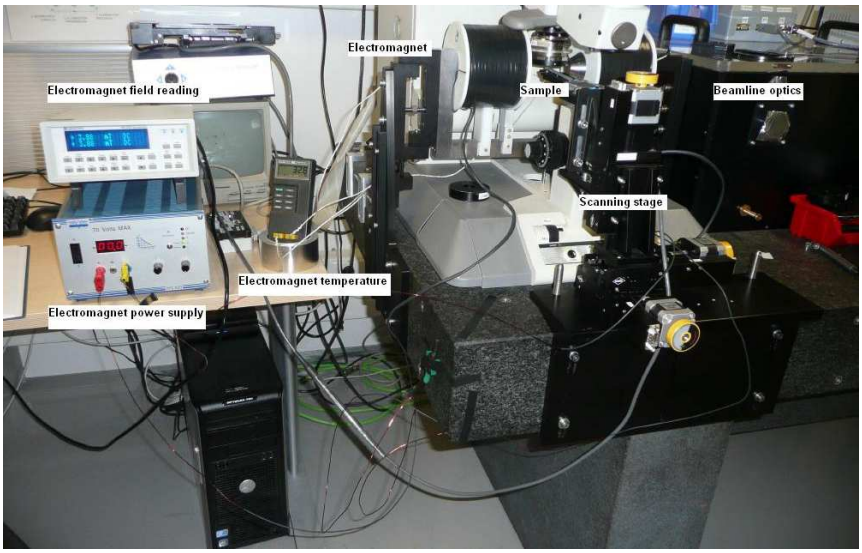

Figure 3.11: Modified SMIS beamline showing the operational electromagnet and 3D scanning stage.

loops provide several valuable pieces of information about the magnetic behaviour of the sample. It is possible to determine the magnetic field required to fully saturate the magnetisation of a sample in one direction. The saturation field, $\mathbf{H}_s$, is defined as the point where the magnetisation plateaus with applied field. The value of magnetisation at $\mathbf{H}_s$ is known as the saturation magnetisation, $\mathbf{M}_s$. Once a sample has been taken to $\mathbf{H}_s$, if the field is reduced to zero some of the magnetic moments in the sample will begin to reverse. The magnetisation that remains is known as the remanent magnetisation, $\mathbf{M}_r$. Finally if a magnetic field is applied in the reverse sense then the field required to reduce the magnetisation to zero, is known as the coercive field, $\mathbf{H}_c$. $\mathbf{M}_s$ depends entirely on the composition of the sample as it comprises the number as well as relative strength of the magnetic moments in the material. $\mathbf{H}_c$, $\mathbf{H}_s$ and $\mathbf{M}_r$, which are illustrated in figure 3.12, can all vary with material structure and temperature so care has to be taken when analysing these parameters.

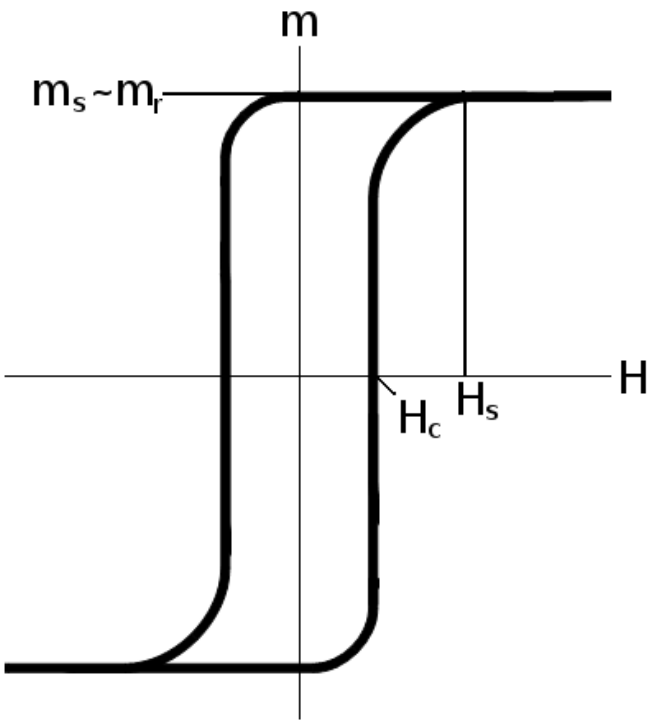

Figure 3.12: Example schematic hysteresis loop for a ferromagnetic material, showing the saturation field ($\mathbf{H}_s$), the coercive field ($\mathbf{H}_c$) and the remanent magnetisation ($\mathbf{M}_r$). For this loop $\frac{\mathbf{M}_r}{\mathbf{M}_s} \sim 1$ but $0 \leq \frac{\mathbf{M}_r}{\mathbf{M}_s} \leq 1$ in general.

The measurement is performed by placing the sample between the pole pieces of an electromagnet. The sample is then vibrated using a piezoelectric motor at a constant frequency, passing pickup coils which detect the variation in magnetic flux due to the pres-

ence of the sample. A current is induced in the pickup coils that is proportional to the magnetic moment of the sample but independent of the applied magnetic field. If the physical dimensions (or mass) of the sample are known accurately then the number of magnetic moments in the sample can be deduced allowing the magnetisation to be calculated. The voltage induced is very small so a lock-in amplifier must be used in order to lock onto the specific vibration frequency. With this it is possible to greatly reduce the noise in the measurements.

The VSM used to perform these measurements is a MicroSense Model 10 Mk II. This VSM allows vector magnetisation measurements at fields up to 22 kOe with noise of less than 0.5×10^{-9} Am^2. The field direction can be rotated through $\pm(540.0 \pm 0.2)^\circ$ and temperature dependent measurements can be performed between 77 K and 773 K with a resolution of 0.01 K. The VSM measurements presented in this thesis were made by the author and/or Mr James Sizeland unless otherwise stated. The author wishes to acknowledge Prof. Kevin O'Grady for allowing use of the VSM.

3.4.2 Transmission electron microscopy (TEM)

High resolution transmission electron microscopy (HR-TEM) is a powerful tool for the analysis of thin films as it allows the atomic scale structure of materials to be examined. A high voltage electron gun is used to generate a beam of electrons which is focussed onto the sample by a series of magnetic lenses. The electrons scatter through the material depending on the relative charge density in the region and are collected by a CCD detector. From this information it is possible to determine where the areas of significant charge density, such as atoms and some molecular bonds, are located. The sample must first be prepared by thinning it to electron transparency. This is done mechanically and then fine thinning is performed using an ion mill. In the York-JEOL Nanocentre this is done using a precision ion polishing system (PIPS) which uses Ar ions to chip away tiny fragments of material leaving the sample very flat and thin. Samples can be prepared to observe either the plan view of the structure or the cross section of the material. Cross sectional analysis is very important as it allows accurate determination of film thickness, as well as judging the uniformity of crystal structure and surface and interfacial roughness and cleanliness over several nanometres. HR-TEM also helps to spot defects in films such as dislocations, vacancies, stacking faults, interstitial atoms and anti-phase domain boundaries (APBs).

It is very important to prepare the sample along a plane of crystal symmetry, this way bright columns of atoms are formed in the resultant images without blurs from underlying layers. The TEM used to produce the micrographs in this image is a double aberration-corrected JEOL JEM-2200Fs TEM with a 200 kV electron gun, located in the York-JEOL Nanocentre. The TEM micrographs presented in this thesis were produced by Dr Vlado Lazarov, Mr James Sizeland and Mr Daniel Gilks.

Chapter 4

Modelling the Reflectivity and MRE of Iron Oxide Thin Films

A series of Fe_3O_4 films of 10, 18, 37, 64 and 110 nm thickness were grown by Dr. James Naughton in the MBE system in York. Dr. Naughton obtained the experimental reflection and MRE spectra presented in this section using the technique outlined in chapter 3 of this thesis for obtaining MRE spectra in York. In this section, the MRE model used to describe the films is compared to the experimental data. Systematic analysis of the simulated spectra in context of the experimental data allowed the model to be modified and improved, providing a closer reproduction of the experimental spectra as well as a deeper insight into the underlying physics.

4.1 Modelling of the reflectivity of Fe_3O_4 thin films as a function of thickness

The growth conditions used by Dr. Naughton in the preparation of the films considered were based on those used by Gao *et al*[37]. The MgO substrates were cleaned *ex-situ* by sonication in acetone and then isopropanol to remove contaminant organic molecules. The substrates were further cleaned *in-situ* by annealing in atomic oxygen at 973 K for two hours. The substrates were then cooled to 623 K in the oxygen to eliminate any oxygen vacancies introduced during annealing. The Fe_3O_4 films were then deposited on the substrates by simultaneous oxidation with an oxygen plasma source, as outlined in section 3.1.1. The iron deposition rate was 0.1 $Å s^{-1}$, with an RF plasma power of 200 W and oxygen partial pressure of 2×10^{-5} mbar. The film thicknesses and structure were determined

using cross sectional HR-TEM performed at the York-JEOL Nanocentre by Dr. Naughton.

Simulated reflection spectra were generated using a Python program written by the author. This program is a transcription and extension of a model written in MathCad provided by Dr. Naughton. The benefits of the Python program are an increase in computational efficiency as well as the ability to easily perform spectral analysis such as peak height and gradient calculations. The spectral analysis functionality is new to the Python version of the model and is the work of the author. The program uses the theory outlined in chapter 2, calculating the reflectivity from the Fresnel equations using the MgO and Fe_3O_4 complex dielectric functions given below:

$$\begin{aligned}
\epsilon_{\mathrm{MgO}} &= \epsilon_{\infty} + \epsilon_{\mathrm{phonon}} \\
&= \epsilon_{\infty_{\mathrm{MgO}}} + \sum_{j=1}^{n} \frac{S_{j_{\mathrm{MgO}}} \omega_{j_{\mathrm{MgO}}}^2}{\omega_{j_{\mathrm{MgO}}}^2 - \omega^2 - i\gamma_{j_{\mathrm{MgO}}}\omega_{j_{\mathrm{MgO}}}} \qquad (4.1) \\
\epsilon_{\mathrm{Fe_3O_4}} &= \epsilon_{\mathrm{phonon}} + \epsilon_{\mathrm{ds}} + \epsilon_{\infty} + \epsilon_{\mathrm{Drude}} + \epsilon_{\mathrm{hopping}} \\
&= \sum_{j=1}^{n} \frac{S_{j_{\mathrm{Fe_3O_4}}} \omega_{j_{\mathrm{Fe_3O_4}}}^2}{\omega_{j_{\mathrm{Fe_3O_4}}}^2 - \omega^2 - i\gamma_{j_{\mathrm{Fe_3O_4}}}\omega_{j_{\mathrm{Fe_3O_4}}}} \qquad (4.2) \\
&+ \sum_{j=1}^{n} \frac{S_{j-\mathrm{ds}_{\mathrm{Fe_3O_4}}} \omega_{j-\mathrm{ds}_{\mathrm{Fe_3O_4}}}^2}{\omega_{j-\mathrm{ds}_{\mathrm{Fe_3O_4}}}^2 - \omega^2 - i\gamma_{j-\mathrm{ds}_{\mathrm{Fe_3O_4}}}\omega_{j-\mathrm{ds}_{\mathrm{Fe_3O_4}}}} \\
&+ \epsilon_{\infty_{\mathrm{Fe_3O_4}}} - \frac{\omega_{\mathrm{p}}^2}{\omega^2 - i\gamma\omega} - \frac{7.1 \times 10^{14}}{i\omega}
\end{aligned}$$

The parameters in table 4.1 were taken from previous work by Ahn, Choi, Noh, Degiorgi, Wachter, Ihle and Šimša[62,69,61,70]. The simulated reflectivity spectra produced by these groups are in good agreement with previous experimental studies in the energy regime of interest, so they are used in this model with confidence. Using the parameters in table 4.1, a series of reflection spectra with different values of film thickness were produced. The simulated spectra are given in figure 4.1a and the corresponding experimental spectra are given in figure 4.1b, where both sets of spectra have been normalised against a gold reference spectrum.

The experimental and simulated spectra in figure 4.1 show the same general trends but there are a few discrepancies between theory and experiment. There is a significant underestimation of the reflectivity at short wavelengths. Also, the location of the Fe_3O_4 phonon absorption peak at 18.5 μm is shifting towards longer wavelengths in the experi-

MgO resonance parameters		
	***j* = 1**	***j* = 2**
$\omega_{j_{\mathrm{MgO}}}$	$25.25\,\mu\mathrm{m}$	$15.55\,\mu\mathrm{m}$
$\gamma_{j_{\mathrm{MgO}}}$	$1315.79\,\mu\mathrm{m}$	$111.11\,\mu\mathrm{m}$
$S_{j_{\mathrm{MgO}}}$	6.80	0.043
Fe_3O_4 resonance parameters		
	***j* = 1**	***j* = 2**
$\omega_{j_{\mathrm{Fe_3O_4}}}$	$30.30\,\mu\mathrm{m}$	$18.52\,\mu\mathrm{m}$
$\gamma_{j_{\mathrm{Fe_3O_4}}}$	$250.00\,\mu\mathrm{m}$	$227.27\,\mu\mathrm{m}$
$S_{j_{\mathrm{Fe_3O_4}}}$	996.00	821.00
d-s transition parameters		
$\omega_{j-\mathrm{ds}_{\mathrm{Fe_3O_4}}}$		$2.02\,\mu\mathrm{m}$
$\gamma_{j-\mathrm{ds}_{\mathrm{Fe_3O_4}}}$		$2.31\,\mu\mathrm{m}$
$S_{j-\mathrm{ds}_{\mathrm{Fe_3O_4}}}$		11920
Other parameters		
$\epsilon_{\infty_{\mathrm{MgO}}}$		3.01
$\epsilon_{\infty_{\mathrm{Fe_3O_4}}}$		4.6
γ		$1.01 \times 10^{15}\,\mathrm{Hz}$
N		$1.86 \times 10^{26}\,\mathrm{m}^{-3}$

Table 4.1: The various modelling parameters necessary in order to calculate the reflectivity and MRE spectra for the Fe_3O_4/MgO system. The MgO parameters were obtained from Ahn, Choi and Noh[62,69]. The Fe_3O_4 modelling parameters were derived from Degiorgi, Wachter and Ihle[61]. The damping term (γ) and number of free carriers (N) were taken from Šimša[70].

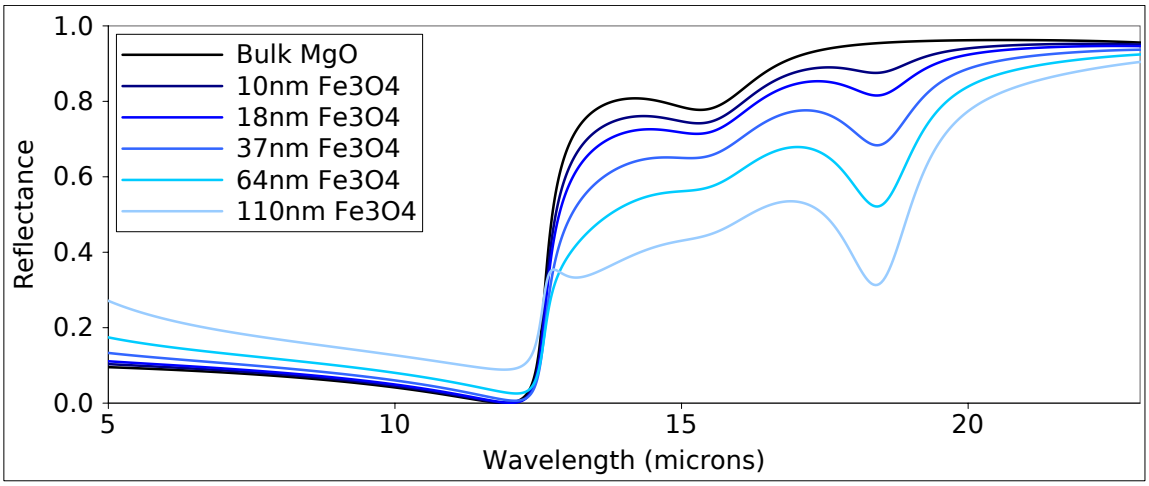

(a) Modelled infrared reflectivity spectra for MgO(111), and various thicknesses (10, 18, 37, 64 and 110 nm) of Fe_3O_4 on MgO(111).

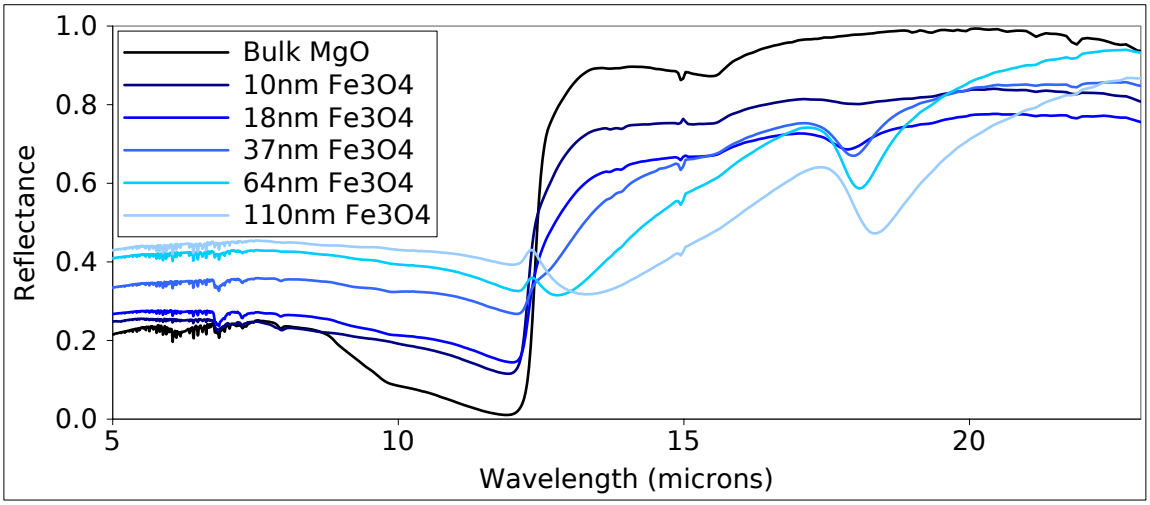

(b) Experimental infrared reflectivity spectra for MgO(111), and various thicknesses (10, 18, 37, 64 and 110 nm) of Fe_3O_4 on MgO(111).

Figure 4.1: Plots comparing the experimental and simulated reflection spectra. The overall trend of the experimental spectra is followed by the simulated spectra. However, the simulations underestimate the reflectivity at short wavelengths and the spectral feature at $\sim$18.5µm shifts in the experimental spectra but does not in the simulated spectra.

ment but not the simulation. The reflectivity is ultimately dependent on the conductivity of the film. The simulations suggest that the conductivities used to build the dielectric function may have been underestimated. One possible explanation for the low conductivity is that the model underestimates the metallic nature of the film. For this to be true, either the assumption that the Drude contribution to the conductivity is negligible is false, or the film contains a significant fraction of unoxidised iron, introducing an extra Drude term and increasing the conductivity. It is also possible that the hopping conductivity is underestimated. Calculating the hopping conductivity is an extremely difficult quantum mechanical problem to solve as it is a 3-body (at least) interaction and is very sensitive to the relative positions and separations of atoms in the lattice. It is possible that the fitting parameters as stated may be unique to their films and are underestimating the conductivity of the films grown in York. In the following section, the hopping and Drude conductivity contributions to the reflectivity are investigated by varying them to try and obtain spectra that are the same shape as the experimental spectra.

4.2 Modelling the reflectivity of Fe_3O_4 thin films

4.2.1 Modelling the conductivity contribution to the reflectivity

Figure 4.2 shows the experimental reflection spectrum for the 110 nm thick sample. Three simulated spectra are also shown; one where there is a Drude term and no hopping term (Drude only, $R \propto \omega^{-2}$), one where there is a hopping term and no Drude term (Hopping only, $R \propto \omega^{-1}$) and one with both terms (Both). The spectrum where the contribution is solely Drude is a different shape to the experimental spectrum, there is a step at ~ 12.5 μm whereas in the experimental spectrum there is a small peak at this location. The spectrum where the two terms are of equal order appears similar to the experimental spectrum, with a peak at ~ 12.5 μm, but the magnitude of the peak is overestimated. Finally, the spectrum where the hopping term is dominant is most like the experimental spectrum, with a peak at ~ 12.5 μm that is closer to the size of the experimental peak. These spectra suggest that the dominant dependence of R on frequency is $R \propto \omega^{-1}$ from the hopping term. This gives credence to the assumption that the Drude contribution was insignificant[71].

A set of simulated spectra were plotted for increased values of hopping conductivity, shown in figure 4.3, to attempt to verify whether the hopping conductivity may have been

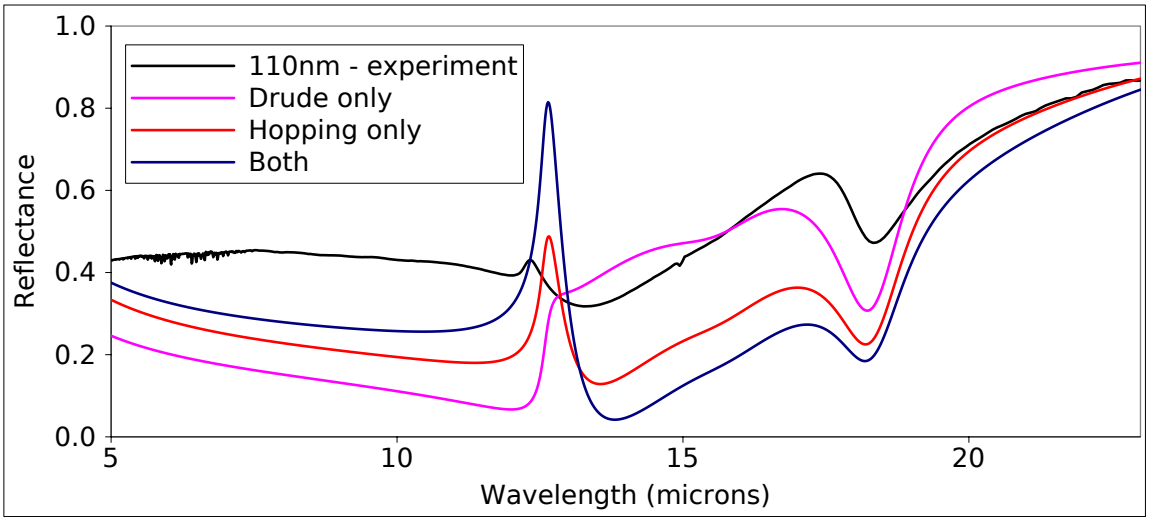

Figure 4.2: Plot of the experimental reflection spectrum of the 110 nm Fe_3O_4 film with a set of simulated reflection spectra with different conductivity profiles. The simulated spectrum where the conductivity is dominated by polaron hopping gives a reasonable approximation to the shape of the experimental spectrum. The simulated spectrum where the Drude term is of the same order as the hopping is less of a good fit, the simulated spectrum where the Drude term is dominant does not reflect the experimental spectrum at all. This is consistent with the prediction that the hopping term is dominant in the wavelength regime of interest.

underestimated.

It can be seen that increasing the hopping conductivity to around $\sigma_{\text{hopping}} = 1000\,\Omega^{-1}\text{cm}^{-1}$ fits the general shape of the spectra much better than $500\,\Omega^{-1}\text{cm}^{-1}$. The reflectivity is higher to the left of the peak than on the right for $1000\,\Omega^{-1}\text{cm}^{-1}$, the lowest value for which this is true. Higher values increasingly exaggerate the magnitude of the peak. The overall magnitude of the reflectivity is still much lower than in the experiment. Figure 4.4 compares the experimental reflection spectrum of the 64 nm thick film with simulated spectra with the original hopping conductivity of $500\,\Omega^{-1}\text{cm}^{-1}$and the increased value of $1000\,\Omega^{-1}\text{cm}^{-1}$. It is again clear that the increased hopping conductivity gives the simulated spectrum the correct shape, with a peak rather than a step as the spectral feature.

Figures 4.5-4.9 compare the experimental spectra with the simulated spectra with a hopping conductivity of $1000\,\Omega^{-1}\text{cm}^{-1}$ for each sample, assuming that the conductivity of all the films is the same. This conductivity value is double that reported by Ahn[62].

It can be see from figure 4.10 that the shapes of the simulated spectra are now significantly closer to the shapes of their experimental counterparts. The overall reflectivity of the simulated spectra are much closer to those of the experimental spectra but are still un-

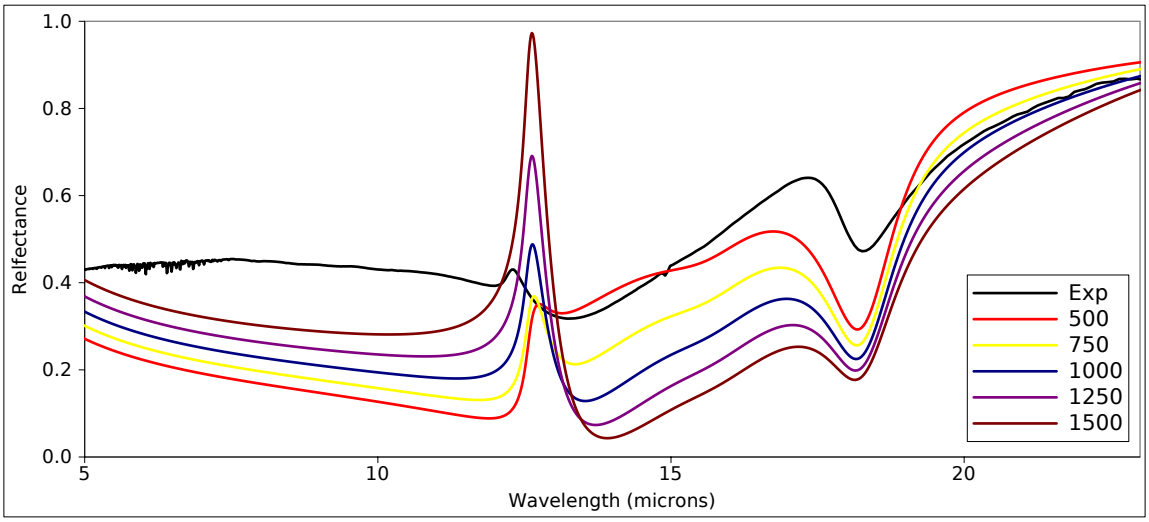

Figure 4.3: Plot showing a series of simulated reflection spectra with increasing hopping conductivities. The best fit to the overall shape of the experimental spectra comes when the value of the hopping conductivity is $1000\,\Omega^{-1}\,\mathrm{cm}^{-1}$.

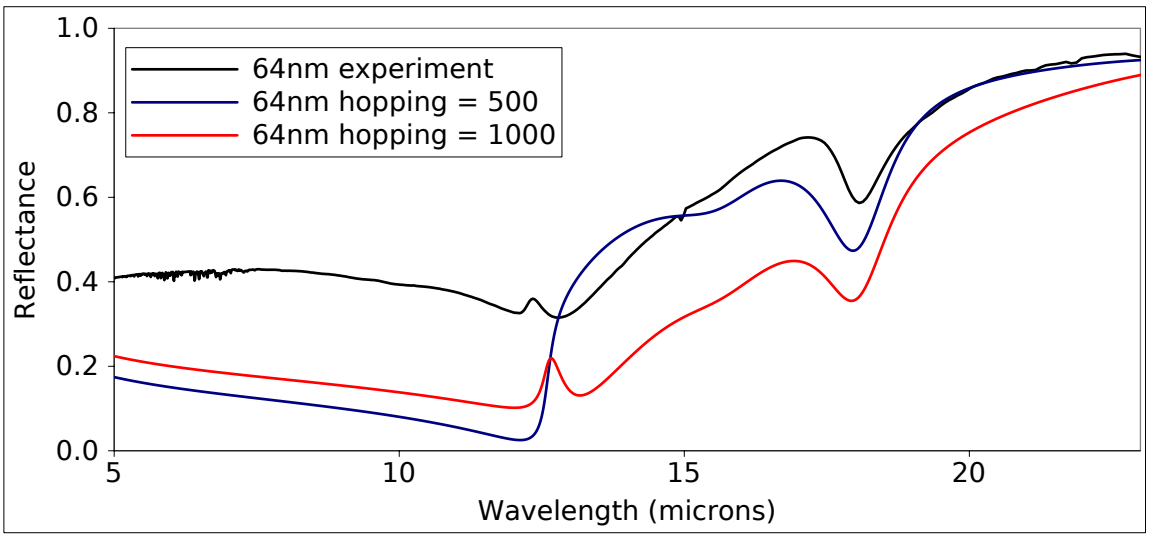

Figure 4.4: When compared to the experimental reflection spectra for the 64 nm sample, a much better fit to the general shape is obtained with a hopping conductivity double the size of the previous estimate.

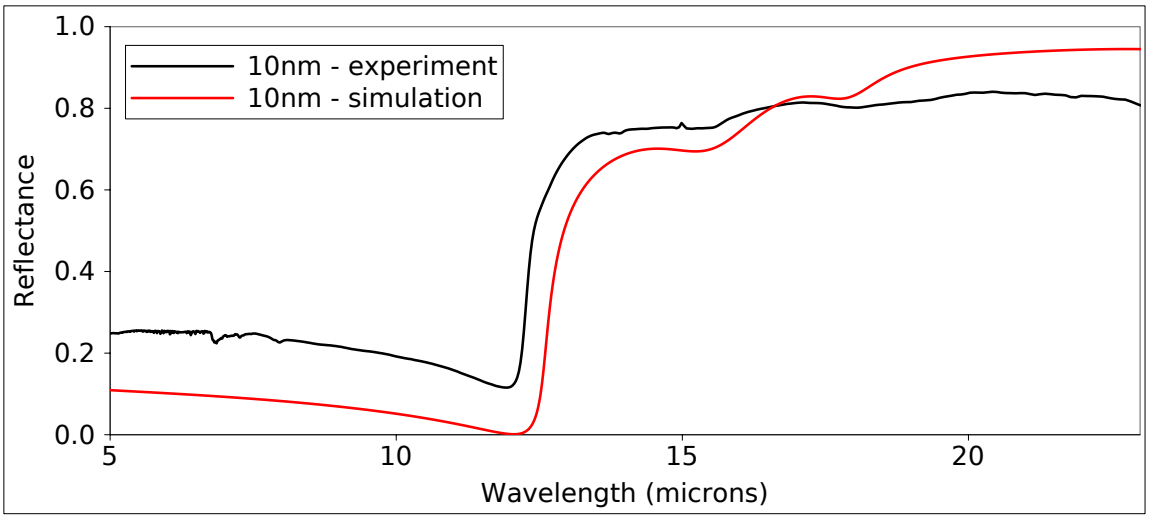

Figure 4.5: Experimental and simulated reflection spectra of a 10 nm Fe_3O_4 thin film.

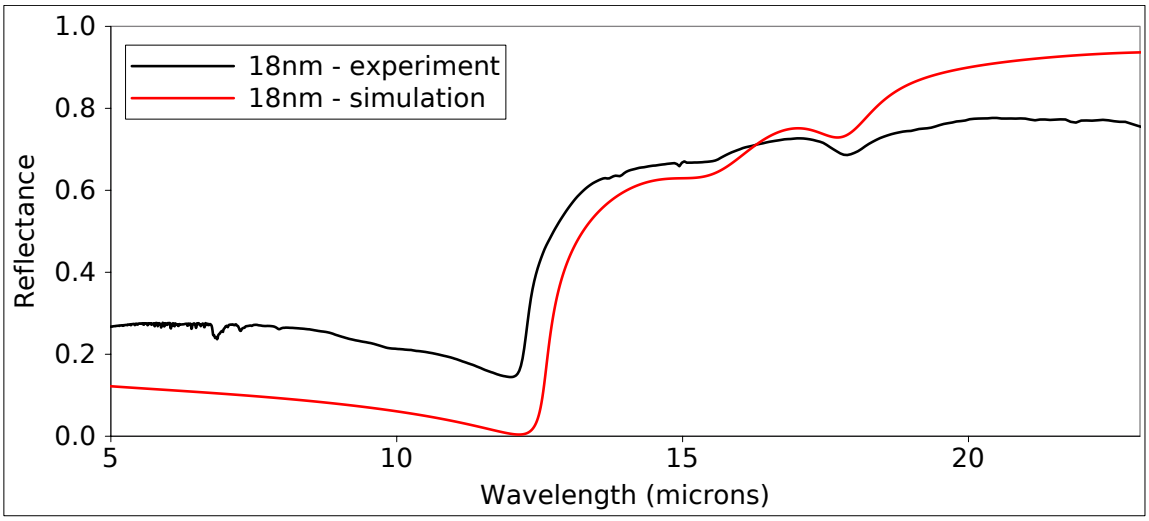

Figure 4.6: Experimental and simulated reflection spectra of a 18 nm Fe_3O_4 thin film.

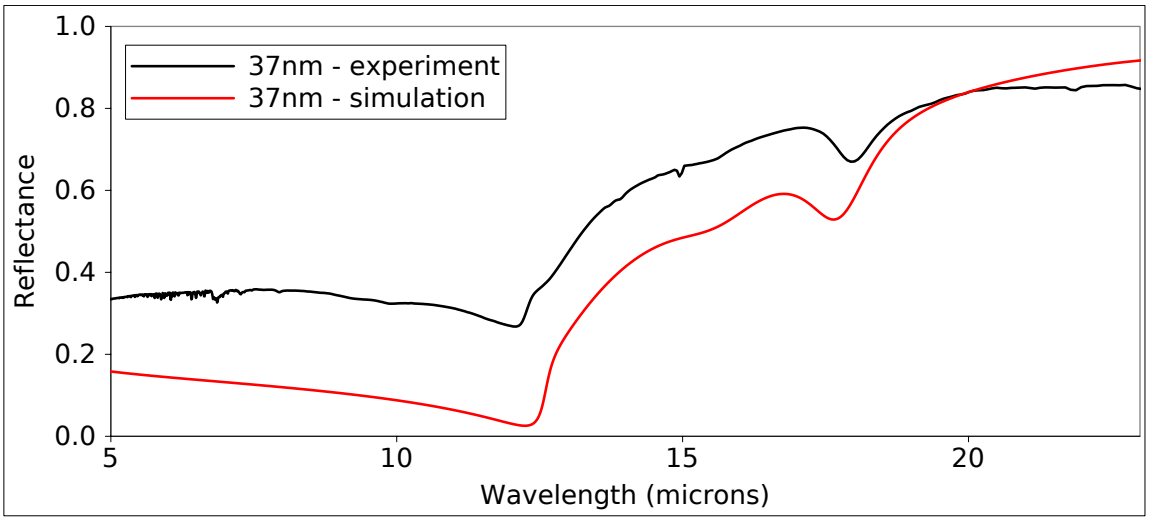

Figure 4.7: Experimental and simulated reflection spectra of a 37 nm Fe_3O_4 thin film.

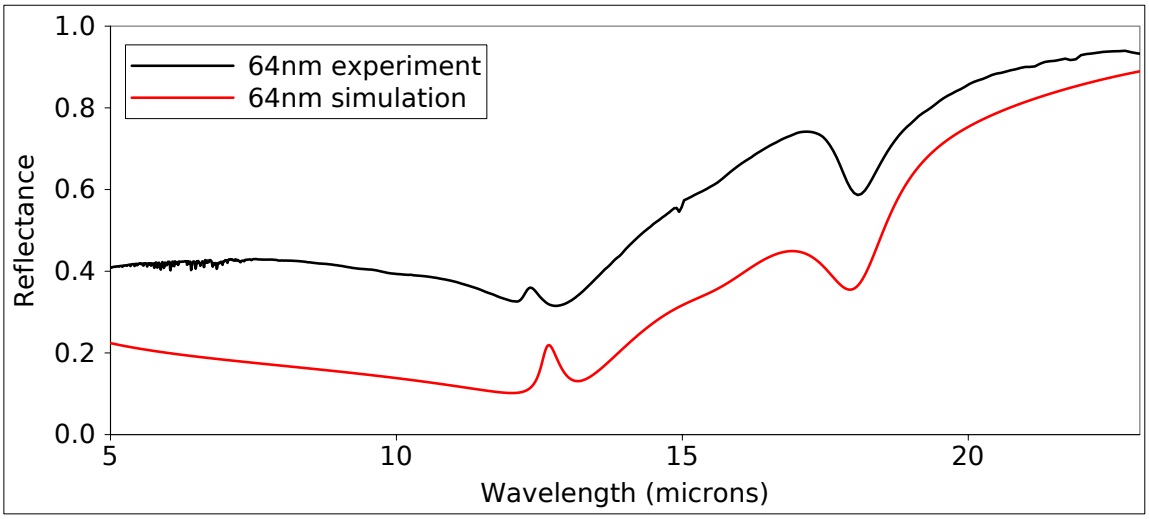

Figure 4.8: Experimental and simulated reflection spectra of a 64 nm Fe_3O_4 thin film.

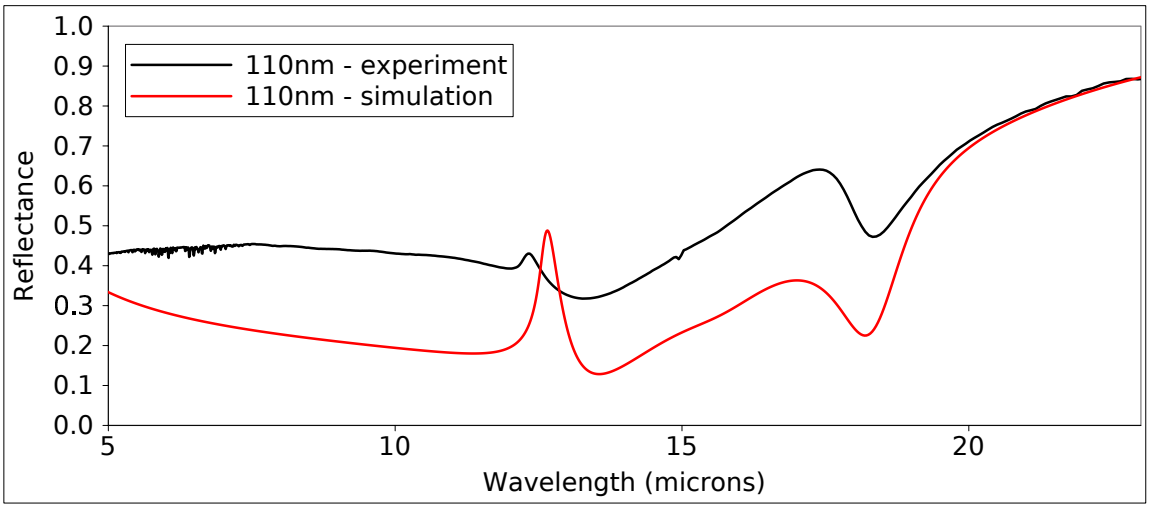

Figure 4.9: Experimental and simulated reflection spectra of a 110 nm Fe_3O_4 thin film.

derestimates. The changing experimental position of the Fe_3O_4 phonon absorption is not reproduced by the simulation, so must be the result of a phenomenon not yet incorporated into the model.

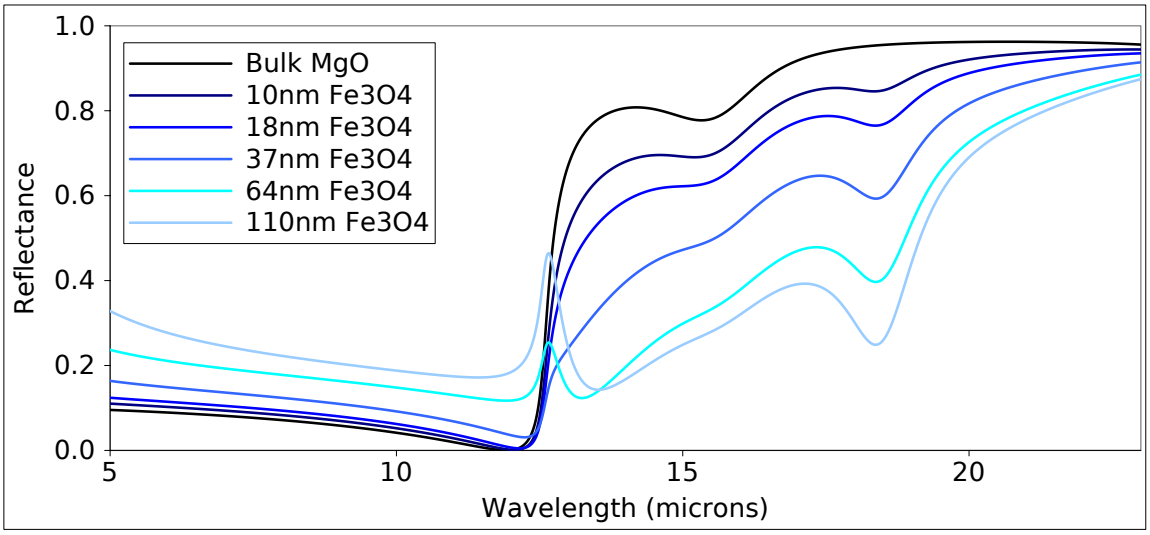

(a) Modelled infrared reflectivity spectra for MgO(111), and various thicknesses (10, 18, 37, 64 and 110 nm) of Fe_3O_4 on MgO(111) with $\sigma_{\text{hopping}} = 1000\,\Omega^{-1}\text{cm}^{-1}$.

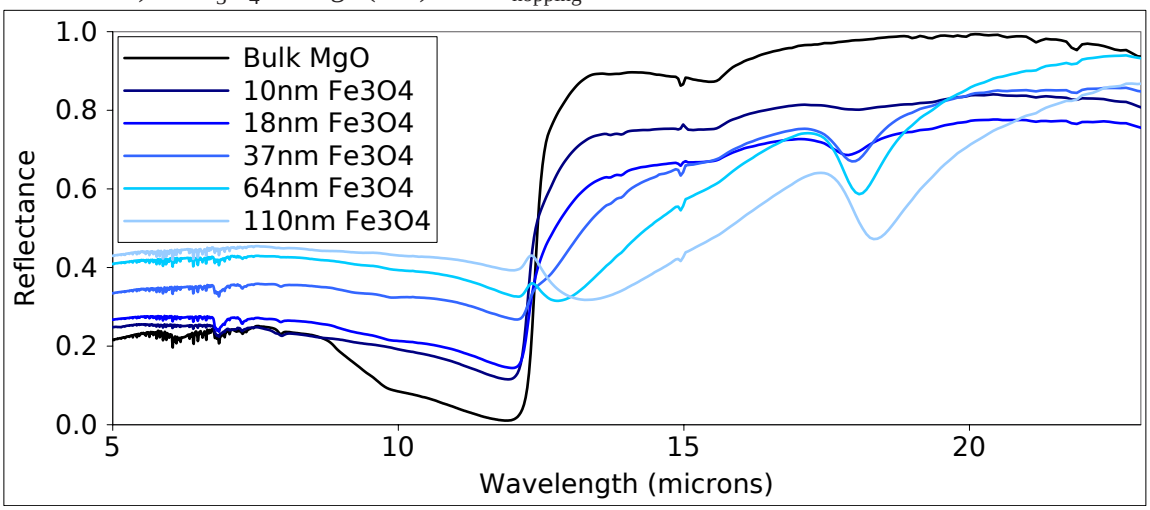

(b) Experimental infrared reflectivity spectra for MgO(111), and various thicknesses (10, 18, 37, 64 and 110 nm) of Fe_3O_4 on MgO(111).

Figure 4.10: Plots comparing the experimental and simulated reflection spectra. The overall trend of the experimental spectra is followed by the simulated spectra. However, the simulations underestimate the reflectivity at short wavelengths and the spectral feature at $\sim$18.5µm shifts in the experimental spectra but does not in the simulated spectra.

4.2.2 Modifying the simulated spectra to account for the shifting phonon resonance.

The experimental reflection spectra show a shift in the location of the absorption peak predicted to be at $18.5\,\mu$m; the peak shifts towards this bulk value with increasing film thickness. This shift is not reproduced in the simulated spectra. This shift is possibly due to strain in the lattice shifting the bond energy associated with the phonon. The $18.5\,\mu$m absorption is Raman active and such shifts in phonon energy due to strain have been observed in Raman spectra of Fe_3O_4 [72]. It is therefore reasonable to assume the same would be true in reflection spectra. Figure 4.11 shows a plot of the shift from the bulk location of the phonon peak with film thickness. It can be clearly seen, with the exception of the 10 nm sample, that the phonon peak position shifts linearly towards the bulk value of 18.5 μm. Extrapolating down to zero shift, a prediction can be made that the bulk value is recovered for a $\sim$145 nm thick film. It is possible that for the 10 nm sample the film is still in an island growth phase. This would lead to the film being discontinuous across the surface of the substrate leading to very different material properties. It appears that above 18 nm the film is continuous. Thus, as more material is added, the contribution from the ordered film becomes more important resulting in the shift in energy towards the bulk value.

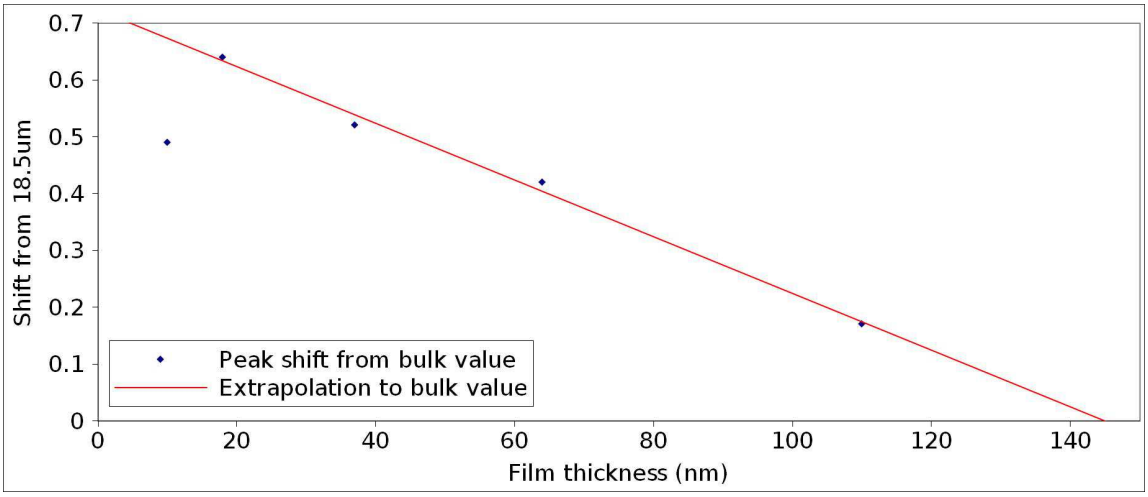

Figure 4.11: The position of the spectral feature due to the Fe_3O_4 shifts linearly towards the bulk value, reaching it a thickness of $\sim$145 nm. The 10 nm thick sample does not follow the trend of the other films.

In order to produce more accurate MRE spectra, this phonon shift needs to be incorporated into the model. This was done by taking the peak position from the experimental spectra and putting those values into the model instead of the bulk value. The result of this produces the more accurate simulated reflection spectra in figure 4.12a.

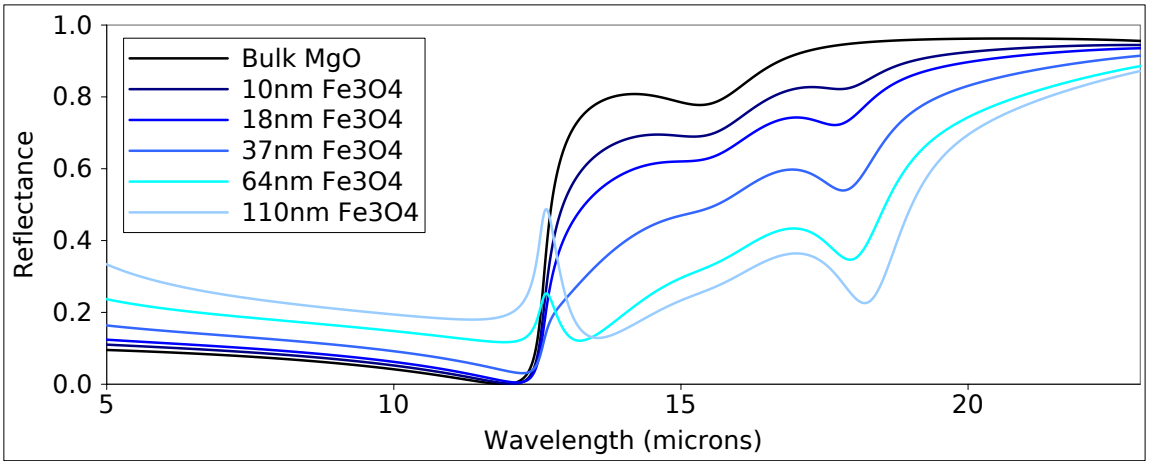

(a) Simulated reflectivity spectra using the experimentally determined location of the Fe_3O_4 resonance peak.

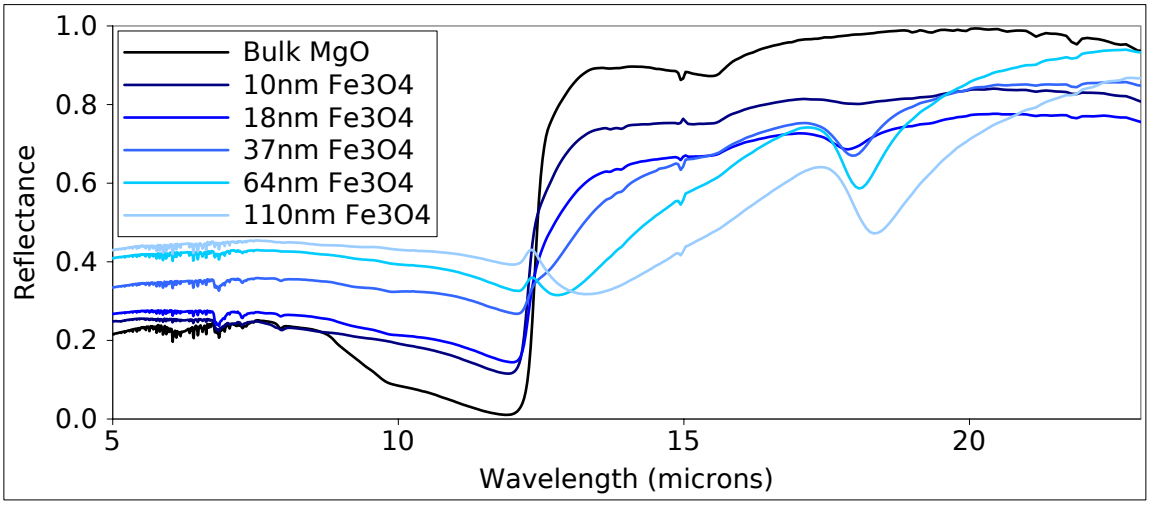

(b) Experimental infrared reflectivity spectra for MgO(111), and various thicknesses (10, 18, 37, 64 and 110 nm) of Fe_3O_4 on MgO(111).

Figure 4.12: Plots comparing the experimental and simulated reflection spectra, where the experimental position of the Fe_3O_4 resonance has been incorporated into the model. The overall trend of the experimental spectra is followed by the simulated spectra, although the simulations underestimate the reflectivity at short wavelengths.

4.3 Modelling the MRE of Fe_3O_4 thin films

4.3.1 Assigning the magnetic field dependence of the Fe_3O_4 dielectric function

The magnetic field dependence is introduced into the model by multiplying the appropriate conductivity components of the Fe_3O_4 dielectric function by $(1 + \eta h^2)$, where h is the fractional change in conductivity in the applied magnetic field and η is a fitting parameter to test the proportionality of the optical and d.c. electrical response. Electrical four-point probe measurements of the MR of the films show that each film has an MR of approximately 1% at 10 kOe, typical of Fe_3O_4 thin films[73], giving $h^2 = 1 \times 10^{-4}$ for each sample. The ηh^2 term represents the small conductivity change within the dielectric function caused by the magnetoresistance, hence we use this term to fit the magnitude of the MRE. As the value of h is very small, it will be difficult to say with certainty whether the difference in ηh^2 is due to a real change in magnetoresistance, h, or in the fitting parameter, η.

The spin-dependent conductivity of the Fe_3O_4 ultimately gives rise to the MR, so it is necessary to know which terms in the Fe_3O_4 dielectric function are spin-dependent and of significant magnitude in the spectral range under consideration. ϵ_∞ is a material constant and is independent of the magnetic field so the field dependence must be distributed amongst $\epsilon_{\text{phonon}}, \epsilon_{\text{ds}}, \epsilon_{\text{hopping}}$ and ϵ_{Drude}. ϵ_{phonon} is treated as independent of the external magnetic field. If it was field-dependent then there would be uncharacteristically large increases in the MRE signal at every Fe_3O_4 phonon resonance, which is not seen in the experimental MRE spectra. ϵ_{ds} represents a relatively high energy phenomena, outside the wavelength range of interest, so is discounted for this reason. The hopping term is potentially spin-dependent as the polaron hopping occurs between the 3d electrons that are responsible for the ferrimagnetism in Fe_3O_4. Although the Drude term must be spin-dependent (as the band structure is necessarily spin-split[74]), it has been previously noted that the contribution of $\epsilon_{\text{hopping}}$ is dominant over ϵ_{Drude}. We can therefore, to a first approximation, assign the magnetic field dependence to the hopping term with confidence:

$$\epsilon_{Fe_3O_4} = \sum_{j=1}^{n} \frac{S_{j_{Fe_3O_4}} \omega^2_{j_{Fe_3O_4}}}{\omega^2_{j_{Fe_3O_4}} - \omega^2 - i\gamma_{j_{Fe_3O_4}} \omega_{j_{Fe_3O_4}}} \tag{4.3}$$

$$+ \sum_{j=1}^{n} \frac{S_{j-ds_{Fe_3O_4}} \omega^2_{j-ds_{Fe_3O_4}}}{\omega^2_{j-ds_{Fe_3O_4}} - \omega^2 - i\gamma_{j-ds_{Fe_3O_4}} \omega_{j-ds_{Fe_3O_4}}} \tag{4.4}$$

$$+ \epsilon_{\infty_{Fe_3O_4}} - \frac{\omega_p^2}{\omega^2 - i\gamma\omega} - \left[\frac{1.4 \times 10^{15}}{i\omega}\left(1 + \eta h^2\right)\right]$$

This approach is different to that taken in previous MRE models where the magnetic field dependence was assumed to be due only to the spin-dependence of the Drude conductivity, as in a pure metallic system.

4.3.2 Fitting the simulated MRE to the experimental spectra

The ηh^2 term was used to fit the magnitude of the main feature in the MRE spectrum of each film. These MRE spectra are shown with their experimental analogues in figure 4.13.

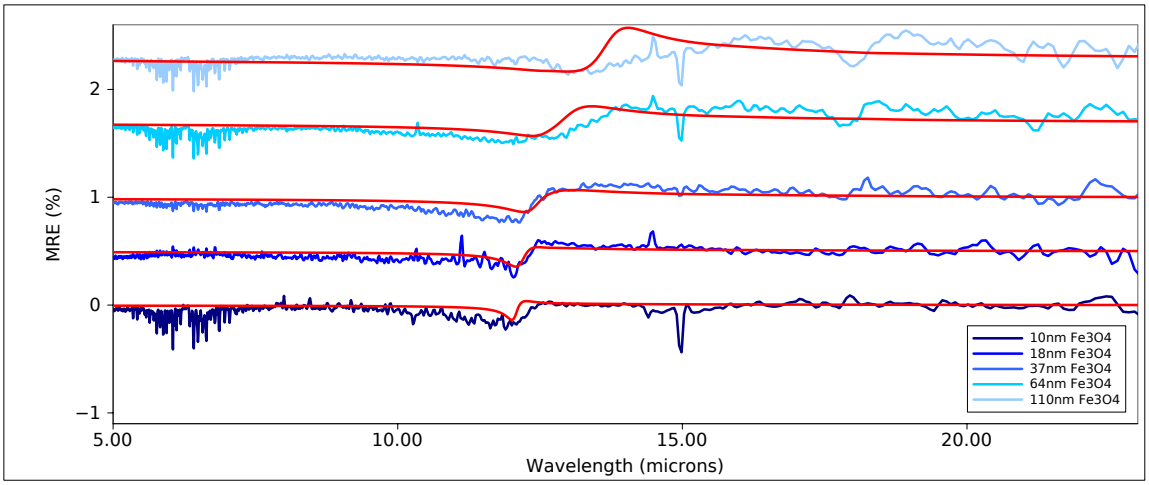

Figure 4.13: Stacked experimental and simulated MRE spectra for Fe_3O_4 films of increasing thickness. The height of the main spectral feature was used to gauge the value of ηh^2, the gradient (as measured from the maximum and minimum) of the feature however is not accurately reproduced for very low/high thickness. There is also an additional feature in the experimental spectra around 18.5 μm that is not present in the simulated spectra.

The magnitude of the main spectral feature of each film was measured for $h^2 = 1 \times 10^{-4}$, with no fitting parameter ($\eta = 1$), shown in figure 4.14. The simulation agrees within error ($\pm 0.05\%$) suggesting that the value of the η is approximately unity and there is a one-to-one correlation between the optical and electrical responses. The experimental

feature magnitudes are reproduced with only a slight change in the value of ηh^2 between samples of $(0.9 \leq \eta h^2 \leq 1.3) \times 10^{-4}$, as shown in figure 4.15. The narrow range in values of ηh^2 is consistent with there being little variation in the MR between the samples. Our approximation for h ($h \approx 1 \times 10^{-4}$) gives the range of the scaling parameter η as $0.9 \leq \eta \leq 1.3$, which is very close to 1.

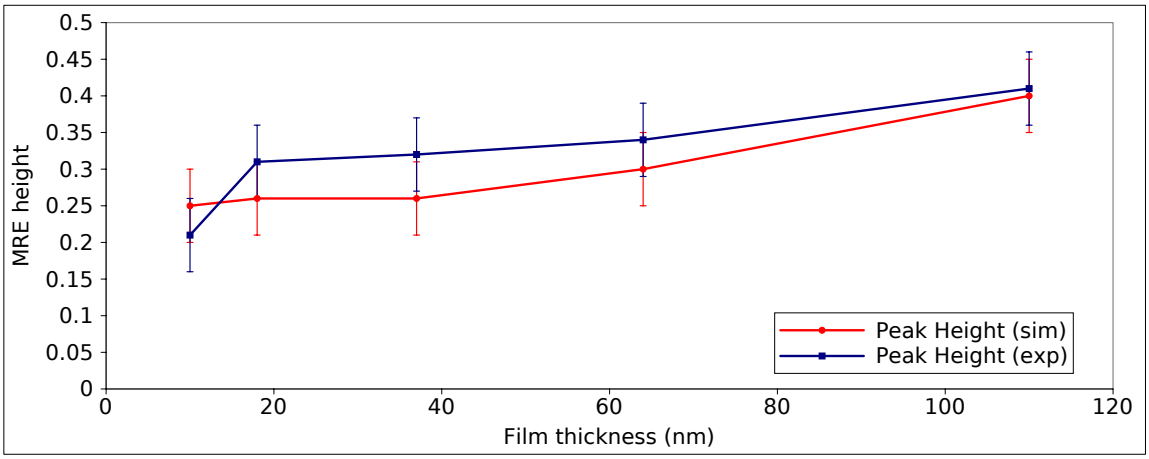

Figure 4.14: Comparison between the experimental and simulated peak heights for the 12.5 μm MRE spectral feature as a function of film thickness. The value of h used gives $h^2 = 1 \times 10^{-4}$ and the fitting parameter $\eta = 1$. The simulated peak heights agree within error with the experimental peak heights for all samples except the 18 nm sample.

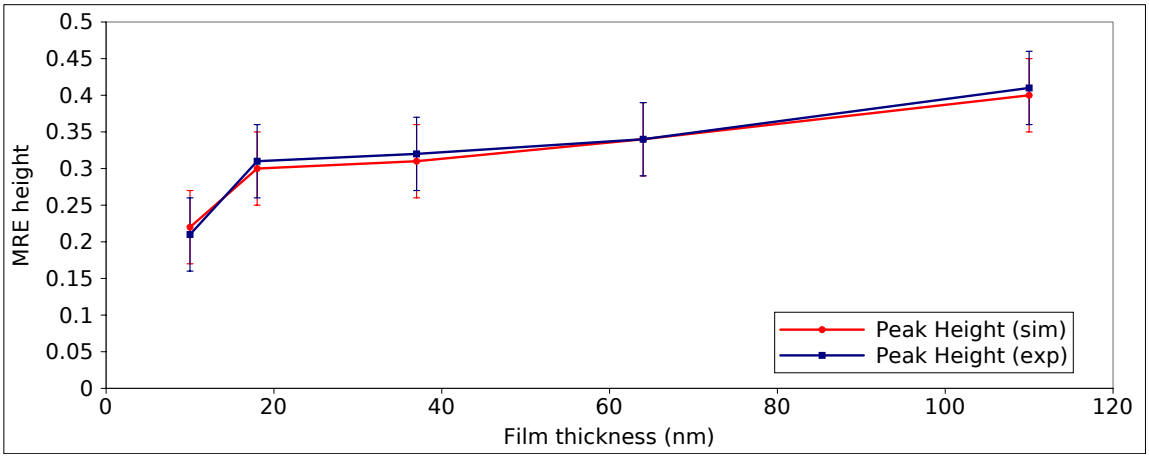

Figure 4.15: Comparison between the experimental and simulated peak heights for the 12.5 μm MRE spectral feature as a function of film thickness. The peak heights are fitted with ηh^2 values in the range $\eta h^2 = 0.9 \times 10^{-4} - 1.3 \times 10^{-4}$. The simulation can be made to follow the experimental trend with only a modest change in the value of ηh^2.

The gradient (as measured between the lowest and highest points of the main spectral feature) is well reproduced for the intermediate thickness samples, but not for the 10 nm and 110 nm samples, a shown in figure 4.16. There is also an unexpected additional spectral feature at ∼18.5 μm in the experimental spectra of the thicker samples that is not

reproduced in the simulations.

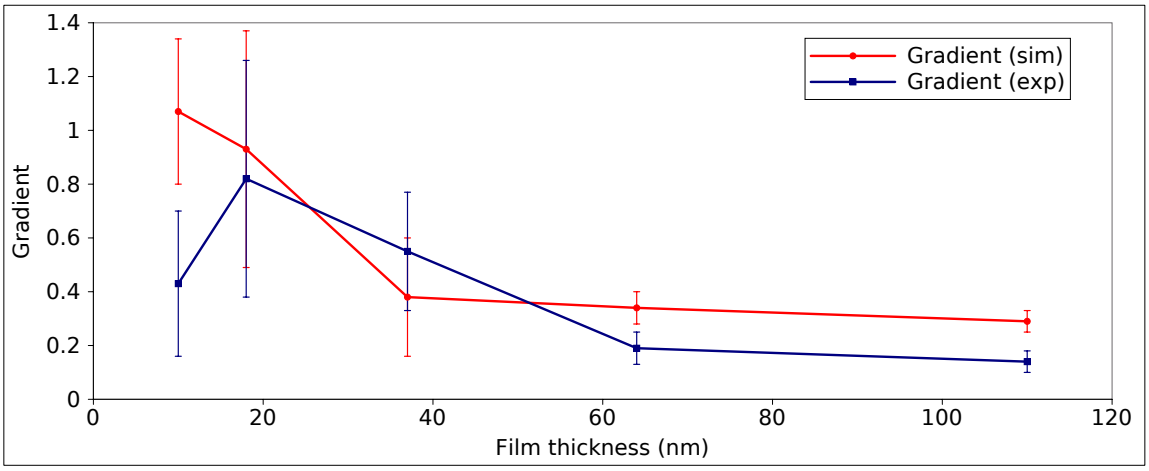

Figure 4.16: Comparison between the experimental and simulated gradients of the 12.5 μm MRE spectral feature as a function of film thickness. The simulation closely matches the experiment at intermediate thicknesses, is weaker at 110 nm and is not a good fit at 10 nm.

The feature in the MRE spectrum at 18.5 μm in the thicker films must be due to the Fe_3O_4 phonon resonance in that region as the feature becomes more prominent with increased film thickness. This feature also seems to shift towards the bulk location for this Fe_3O_4 phonon. The experimental evidence strongly suggests that there is an additional shift in the location of this phonon with magnetic field which has not been accounted for in the simulation. In a bid to reproduce the feature, a small change in the position of the phonon of 0.05 μm was introduced into the applied field dielectric function. The results of this modification are given in figure 4.17.

The small shift introduced into the simulation accounts for the feature seen in the experimental spectra. The physical origin of this shift could be the magnetic field modifying the bond lengths in the material, causing a change in the bonding energy resulting in a different phonon wavevector. A magnetic field has been shown to be capable of shifting the position of a phonon resonance in GaAs by Cheng *et al*[75]. Overall, the simulated spectra now fit the experimental spectra far more closely than in previous simulations, where the magnetic field dependence was assumed to be entirely due to the Drude conductivity. Although the model is very good at intermediate thickness, there is still significant differences between the experimental and simulated spectra at low/high thicknesses. Allowing the Fe_3O_4 phonon location to shift both with thickness and with the applied magnetic field also greatly increases the accuracy of the model, as well as better representing the underlying physics of the system.

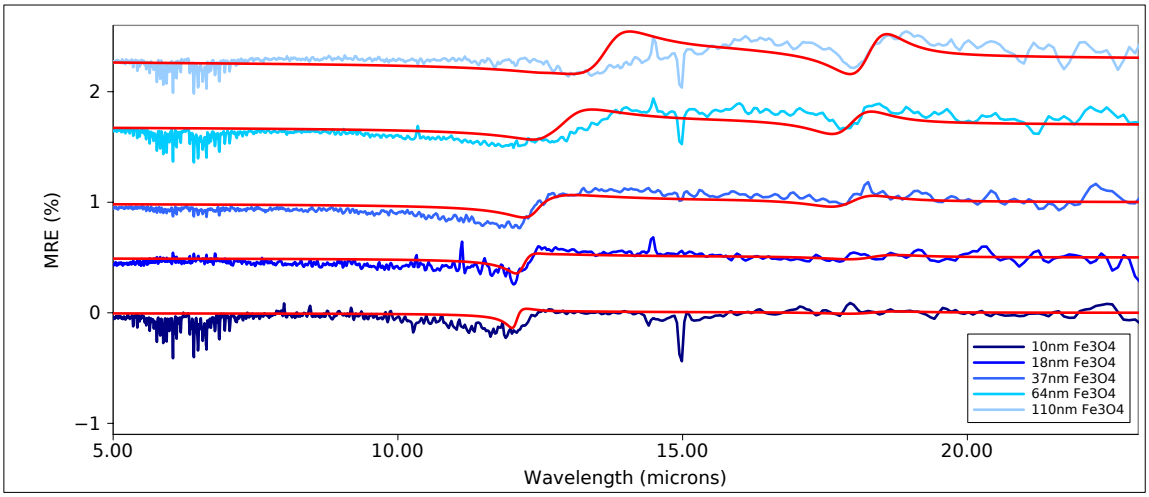

Figure 4.17: Stacked experimental and simulated MRE spectra for Fe_3O_4 films of increasing thickness, where the location of the Fe_3O_4 phonon resonance has been shifted by 0.05 μm when the magnetic field is applied. The behaviour of the additional spectral feature at 18.5 μm is accurately reproduced by this simple modification to the model.

4.4 Conclusions

A series of Fe_3O_4/MgO thin films of thickness 10, 18, 37, 64, 110 nm were grown by MBE. The reflectivity of these Fe_3O_4 films was successfully reproduced using a multiple reflection model as a function of thickness. It has been demonstrated that the Fe_3O_4 phonon resonance at 18.5 μm occurs at shorter wavelengths in these thin films, linearly approaching the bulk value (at ∼145 nm) with increasing thickness. This is possibly due to a strained portion of the film at the substrate in each film having a different phonon energy, the effect of which decreases in importance as more unstrained material is deposited above it, causing a shift in phonon position towards the bulk value with increasing thickness and strain. Such measurements could prove to be a useful, very quick way of estimating the film thickness from its reflectivity spectrum. The MRE spectra of the Fe_3O_4 films can be reasonably reproduced by using $h^2 = 1 \times 10^{-4}$ as the conductivity difference in the applied magnetic field, suggesting the value of the fitting parameter is $\eta \sim 1$. If a sufficiently large magnetic field could be applied in order to saturate the films then the exact value of η could be determined, perhaps reinforcing the claim that the scaling parameter is almost unity. However, magnetic fields of the strength required are not available in York, so the one-to-one correlation between the MRE and MR is strongly suggested but not conclusively demonstrated. The simulated MRE spectra were produced by assigning the magnetic field dependence to the hopping term, whereas previous work had assigned the dependence to the Drude term. The simulated spectra were in reasonable agreement with

the experimental spectra, suggesting this approach is valid. An additional experimental MRE spectral feature that becomes more prominent with increasing thickness was reproduced in the model by introducing a slight (0.05 μm) shift in the Fe_3O_4 phonon position with the field. This observation was unexpected and could be an interesting opportunity for further investigation. These results demonstrate the potential for using the MRE technique for probing the underlying magnetoelectronic properties of thin film oxides in a quick and non-destructive way.

Chapter 5

Spatially Resolved Variations in Reflectivity Across Iron Oxide Thin Films

The performance of a spintronic device is extremely sensitive to its microstructure. For a Fe_3O_4 based device, small variations in chemical composition can change the magnetic properties of the device. Contaminant oxide phases in Fe_3O_4 based devices lead to a reduction in spin polarisation, leading to device failure. In this chapter, the variation in oxide composition across several Fe_3O_4 thin films, produced by different deposition methods, is measured using IR reflection microspectroscopy at the SOLEIL synchrotron. Where a significant variation in composition is observed in a sample, IR reflectivity modelling is used in an attempt to establish which oxide phases are present and in what relative concentrations. This modelling is an extension of the work in chapter 4. IR reflection microspectroscopy is presented as a quick, reliable way of determining the quality of an Fe_3O_4 thin film with spatial resolution. Complementary magnetometry and TEM data is presented to support the microspectroscopy conclusions.

5.1 General comments on obtaining and analysing the reflection spectra

The reflection spectra discussed in this chapter were taken with the IR microscope on the SMIS beamline at the SOLEIL synchrotron, using the techniques outlined in section 3.3. Reflection spectra were taken over the range $1.5 - 20.0$ μm with a spot diameter of 20 μm.

In order to eliminate contaminant peaks from atmospheric sources (and from within the detector itself) it is necessary to normalise the spectra against a gold reference spectrum. Gold is highly reflective across the spectral range being used and has no spectral features, making it an ideal normalisation standard. Once normalisation has removed unwanted spectral features, the remaining features will be due to the film. There are several iron oxide phonon resonances in this spectral range, shown in table 5.1. The locations of these resonances are marked on each of the plots of reflection spectra to make determination of which oxides may be present simpler.

Oxide	**Formula**	**Position (cm^{-1})**
haematite	α-Fe_2O_3	437 525
maghemite	γ-Fe_2O_3	440 550
magnetite	Fe_3O_4	540

Table 5.1: The locations in wavenumbers of characteristic phonon resonances of α-Fe_2O_3, γ-Fe_2O_3 and Fe_3O_4.

5.2 Variations in reflectivity across post-oxidised Fe_3O_4/MgO thin films with annealing timescale

5.2.1 Preparing Fe_3O_4/MgO thin films by post-oxidisation

The first series of three Fe_3O_4 thin films under consideration were grown by MBE in York by the author, with the assistance of Dr. Siew Wai Poon, by the the post-oxidation technique outlined briefly in section 3.1.1. 20 nm iron films were deposited at 1.5 Åmin^{-1}. The films were then subsequently annealed in an atmosphere of molecular oxygen at a partial pressure of 5×10^{-5} mbar at 320 °C. The samples were annealed for 15, 44 and 60 minutes respectively so they could be used to determine if the post-oxidising time affects the quality of the film produced. It was previously noted that the oxidation process is self-limiting and only the top 3 nm of the sample will oxidise, therefore it is expected that there will be a strong metallic reflectivity contribution from the iron for all three samples. The samples are unpatterned and intended to be uniform.

5.2.2 Maps of reflectivity across films with different annealing times

Description of map for post-oxidised samples

Ten reflection spectra were recorded at different positions on the sample, with a spot diameter of 20 μm. The first seven spectra were taken in a line along the length of the sample, with each spectrum separated from its neighbours by 0.1 mm. To test that this was representative of the rest of the sample, three additional spectra were obtained from another part of the sample roughly 1 mm away, which were also separated by 0.1 mm. A diagram of this map is given in figure 5.1.

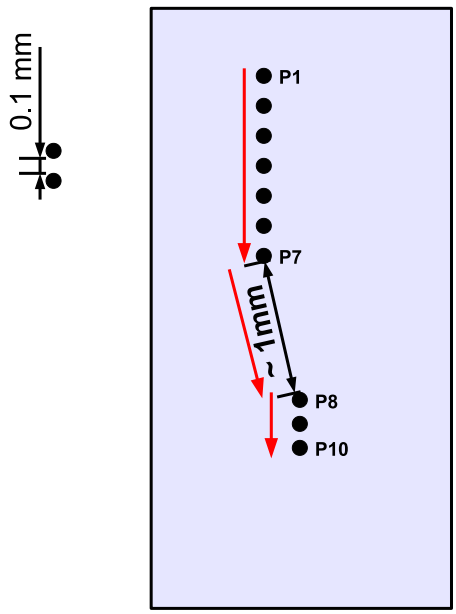

Figure 5.1: Map of the reflection spectra obtained for the post-oxidised samples. Ten spectra were taken in total in two parts of the sample to test that the spectra obtained were representative of the whole sample.

Reflectivity maps for the sample post-oxidised for 15 minutes

Figure 5.2 shows the ten reflection spectra obtained from the sample post-oxidised for 15 minutes. It can be seen that there is little variation between the spectra, suggesting that

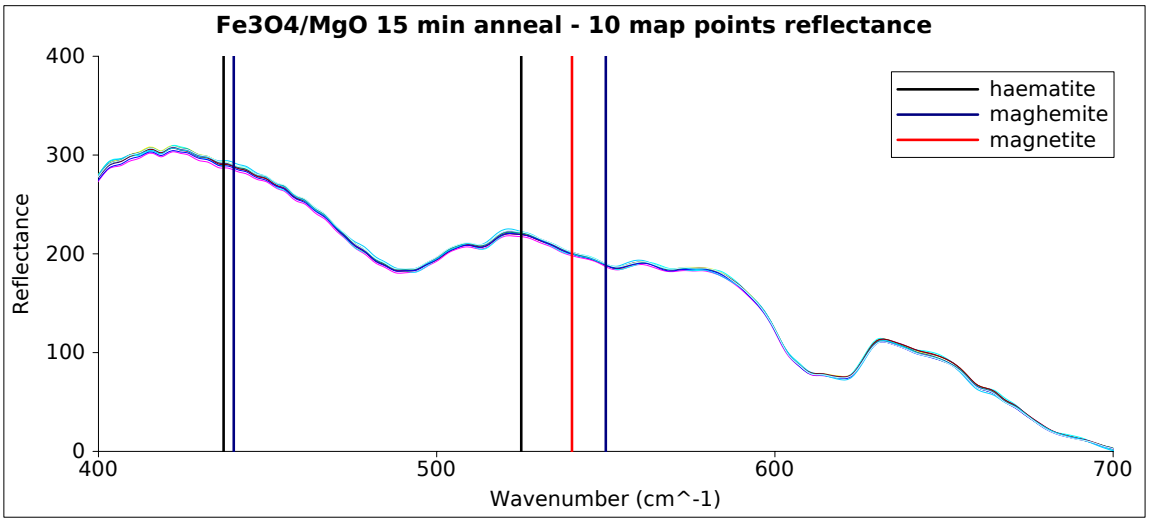

Figure 5.2: Spectra taken at ten points across the post-oxidised Fe_3O_4 thin film that was annealed for 15 minutes. The ten spectra are almost identical suggesting there is little reflectivity variation across the film.

the sample has a uniform composition across a large area. Normalising the ten spectra to the gold produces the spectra shown in figure 5.3. There is no significant spectral feature at any of the locations indicated. There are some small contaminant peaks beyond 600 wavenumbers but otherwise the spectra are all very similar and very flat.

Reflectivity maps for the sample post-oxidised for 44 minutes

For the sample annealed for 44 minutes, a similar result is found. From figure 5.4, there is again no obvious differences between any of the ten reflectivity spectra, with the spectra all being very flat and metallic. The contaminant peaks however are more prominent, suggesting that the extra annealing time does not promote better quality oxide formation but does allow for more contaminants to form at the film surface.

Reflectivity maps for the sample post-oxidised for 60 minutes

The reflection spectra from the sample which was annealed for 60 minutes are almost identical to those taken from the sample annealed for 44 minutes. This suggests that at some time between 15 and 44 minutes the contamination of the surface is complete and no further damage to the surface is possible.

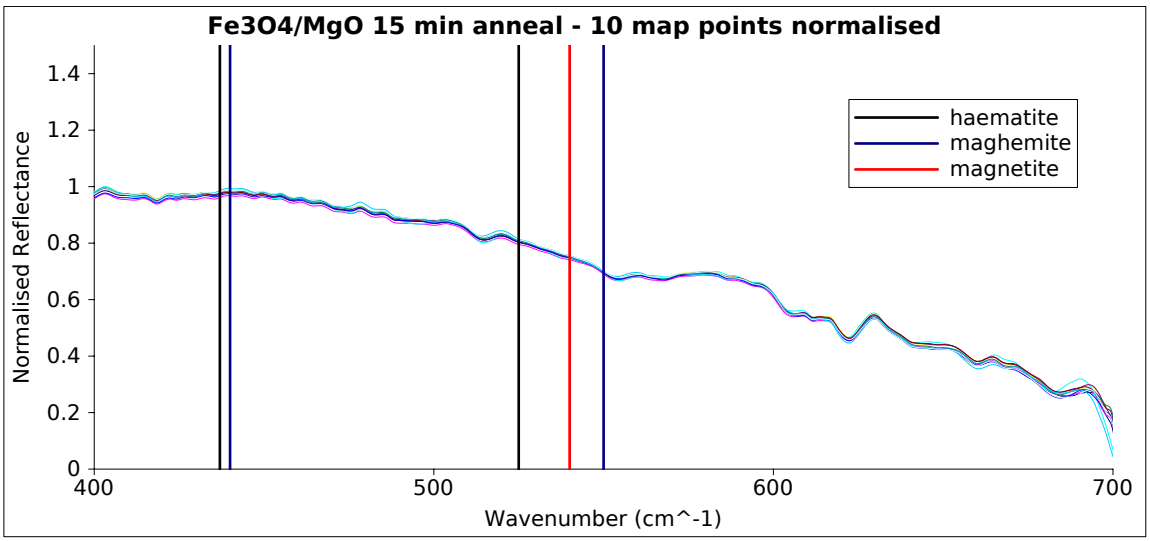

Figure 5.3: Normalised spectra taken at ten points across the post-oxidised Fe_3O_4 thin film that was annealed for 15 minutes. The normalisation reveals that there are no major spectral features and that the spectra are all flat with some contaminant peaks. This suggests that there is very little oxide formation and the spectrum is being dominated by the strongly reflecting iron.

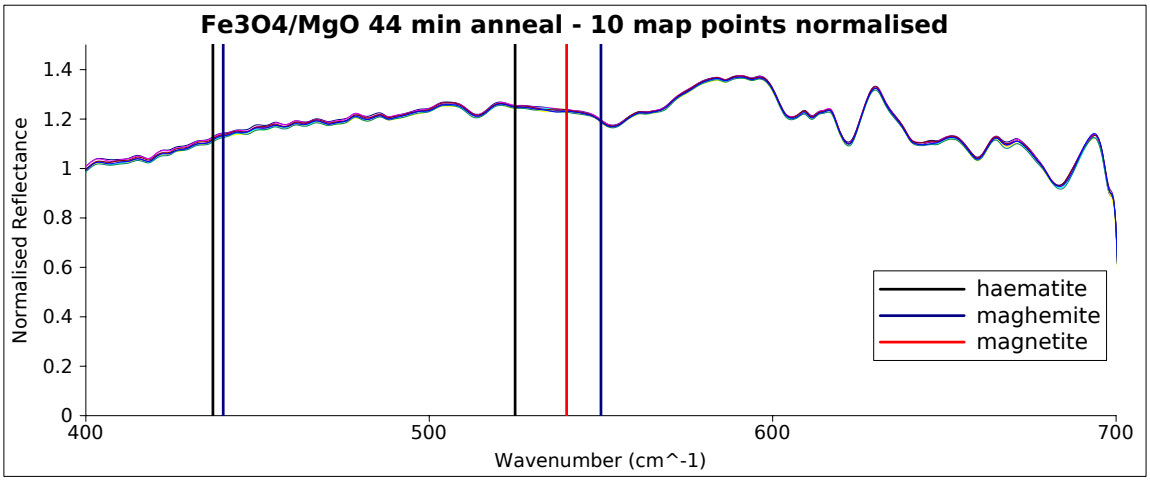

Figure 5.4: Normalised spectra taken at ten points across the post-oxidised Fe_3O_4 thin film that was annealed for 44 minutes. The spectra are free of iron oxide and have more prominent contaminant peaks than the sample which was annealed for 15 minutes. There is almost no variation between the ten spectra.

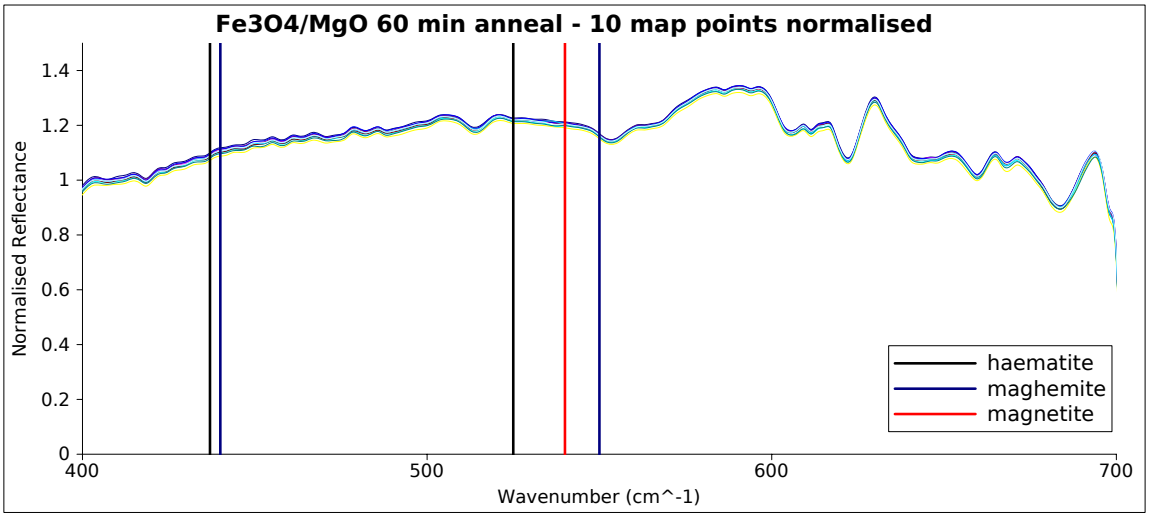

Figure 5.5: Normalised spectra taken at ten points across the post-oxidised Fe_3O_4 thin film that was annealed for 60 minutes. The spectra are almost identical to those from the sample annealed for 44 minutes, suggesting that there is a limit to how contaminated the surface can become.

5.2.3 Differences in composition across samples determined by peak height analysis

The percentage difference between P1 from the sample annealed for 15 minutes and the samples annealed for 44 and 60 minutes was calculated to quantify the differences between the reflection spectra of the samples. For each sample, all of the spectra taken at different points are very similar, so P1 was chosen arbitrarily. It can be seen from figure 5.6 that the samples annealed for 44 minutes and 60 minutes have very similar reflection spectra, while the sample annealed for 15 minutes has a very different reflection spectrum, having a steadily reducing reflectivity with increasing wavenumber. The variation between the samples annealed for 15 and 60 minutes can't be caused by changes in the contaminant oxide concentration as there is no difference in peak height, the variation is very linear.

In order to highlight any differences between the various spectra taken from the sample annealed for 15 minutes, the spectra were subtracted from each other to determine if there were any slight changes in peak heights between spectra. The difference between the spectra taken at points 2-9 and the spectrum at point 1 was expressed as a percentage $\left(\frac{R_{\mathrm{p}x}-R_{\mathrm{p1}}}{R_{\mathrm{p1}}} \times 100\%\right)$ and plotted in figure 5.7. There is no variation with peak height visible above the noise, although there is some drift at long wavenumbers. Similar conclusions can be drawn for the samples annealed for 44 minutes and 60 minutes but the spectra are

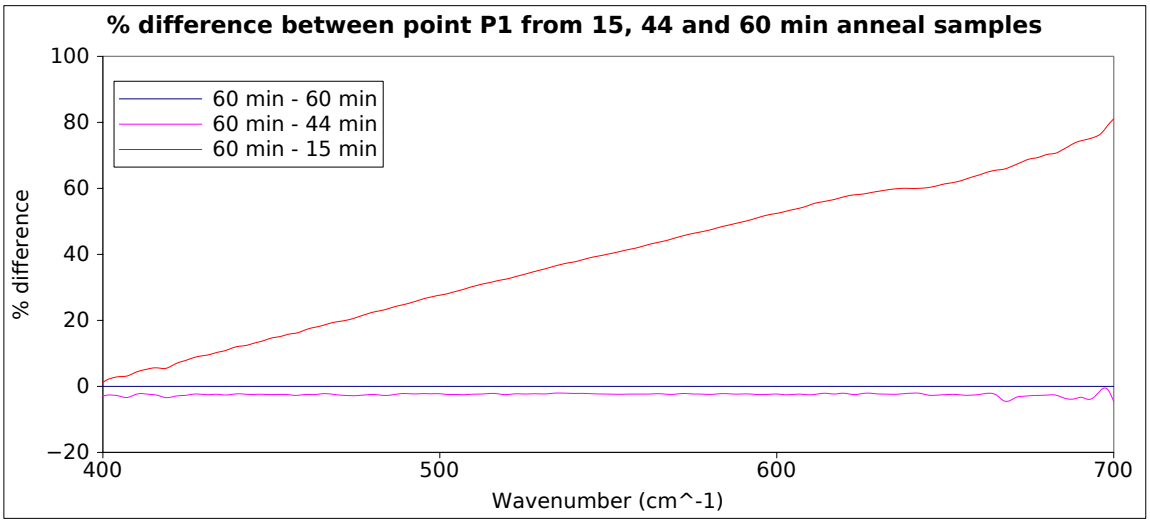

Figure 5.6: Percentage difference between spectrum P1 from the sample annealed for 60 minutes and the samples annealed for 15 and 44 minutes. It can be seen that the 44 and 60 minutes samples are very similar but the reflectivity spectrum of the sample annealed for 15 minutes is very different, with a much lower reflectivity with increasing wavenumber.

not produced here for brevity.

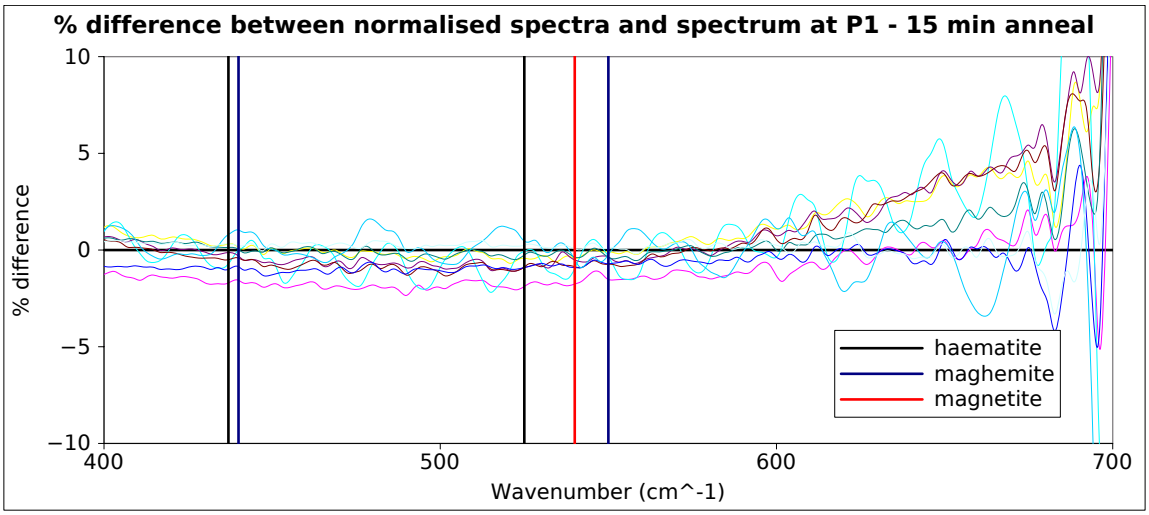

Figure 5.7: Plot of the difference between spectra from points 2-9 and the spectrum from point 1 expressed as a percentage. There is no variation observable above the noise.

5.2.4 Supplementary characterisation by VSM and TEM

The hysteresis loop for the sample annealed for 15 minutes is given in figure 5.8. The loop has very low coercivity and a large remanent magnetisation, characteristic of an iron hysteresis loop. This hysteresis loop would suggest that the magnetic behaviour of the sample

is being dominated by the presence of a large quantity of iron present in the film. This argument is supported by the TEM micrograph presented in figure 5.9. The micrograph shows that this region of the film is approximately 75% iron which has not been oxidised, while there is a layer of Fe_3O_4 on the surface, comprising 25% of the total film. It is important to note that this micrograph only shows an approximately 22 nm section of the sample, which is two orders of magnitude lower than the resolution of the IR microscope, so gives very localised information and may not be representative of the entire sample.

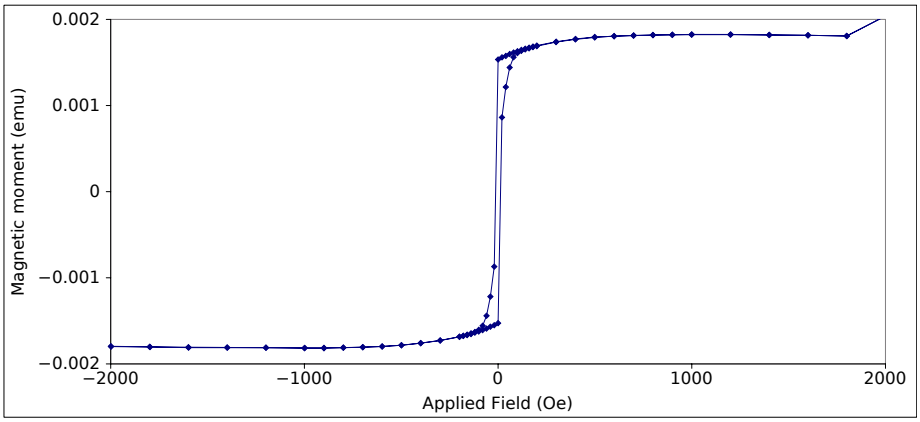

Figure 5.8: Magnetometry data for the sample annealed for 15 minutes. The hysteresis loop has a low coercivity and high remanence, indicating that the signal produced is dominated by the presence of iron in the film. Image courtesy of Mr. James Sizeland.

5.2.5 Modelling the reflectivity of the sample annealed for 15 minutes

Using the multilayer reflectivity model discussed in detail in chapter 4 the reflectivity of the sample annealed for 15 minutes was simulated, shown in figure 5.10. The simulation assumes the 75% Fe and 25% Fe_3O_4 split implied by the TEM data. Reflectivity spectra where the film is composed entirely of iron and entirely of Fe_3O_4 are presented on the same plot for comparison. The simulated spectrum of the sample is very flat, consistent with the experimental spectra. The Fe_3O_4 spectral feature is very weak in the simulation, in agreement with the prediction that the presence of a large quantity of iron would wash out the reflectivity contribution of the oxide at the surface. As the sample is only 20 nm thick, there is a significant, broad absorption from the substrate at $\sim 640\,\mathrm{cm}^{-1}$ which is not observed in the experimental spectra. However, the film thickness estimated from the TEM results is ~ 7 nm greater than the growth thickness, due to an oxygen plane being inserted between each plane of iron atoms in the oxide layer, so this is unsurprising.The general

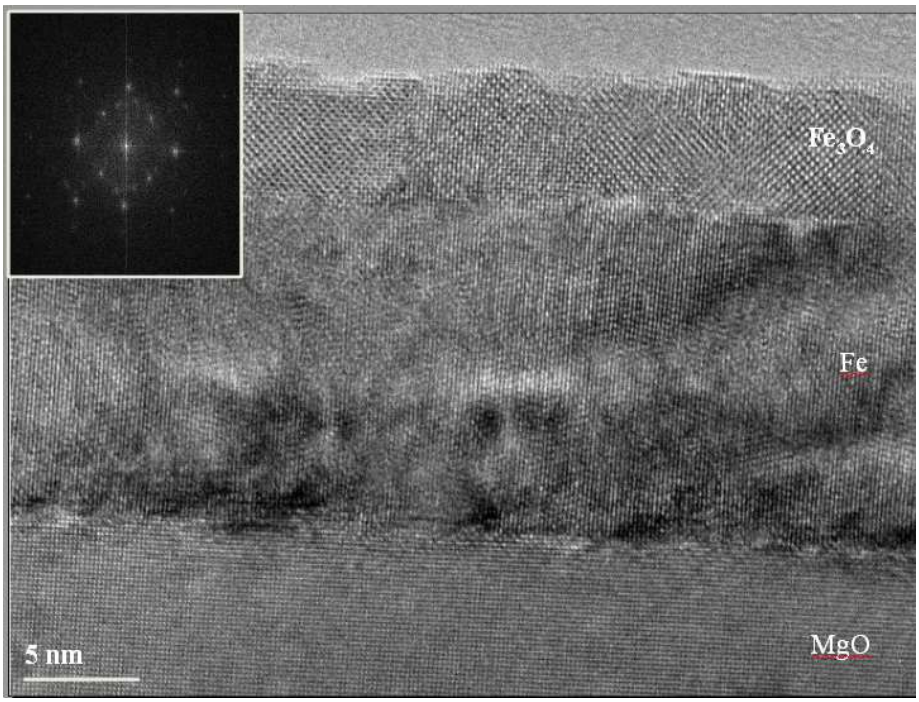

Figure 5.9: TEM micrograph showing the sample annealed for 15 minutes is 75% unoxidised iron with a small layer of Fe_3O_4 at the surface. Image courtesy of Mr. Daniel Gilks. The inset diagram is the electron diffraction pattern of the surface layer and is of Fe_3O_4.

trend of decreasing reflectivity beyond $\sim 600\,\mathrm{cm}^{-1}$ is seen in both the experimental and simulated spectra.

5.2.6 Summary

Ten reflection spectra were taken at points along a line separated by 0.1 mm from Fe_3O_4 thin films that had been annealed for 15, 44 and 60 minutes. There was no variation in reflectivity observable across any of the samples. All three samples were featureless, suggesting that there is a strong enough metallic reflectivity contribution to wash out any oxide absorption features. This supports the hypothesis that the post-oxidation is self-limiting in depth and only oxidising a few nanometres down into the iron film. For the sample annealed for 15 minutes, the magnetometry data strongly suggests a film comprised mostly of iron. The TEM data shows conclusively that the film is 75% Fe with 25% Fe_3O_4 as a surface layer, as well as demonstrating that the ratio of iron to Fe_3O_4 is roughly constant across this 20 nm section, potentially explaining the lack of variation in reflectivity across the film. A simulated reflectivity spectrum for the sample annealed for 15 minutes was produced, which was flat with very weak absorption features like the experimental

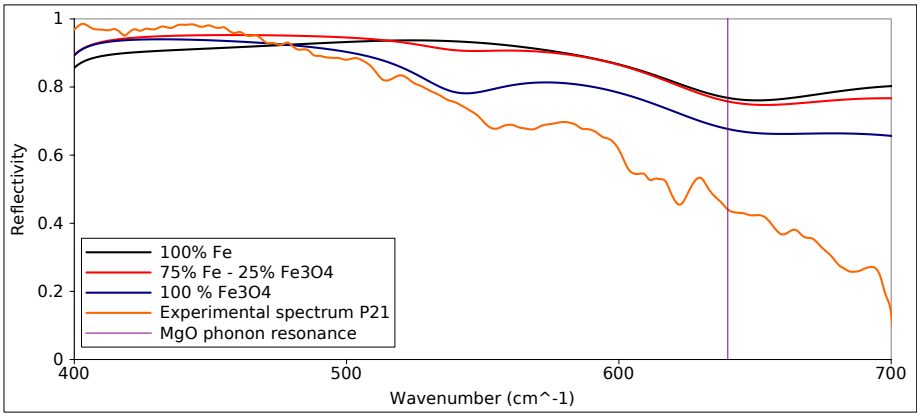

Figure 5.10: Simulated reflectivity spectrum of the sample annealed for 15 minutes (75% iron - 25% Fe_3O_4). The Fe_3O_4 absorption in the simulated spectrum is very weak, suggesting that at this sample thickness and iron/Fe_3O_4 ratio the iron reflectivity is washing out the reflectivity contribution of the oxide.

spectra.

5.3 Reflectivity variation across an Fe_3O_4/MgO thin film deposited by simultaneous-oxidation

5.3.1 Preparing Fe_3O_4/MgO thin films by simultaneous-oxidisation

An Fe_3O_4 thin film was grown by MBE in York by the author, with the assistance of Dr. Siew Wai Poon, by the the simultaneous-oxidation technique outlined briefly in section 3.1.1. A 60 nm iron film was deposited at 1.1 Åmin^{-1} in an atmosphere of molecular oxygen at a partial pressure of 5×10^{-5} mbar at 320 °C. As the iron is continuously exposed to oxygen from the beginning of the deposition it is expected that the film will be oxidised down to the substrate and not just the first 3 nm.

5.3.2 Description of maps for the simultaneous-oxidation sample

Three maps of reflectivity of different sized areas were produced for this sample. The first (large) map was produced as shown in figure 5.11, where each point is separated from its neighbours by 0.5 mm with a spot size of 20×20 µm. The second (medium) map, follows the same pattern as the large map but is located within the square formed by points 19-22 of the large map. The points are each separated by 125 µm. The third (small) map is

located within this square, defined from point 21. This map follows the same pattern as the first two, except there are 36 spectra and they are separated by 50 μm, which is close to the resolution of the IR microscope.

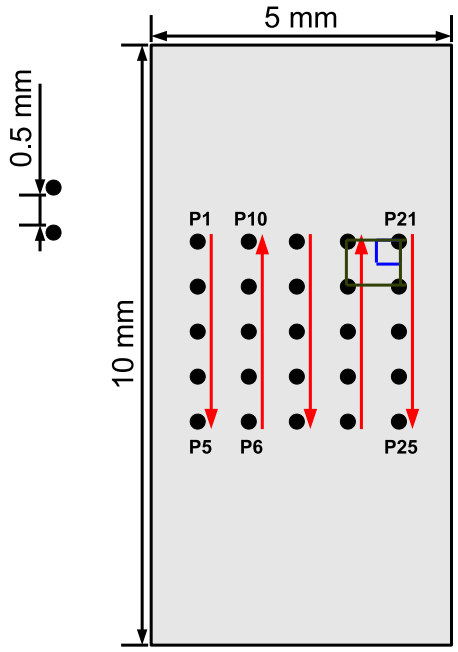

Figure 5.11: Description of the three maps (large, medium and small) produced for the simultaneously-oxidised Fe_3O_4 thin film. The large map, consisting of the 25 points shown, is a $2 \times 2\,\text{mm}^2$ grid with a 500 micron point separation. The medium map, within the black square, is a $0.5 \times 0.5\,\text{mm}^2$ grid with a 125 micron point separation. The small map, within the blue square, is a $0.25 \times 0.25\,\text{mm}^2$ grid with a 50 micron point separation. All three maps share a common point (P21).

5.3.3 Maps of reflectivity across the simultaneous-oxidation sample on different length scales

The reflectivity spectra taken from the simultaneously-oxidised sample on the large, medium and small scales described in the previous section are presented in figures 5.12, 5.13 and 5.14. It can be seen that at all three lengthscales there is significant variation in reflectivity across the sample, down to near the spatial resolution of the IR microscope. This indicates that there is a spatial variation in the composition of the sample across a large area and on small lengthscales. There is a strong absorption in the spectra at $\sim 550\,\text{cm}^{-1}$, which

is a characteristic phonon resonance of maghemite. The absorptions are not all located in the same position, the deeper the absorption feature the more the feature is shifted towards lower wavenumber. This suggests that there is a variation in the relative concentration of maghemite in the sample. Except for the location of the phonon absorption, the reflection spectra of maghemite and magnetite are similar. The variation in the depth of the feature is therefore predicted to come from a variation in the ratio of oxidised to unoxidised iron, with the spectra becoming flatter where more iron is present.

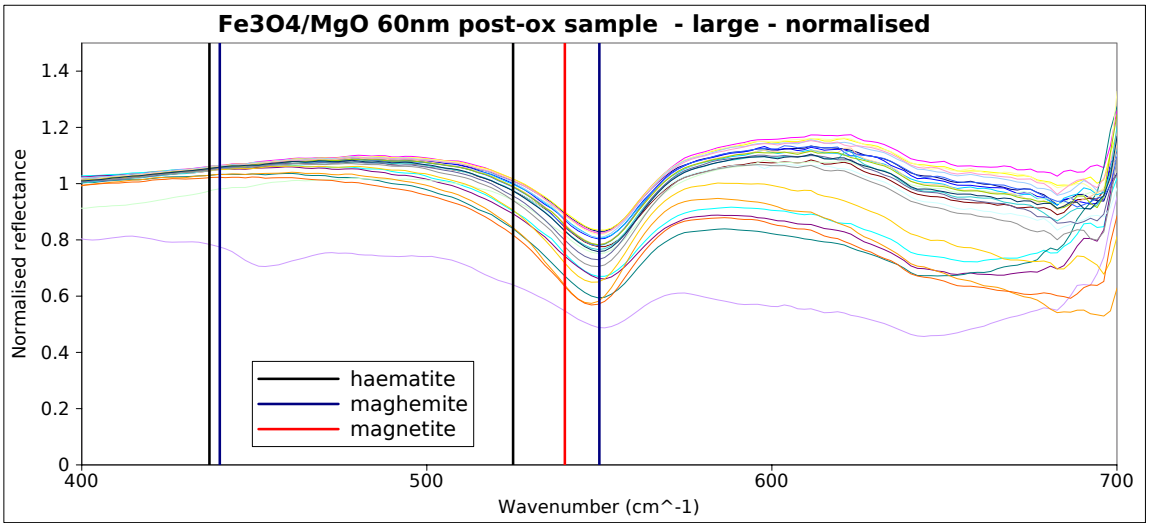

Figure 5.12: 25 reflection spectra taken in a $2 \times 2\,\mathrm{mm}^2$ grid with a 500 micron point separation. There is significant variation in reflectivity across the sample suggesting that there is a variation in sample composition across a large area. There is a strong absorption feature at $\sim 550\,\mathrm{cm}^{-1}$ indicating the presence of maghemite.

5.3.4 Differences in composition across samples determined by peak height analysis

Taking the spectra obtained for the medium sized area, the percentage difference between each spectra and the spectrum at point P21 were taken to highlight differences between the spectra. Point P21 was chosen as it is a common point for all 3 length scales. The percentage differences between the spectra, shown in figure 5.15, show that there is a variation in the depth of the absorption peak across the sample, but not in its position. This suggests that the ratio of magnetite to maghemite is reasonably constant across the sample, with a variation in the relative amount of iron to iron oxide.

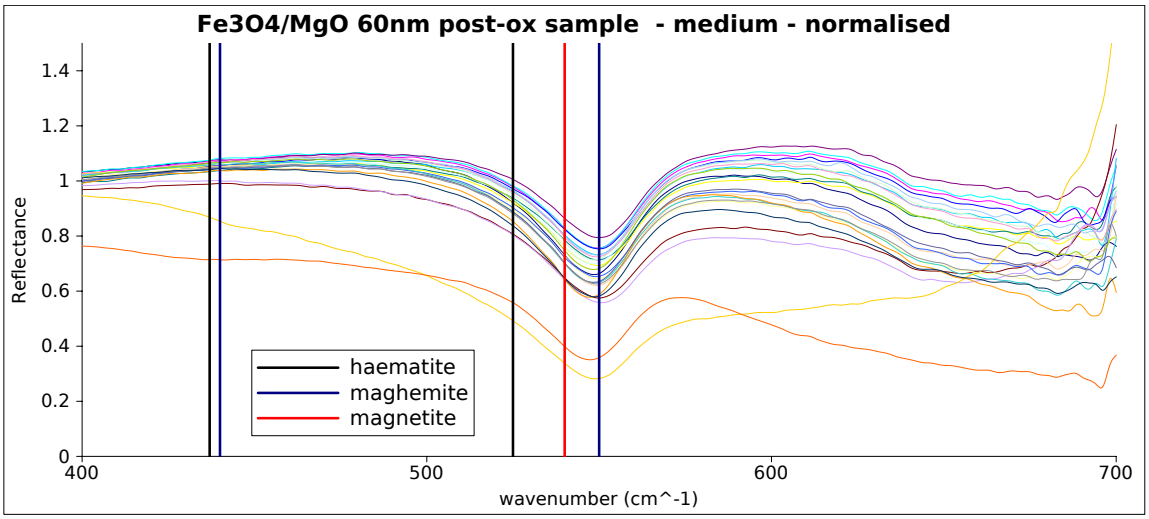

Figure 5.13: 25 reflection spectra taken in a $0.5 \times 0.5\,\mathrm{mm}^2$ grid, within the $2 \times 2\,\mathrm{mm}^2$ grid, with a 125 micron point separation. There is significant variation in reflectivity across the sample on this smaller scale.

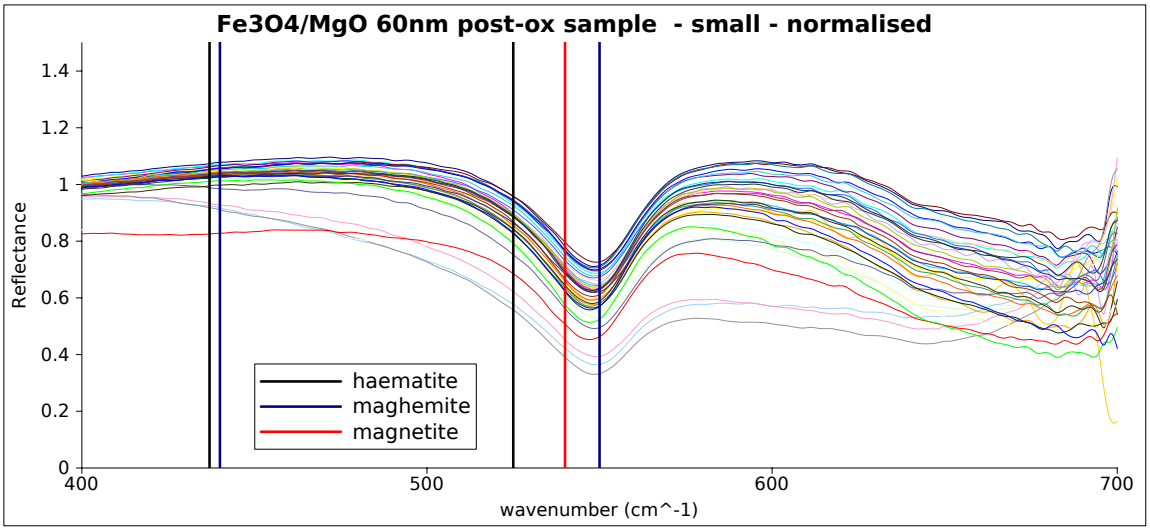

Figure 5.14: 36 reflection spectra taken in a $0.25 \times 0.25\,\mathrm{mm}^2$ grid, within the $0.5 \times 0.5\,\mathrm{mm}^2$ grid, with a 50 micron point separation. Even near the resolving limit of the IR microscope there is significant variation in reflectivity across the sample. The spectra with deeper absorption features appear to be shifted significantly towards $\sim 540\,\mathrm{cm}^{-1}$, where an Fe_3O_4 phonon absorption is expected. This suggests that there is magnetite present in this area of the sample and that the ratio of magnetite to maghemite varies spatially.

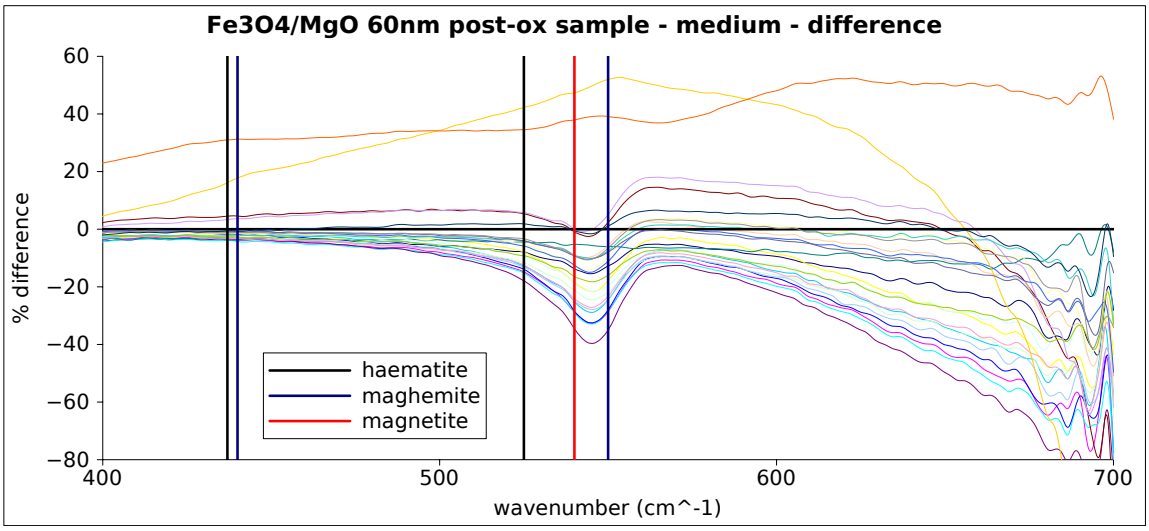

Figure 5.15: Percentage difference between each spectra and the spectrum at point P21 for the medium sized area. There is a significant variation in the depth of the absorption feature but not its position. This suggests that the ratio of magnetite to maghemite does not vary but there is a variation in the ratio of iron to iron oxide across the sample.

5.3.5 Modelling the reflectivity of the simultaneous-oxidation sample

An attempt was made to simulate the reflectivity of the sample at point 21 using the model outlined previously in chapter 4. Point 21 was chosen as it was the spectrum being used to calculate the percentage difference between the spectra. To model the reflectivity, the ratio of magnetite to maghemite was varied in order to fit the position of the absorption feature. Once the ratio of the oxides was determined, the ratio of iron to iron oxide was used to fit the depth of the spectral feature.

Estimating the ratio of oxides

An extra term was introduced into the dielectric function to incorporate the maghemite. The magnetite and maghemite dielectric functions were weighted as in equation 5.1, where f is the fraction of magnetite present.

$$\epsilon_{\text{oxide}} = f\epsilon_{\text{Fe}_3\text{O}_4} + (1-f)\,\epsilon_{\gamma-\text{Fe}_2\text{O}_3} \tag{5.1}$$

The simulated spectra in figure 5.16 demonstrate that if the ratio of magnetite to maghemite is varied then the position of the absorption features does move. The cor-

rect position for the spectral feature is achieved for a sample that is 75% Fe_3O_4 and 25% $\gamma - Fe_2O_3$. Overall, the reflectivity is underestimated in the same way as the simulations produced in chapter 4. This underestimation is unexplained so no attempt to address this is made here. It must be noted that changing the ratio of magnetite of maghemite also changes the depth of the spectral feature. This effect can be ignored in fitting the ratio of iron to iron oxide however as it has been shown that the ratio of the two oxides is not changing, so the effect must be purely due to the variation in the ratio of iron to iron oxide.

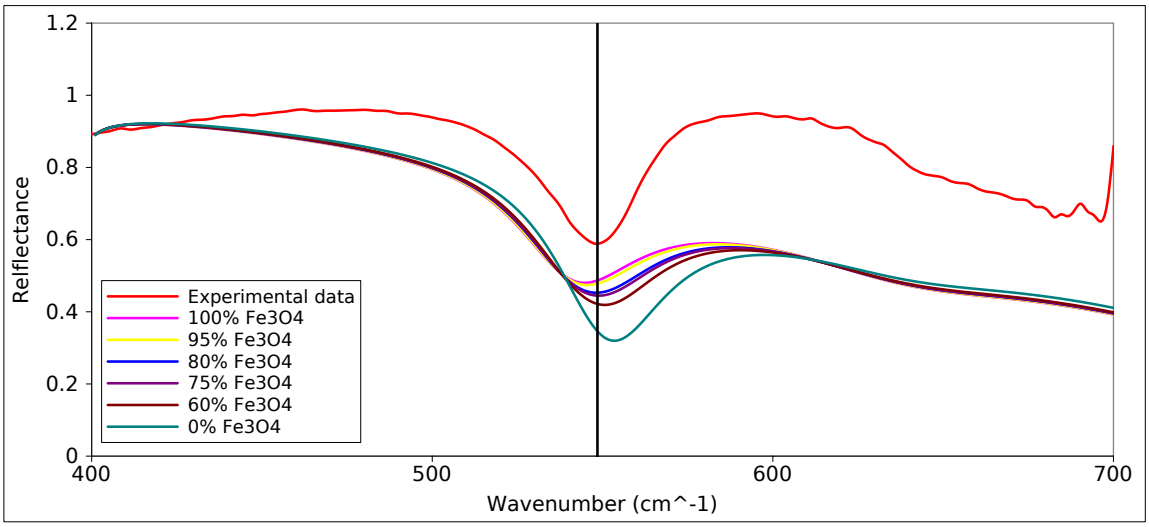

Figure 5.16: Simulated reflection spectra with different ratios of magnetite to maghemite. The position of the absorption feature is dependent on the ratio of the concentration of each oxide present. The position of the feature in the experimental spectrum is reproduced when the ratio is 75% Fe_2O_3 and 25% $\gamma - Fe_2O_3$.

Estimating the ratio of oxides to iron

The ratio of iron oxide to iron was used to fit the magnitude of the absorption feature. The iron was represented by an additional term in the dielectric function, weighted against the dielectric function contribution from the combined oxided, where f' is the fraction of iron oxide in the sample:

$$\epsilon_{\text{film}} = f'\epsilon_{\text{oxide}} + (1 - f')\,\epsilon_{\text{iron}} \tag{5.2}$$

The simulated spectra in figure 5.17 show the variation in the depth of the absorption feature with the ratio of iron to iron oxide. The experimental depth of the spectral feature

is best reproduced by a simulation with 65% oxide and 35% iron. This gives Fe(35%)γ-Fe_2O_3(15%)Fe_3O_4(50%) as an approximate composition for this point in the sample.

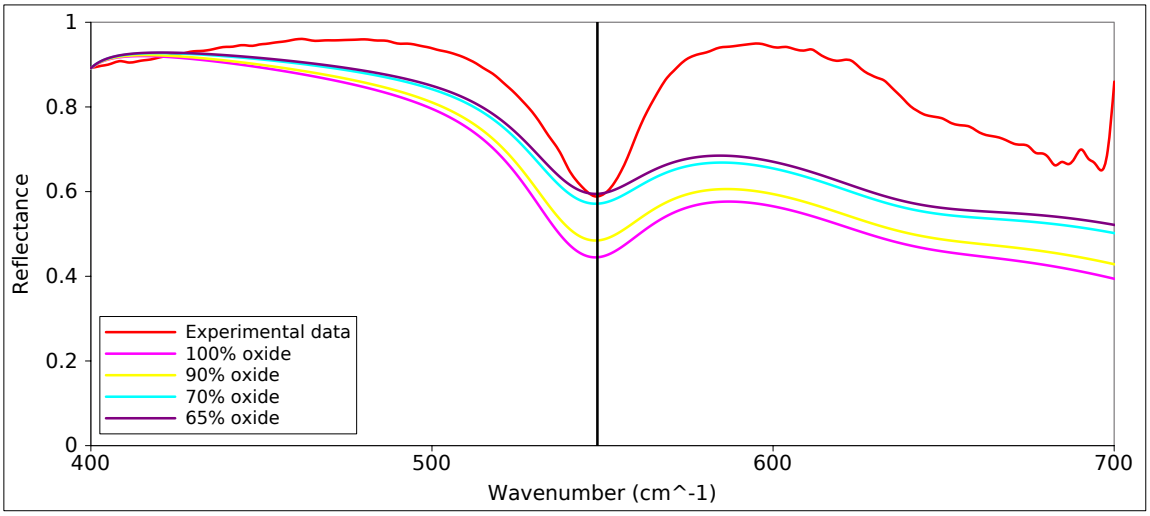

Figure 5.17: Simulated spectra with different ratios of iron oxide to iron. The depth of the absorption feature in the experimental spectrum is reproduced with 65% oxide and 35% iron.

Modelling the differences in reflectivity as a variation in iron to iron oxide ratio

In figure 5.15 the percentage difference between the spectra and the spectrum at P21 showed that there was no shift in the position of the spectral feature, so in modelling the differences between the spectra the ratio of iron to iron oxide was used to generate the variation. Figure 5.18 shows the percentage difference between the experimental spectra and the spectrum at P21. There are three simulated spectra; the difference between the simulated P21 spectrum and simulations of films with 40, 20 and 10% oxide content. The ratio of magnetite to maghemite has been kept constant in these simulations. The trend of the difference can be reproduced by varying the ratio of iron to iron oxide from 65%/35% to 80%/20%. This is a large variation in composition and would certainly lead to unwanted device properties.

5.3.6 Summary

Spatial variations in reflectivity were observed across a 60 nm Fe_3O_4/MgO thin film in a $2 \times 2\,mm^2$ area with a spatial resolution down to 50 μm. A spectral feature indicative of the presence of iron oxide was observed, which varied in both magnitude and position across

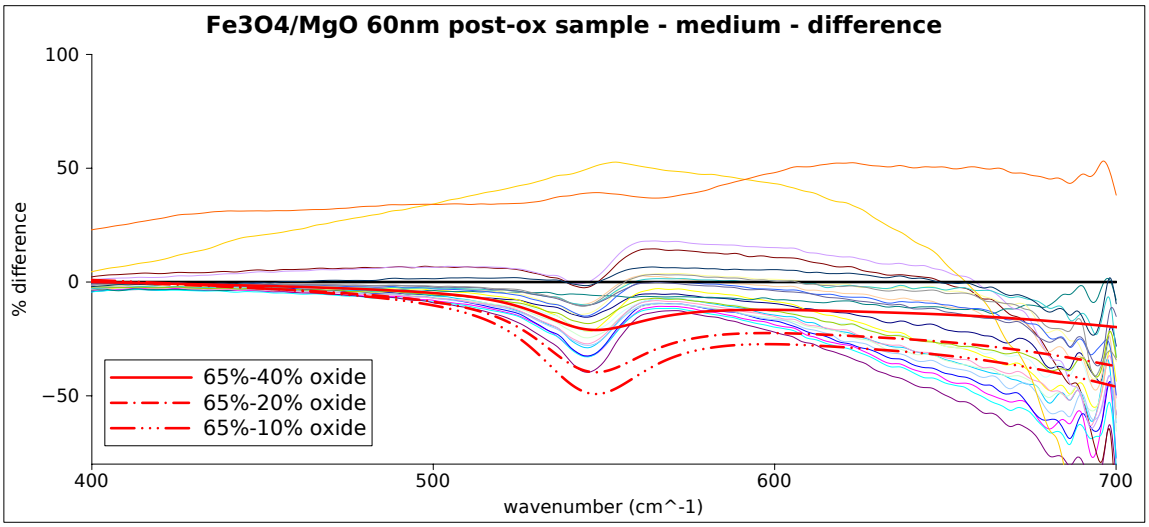

Figure 5.18: Percentage difference between the experimental spectra and the spectrum at P21 for the medium map. The percentage difference between the simulated P21 spectrum and simulated spectra with lower oxide content are also shown, demonstrating that varying the iron to iron oxide concentration reproduces the experimental trend. "$65\% - 40\%$ oxide" means the difference between a simulated spectrum with 65% oxide/35% iron and a simulated spectrum with 40% oxide/60% iron composition.

the film, indicating a variation in the composition of the sample. Modelling the reflectivity spectra of the 21st point on the sample allowed an estimate of the composition of the film at that point to be calculated. By taking the difference between the simulated spectrum at point P21 and spectra with different ratios of iron to iron oxide the experimental trend of varying reflectivity could be reproduced.

5.4 Reflectivity variation across an Fe_3O_4/YSZ thin film

5.4.1 Preparing an Fe_3O_4/YSZ thin film by pulsed laser deposition

An Fe_3O_4 thin film was deposited using pulsed laser deposition by Dr. Kosuke Matsuzaki of the Tokyo Institute of Technology, Japan. A KrF laser was used to ablate a sintered Fe_3O_4 target onto an yttrium stabilised zinc oxide (YSZ) substrate. 100 nm of Fe_3O_4 was deposited in 2×10^{-6} mbar partial pressure of molecular oxygen at 300 °C. The sample was subsequently annealed in 2×10^{-6} mbar at 1200 °C. The sample is unpatterned so it was expected to be uniform.

5.4.2 Description of the map for Fe_3O_4/YSZ deposited by PLD

Seven reflection spectra were recorded at different positions on the sample, with a spot diameter of 20 μm. The spectra were taken in a line along the length of the sample, with each spectrum separated from its neighbours by 0.1 mm. A diagram of this map is given in figure 5.19.

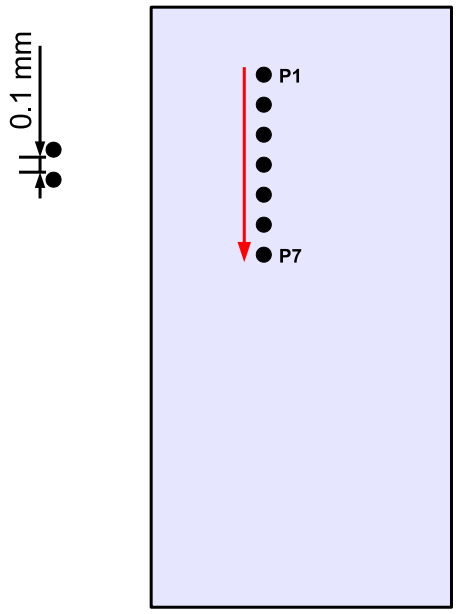

Figure 5.19: Map showing the positions of the seven reflection spectra recorded from the Fe_3O_4/YSZ thin film.

5.4.3 Map of reflectivity across the sample

Normalising the spectra to the gold reference spectrum produces the seven spectra shown in figure 5.20. It can be seen that there is little to no variation in reflectivity across the sample, suggesting it is highly uniform. There is a strong absorption at 540 cm^{-1}, the location of a TO phonon mode in Fe_3O_4. There is a smaller feature at ∼620 cm^{-1} due to the YSZ substrate. These spectra suggest that the film consists primarily of Fe_3O_4 with almost no contaminant oxide present.

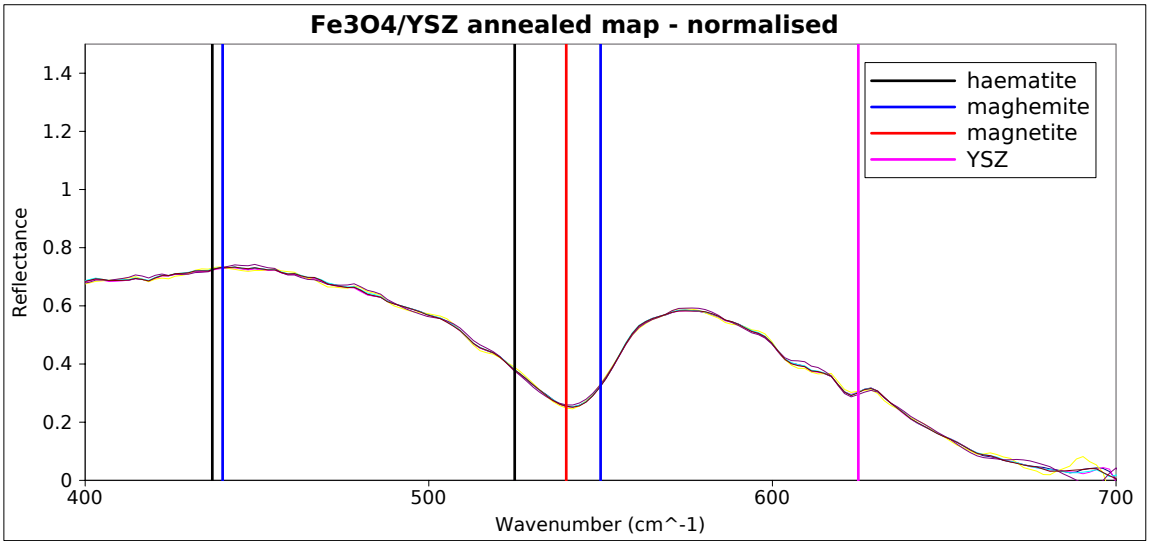

Figure 5.20: Normalised reflection spectra taken from the Fe_3O_4/YSZ thin film. There is a very strong absorption at 540 cm^{-1} indicating the film is composed of Fe_3O_4.

The difference between the spectra taken at points 2-7 and the spectrum at point 1 was taken in order to see if there was any variation in the strength of the absorption across the sample, shown in figure 5.21. There is no variation observable above the noise. The IR microspectroscopy for this sample suggests that this Fe_3O_4/YSZ thin film is composed of Fe_3O_4 and is highly uniform, making it ideal for spintronic applications.

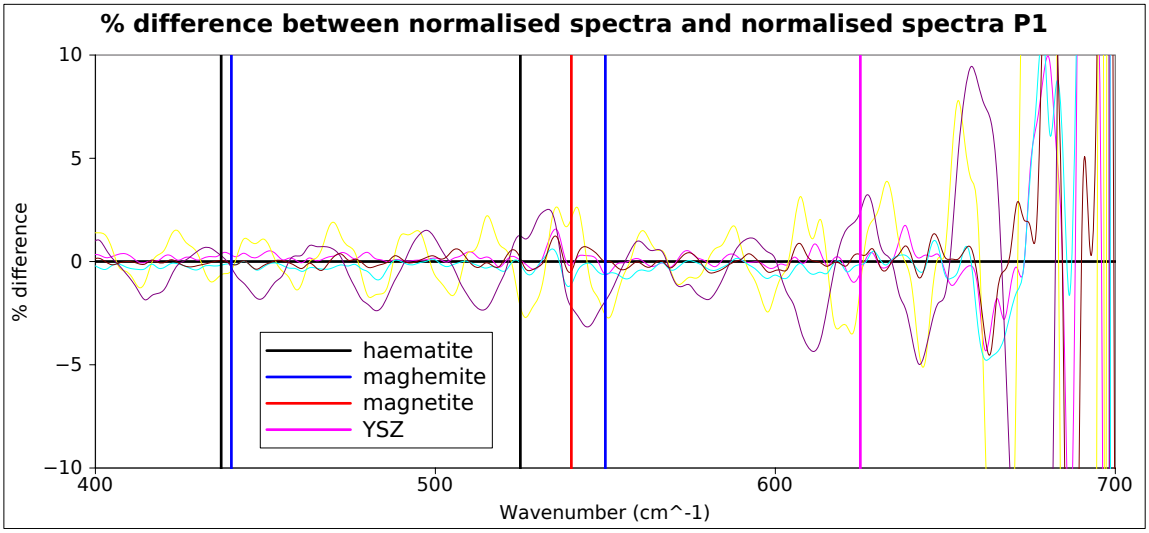

Figure 5.21: Difference between reflection spectra taken at points 2-9 and point 1. There is no change in the strength of the absorption, indicating that the film is comprised of highly uniform Fe_3O_4.

5.4.4 Supplementary characterisation by TEM

The TEM micrograph in figure 5.22 was obtained by Dr. Vlado Lazarov and Dr. Leonardo Lari and is reproduced from the work of Matsuzaki *et al*[76]. The micrograph clearly shows a highly uniform Fe_3O_4 structure down to the atomically sharp interface with the substrate. This confirms the observation in the IR spectroscopy that there is no variation across the sample and it is comprised of highly uniform Fe_3O_4.

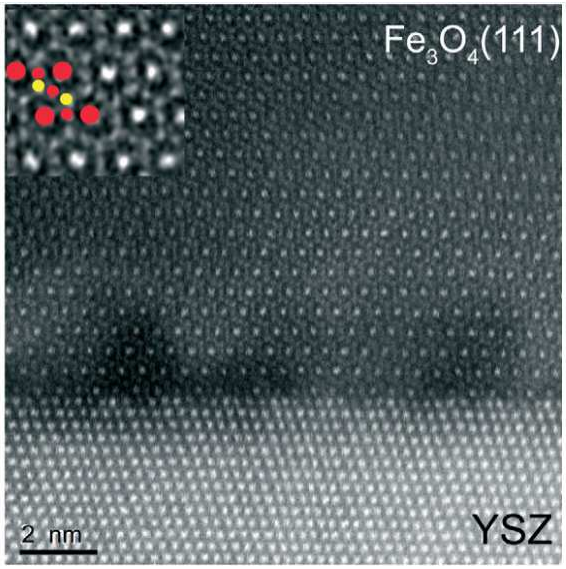

Figure 5.22: TEM micrograph of the Fe_3O_4/YSZ thin film, reproduced from the work of Dr. Kosuke Matsuzaki[76]. The micrograph shows the Fe_3O_4 film is uniform and free of contaminant phases up to the atomically sharp interface with the YSZ substrate.

5.4.5 Summary

Seven reflection spectra were taken from different points across an Fe_3O_4/YSZ film. All the spectra were identical and showed a strong absorption feature at 540 cm^{-1} which is indicative of Fe_3O_4. TEM data from this sample shows that the film is oxidised uniformly to Fe_3O_4 down to the substrate, where the interface is atomically sharp.

5.5 Conclusions

Three Fe_3O_4 thin films were produced by post-oxidation, one by simultaneous-oxidation and one by PLD. Reflectivity spectra, obtained at the SOLEIL synchrotron, were taken

at several points across each sample. This was done in an attempt to determine the composition of the samples and also to try and observe any spatial variations in reflectivity, which could be linked back to the film structure. The reflectivity spectra observed demonstrated that the post-oxidised films were $\sim 75\%$ iron with an Fe_3O_4 layer at the surface, contributing to 25% of the films thickness as expected. Simulated reflection spectra with this composition ratio, magnetometry and TEM all support this conclusion. There was significant variation in reflectivity across the simultaneously-oxidised sample, over a large area and on a length scale close to the resolving limit of the IR microscope. Through modelling the variation in the reflectivity it was possible to estimate the composition of the sample at point 21; Fe(35%)γ-Fe_2O_3(15%)Fe_3O_4(50%) .The trends in the variation of reflectivity across the sample could be reproduced by varying the ratio of iron to iron oxide from 65%/35% to 80%/20%, while keeping the ratio of Fe_3O_4 to γ-Fe_2O_3 constant. There was no reflectivity variation observed across the sample deposited by PLD and all the spectra showed a strong Fe_3O_4 absorption feature, strongly indicating the sample is highly uniform Fe_3O_4. The TEM data confirmed the IR microspectroscopy observations, showing a highly ordered Fe_3O_4 film down to an atomically sharp substrate. Post oxidation has been shown to produce an oxide layer of limited thickness, although such a layer was shown to be uniform across the sample. This suggests post oxidation is only useful for growing Fe_3O_4 films thinner than $\sim 5\,$nm. Simultaneous oxidation was shown to produce a film which is predominately oxidised but to more than one oxide phase, with the amount of oxidation varying across the sample. This suggests that it may be possible to grow Fe_3O_4 by this technique but not with the growth conditions used. A systematic study of various growth conditions must be undertaken to determine conclusively if this technique can produce device quality films. PLD was shown to produce high quality uniform films, although this technique is not currently available in a laboratory at York. The IR microspectroscopy was capable of estimating the film composition, as well as what the variation in the composition was across the samples, with a quick, straightforward and non-destructive measurement. In all three of these very different cases, the IR microspectroscopy proved an excellent indicator of both film composition and film quality, demonstrating it is a very powerful technique for characterising magnetic thin films.

Chapter 6

Spatially and Spectrally Resolved MRE Measurements of GMR Multilayers at the SOLEIL Synchrotron

In chapter 5, IR microspectroscopy was demonstrated to be a powerful technique for characterising the spatial variation in chemical composition of a material. In this chapter, magnetic field-dependent IR microspectroscopy is used to probe the magnetotransport of GMR materials. A gradient in MR was created in a CoFe/Cu multilayer by controlled annealing in a furnace. The multilayer was characterised using an electrical four-point probe measurement to establish its average MR, as well as with an IR camera to demonstrate there was a variation in MR across the multilayer. The MRE measurement performed with the IR microscope is used to provide both the spectral information needed to model the system, as well as the important spatial resolution. By modelling the MRE of the multilayer it is possible to investigate the underlying mechanism of the MR, which is impossible with a conventional four-point probe measurement.

6.1 Preparing a sample with a spatial variation in MR

The samples used in this study were $[CoFe_{1.5\,nm}/Cu_{1.2\,nm}]_{25}/TaN_{7\,nm}$ multilayers provided by Seagate Technology. In order to investigate variations in MR across a material it was necessary to produce a sample where there was a controlled variation in MR. A multilayer with an MR gradient was produced by annealing a multilayer in a furnace at 450 °C for 20 minutes in an argon atmosphere, as shown in the schematic diagram in figure 6.1, by Matthew Illman as part of his undergraduate final year project. A temperature gradient

was established across the sample by attaching a a conducting metal plate to one side of the sample. The conducting metal plate acts as a heat sink, creating a gradient in temperature across the sample. The multilayer has already been optimised by Seagate by controlled annealing at low temperature. These samples were part of a series provided by Seagate with different annealing temperatures with the multilayers annealed at 450 °C and above showing a reduced MR. Annealing the multilayer at 450 °C will cause damage to the sample, with regions of the sample at higher temperature experiencing greater damage (and a reduced MR) than those regions at lower temperature. This creates a gradient in MR across the sample, with high MR in the coolest region near the heat sink and a low MR away from the heat sink.

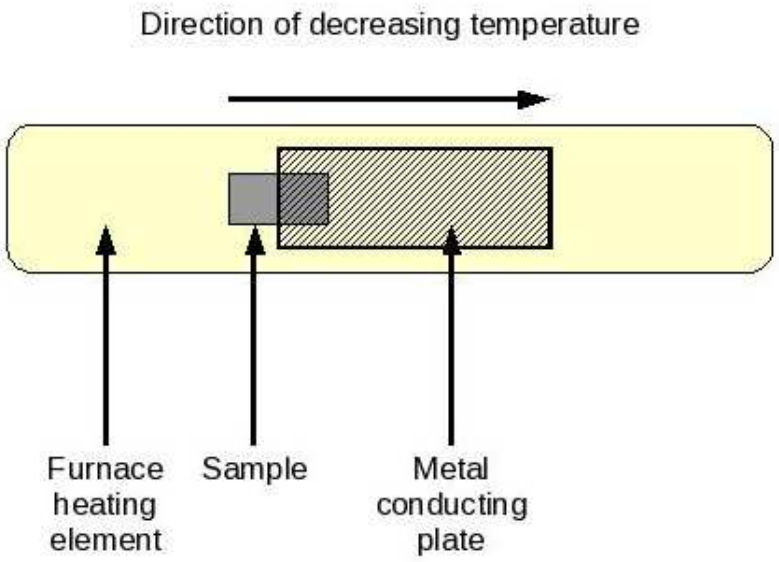

Figure 6.1: Schematic diagram depicting the procedure for establishing an MR gradient in a CoFe/Cu multilayer. The conducting metal plate acts as a heat sink, creating a temperature gradient across the sample. The higher temperature regions will be damaged more by the annealing and will have a lower MR, so the MR decreases in magnitude across the sample when moving away from the heat sink.

6.2 Four-point probe measurement of magnetoresistance

The MR of the annealed multilayer was measured in a 12 kOe external magnetic field using the procedure outlined in section 3.2.1 for performing electrical four-point probe measurements. Figure 6.2 shows the MR curve for the annealed multilayer alongside

the MR curve for an as-deposited multilayer for comparison. The MR of the annealed sample is $(-11.6 \pm 0.1)\%$, which is a significant reduction from the $(-28.3 \pm 0.1)\%$ of the as-deposited multilayer, demonstrating that the annealing does significantly damage the sample and lower its MR. The experiment was repeated in the maximum external magnetic field attainable using the equipment at SOLEIL of 900 Oe, well below the multilayer's saturation field of approximately 7 kOe, Figure 6.3 shows that in this low-field regime the annealed multilayer has an MR of $(-4.8 \pm 0.2)\%$, which is higher than the $(-3.3 \pm 0.2)\%$ measured for the as-deposited multilayer. This result suggests that in fields substantially lower than the saturation field the damage to the annealed multilayer causes the layers to switch more freely, contributing to a larger MR than seen in the as-deposited sample. There is no spatial resolution in this electrical measurement, so all local variations in MR are masked.

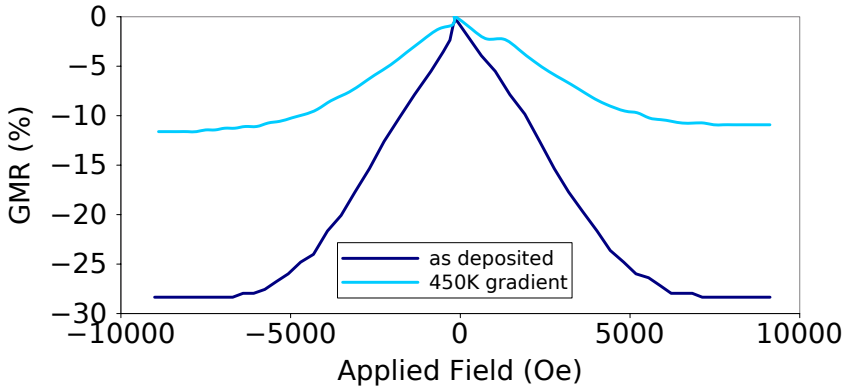

Figure 6.2: MR curves of the annealed multilayer annealed at 450 °C and an as-deposited multilayer taken at 12 kOe, beyond the saturation field of ∼7 kOe. The annealed multilayer has an MR of $(-11.6 \pm 0.1)\%$, less than half of the original as-deposited MR of $(-28.3 \pm 0.1)\%$.

6.3 Measuring a variation in the MRE across the sample using an IR camera

In order to obtain a spatially resolved image of the variations in MR across the sample, the MRE was measured in the emission geometry as outlined in section 3.3 using an IR camera. An IR camera image of the temperature of the sample is shown in figure 6.4, where the colour coded scale bar describes temperature in Kelvin. The higher of the two cool regions in the middle of the heater pad is a silver control sample, the lower cooler region is the annealed multilayer. There is a large variation in temperature at the edges of

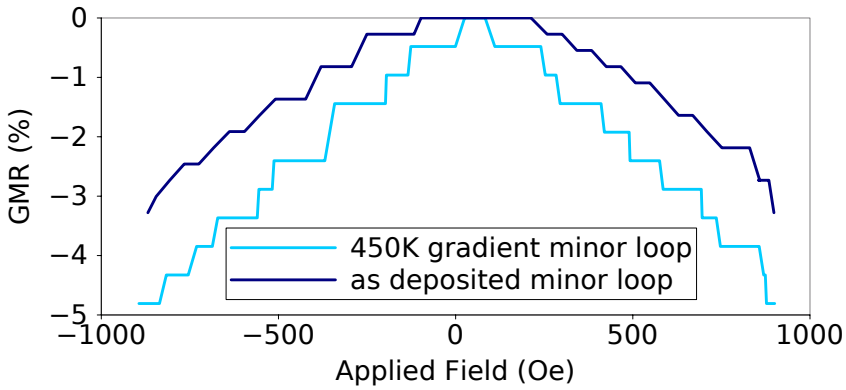

Figure 6.3: MR curves of the annealed multilayer and an as-deposited multilayer taken at 900 Oe, substantially below the saturation field of $\sim$7 kOe. In low fields, the annealed multilayer displays an MR of (-4.8 ± 0.2)%, greater than the (-3.3 ± 0.2)% MR of the as-deposited multilayer.

the sample where the emitted radiation is not normal to the sample plane therefore data near the edges of the samples is ignored when calculating the MRE.

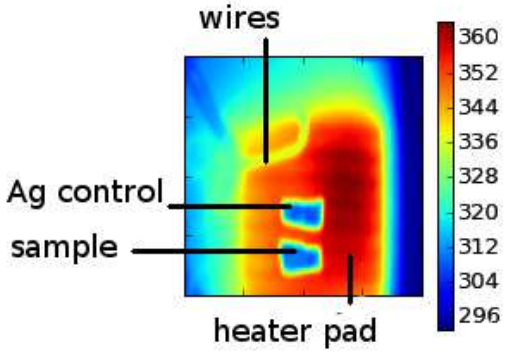

Figure 6.4: IR camera image showing temperature variations in the experiment, the sample is the lower of the two cool regions in the middle of the sample heater pad, the higher cool region is a silver control.

The IR camera image of the GMR of the annealed sample, obtained with an external magnetic field of 900 Oe, is shown in figure 6.5. The image is of a 3.0×2.4 mm area of the centre of the sample to avoid anomalous results associated with being near the edge of the sample. The colour scale bar denotes percentage change in GMR across the sample. The correlation factor, γ, is 11.9 if the maximum MRE observed from the sample corresponds to the maximum MR value measured from the electrical measurement. The MRE, and therefore MR, is clearly varying across the sample. The MRE decreases, in general, in the direction of increasing temperature and sample damage, in agreement with the earlier

prediction, demonstrating that an MR gradient can be established across a multilayer via the process proposed.

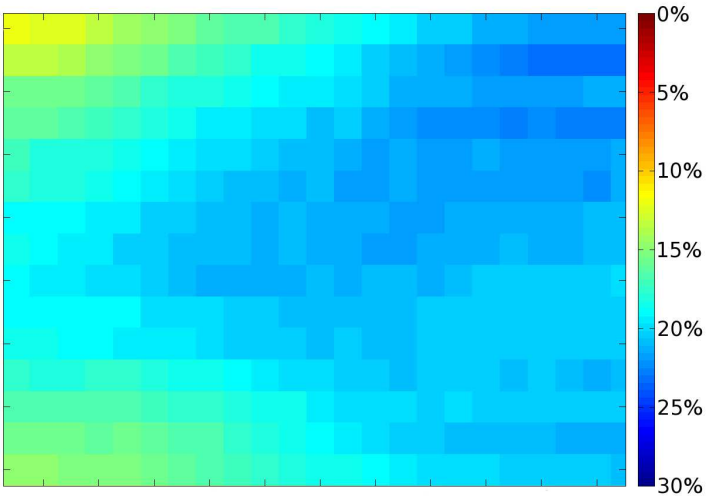

Figure 6.5: Spatially resolved MR measurement of the multilayer annealed at 450 °C taken with an IR camera in an external magnetic field of 900 Oe. The measurement is of a 3.0×2.4 mm area near the centre of the sample to avoid anomalous data being collected from near the edges of the sample. The MRE, and therefore MR, is decreasing across the sample in the direction of increasing temperature and sample damage. The reduction in MRE across the sample indicates a gradient in MR has been created across the sample.

6.4 Spatially and spectrally resolved MRE measurements

6.4.1 Comparison between MRE measurements in the reflection geometry between York and SOLEIL

MRE measurements on the as-deposited multilayer at 900 Oe and 12 kOe were performed in York as controls, shown in figure 6.6. An MRE measurement performed at SOLEIL on the as-deposited multilayer without the IR objective in place at 900 Oe was compared to the data from York. The MRE spectra show that with a 900 Oe external magnetic field the data obtained from York and SOLEIL are comparable, allowing for confident comparison of data obtained at the two institutions.

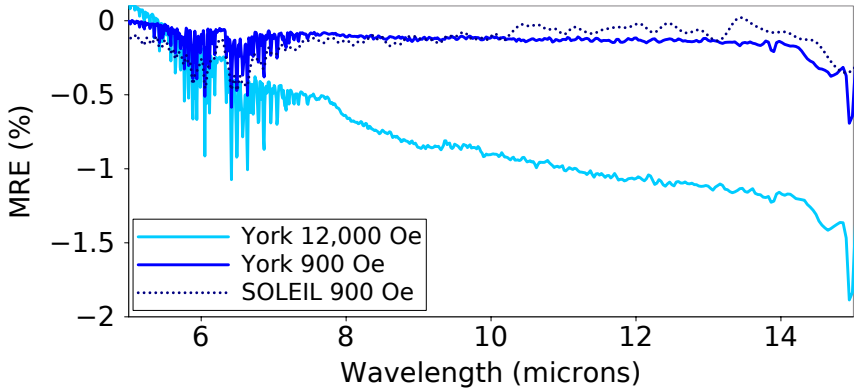

Figure 6.6: MRE spectra of the as-deposited multilater taken at both York and SOLEIL with an external magnetic field of 900 Oe. The data is comparable between the two institutions. An MRE spectra taken at 12 kOe is also shown for comparison.

6.4.2 Performing the first spatially and spectrally resolved MRE measurement

Three MRE spectra were collected from the annealed multilayer, along a line in the direction of increasing sample damage as depicted in figure 6.7. The points were separated by 1 mm, orders of magnitude greater than the 50 μm spot diameter, ensuring that each spectrum is sampled from a different part of the sample. Figure 6.8 shows the spectra from these three points. There is a clear and substantial variation in MRE, defined as the difference between the MRE at 4 μm and 15 μm, across the sample. The MRE increases markedly in the direction of increasing sample damage. This demonstrates conclusively that the low field GMR is increasing across the sample in the direction of increasing sample damage. The MR data in a low magnetic field shows that annealing causes a reduction in MR so this is in agreement with the MRE measurement. This result was the first MRE measurement to ever be performed with both spatial and spectral resolution.

6.5 Modelling the spatial and spectral variations in the MRE

The three MRE spectra from the annealed sample were simulated using the Jacquet-Valet model outlined in section 2.3. The model is valid for this material as the electron mean free path, $\lambda_{\mathrm{FM}} = 6\,\mathrm{nm}$, is several times longer than the CoFe layer thickness, $D = 1.5\,\mathrm{nm}$. This allows the average electron to travel through several layers of the material before

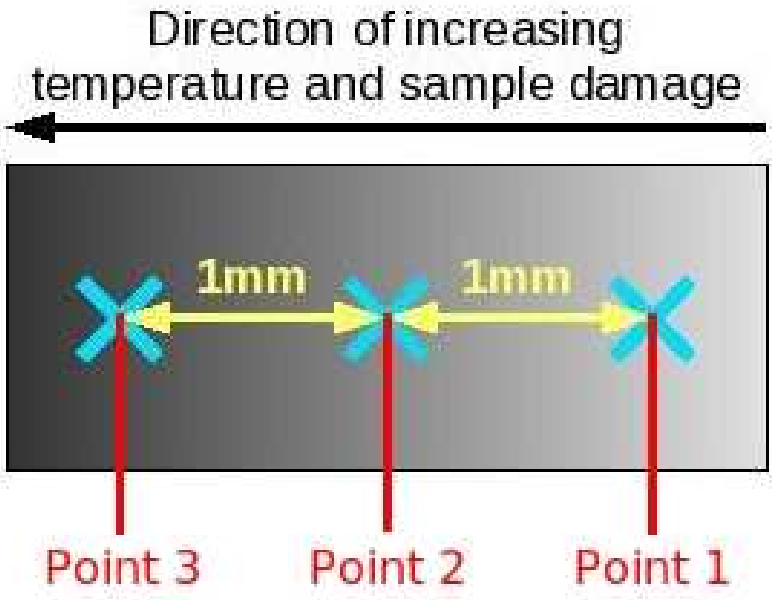

Figure 6.7: Schematic of where the spatially and spectrally resolved MRE measurements were performed. Three MRE spectra were taken in a line in the direction of increasing sample damage. The spacing between the points is an order of magnitude greater than the spot diameter of 100 μm, ensuring the spatial resolution.

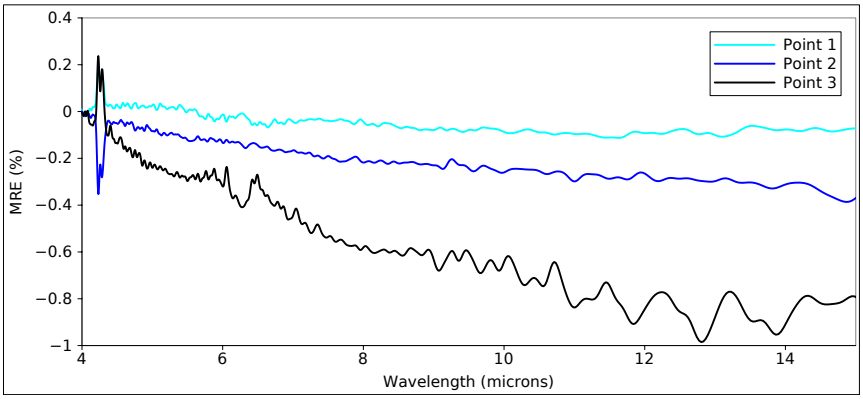

Figure 6.8: Low field MRE spectra for each of the three points on the sample. There is a clear decrease in MRE magnitude, defined as the difference between the MRE at 4 μm and 15 μm, across the sample.

experiencing a spin-selective scattering event, so the conductivities are within the SAL described in section 2.3 and the theory should hold. The material parameters used in the model are given in table 6.1. The values of τ_{FM}, the scattering time in the magnetic layers, and τ_{NM}, the scattering time in the non-magnetic layers, are calculated from experimentally obtained values of the mean free paths $\lambda_{\text{FM}} = 6\,\text{nm}$[77] and $\lambda_{\text{NM}} = 30\,\text{nm}$[78] respectively. c_{i}, the fraction of the sample at the interface, is estimated to be very small due to the high immiscibility of the Co, Fe and Cu[79]. m_1 is unity in fields greater than $\sim$7 kOe because the multilayer has reached saturation as can be seen in figure (6.2). m_1 is a fitting parameter in lower fields ($0 < m_1 < 1$).

Parameter	Description	Value
c_{FM}	Fraction of the multilayer which is ferromagnetic	0.55
c_{NM}	Fraction of the multilayer which is non-magnetic	0.43
c_{i}	Fraction of the multilayer which is an interface	fitting parameter
τ_{FM}	Relaxation time in ferromagnetic layers	$3.57 \times 10^{-15}\,\text{s}$
τ_{NM}	Relaxation time in non-magnetic layers	$1.78 \times 10^{-14}\,\text{s}$
τ_{i}	Relaxation time at FM/NM interfaces	fitting parameter
β	Bulk spin asymmetry coefficient	0.85[80]
γ	Interfacial spin asymmetry coefficient	0.75[81]
ε_∞	Static dielectric constant	3.5
ϕ	Angle of incidence of incident radiation	80°
N	Average conduction electron number density	$1.04 \times 10^{29}\,\text{m}^{-3}$
m_0	Fraction of m_s in 0 Oe	0
m_1	Fraction of m_s in 900 Oe	fitting parameter

Table 6.1: Model parameters for the Jacquet-Valet model of an annealed CoFe/Cu multilayer. The values of m_1, c_{i}, and τ_{i} are used as fitting parameters to try and simulate the shape of the experimental MRE spectra.

Three explanations for the origin of the variation in MR are explored with the model. Intermixing at the interface will cause a reduction in the MR as the interlayer exchange coupling is dependent on the separation distance between the magnetic layers. This possibility is explored by using c_{i} as a fitting parameter. It is also plausible that a small quantity of intermixing at the interface will cause a change in the interfacial scattering time, leading to variation in spin selective scattering and therefore MR across the sample. This possibility is explored by using τ_{i} as a fitting parameter. The third explanation is that the annealing has caused disruption to the magnetic ordering within each magnetic layer, causing an increase in layer reversal in low fields, creating the variation in MR observed. This possibility is explored by using m_1 as a fitting parameter.

6.5.1 Modelling the variation in MR as a variation in interfacial thickness

τ_{i}, the interfacial scattering time, is estimated to be $\tau_{\mathrm{i}} = 1 \times 10^{-14}$ s, a typical value for a metal. The value of m_1 was estimated from the electrical MR curve in figure 6.2. At 900 Oe, the MR is 41% of its saturation value, so $m_1 = 0.41$. The antiferromagnetic exchange coupling between layers is sensitive to the layer separation, so a change in interfacial thickness should weaken the exchange coupling leading to increased switching in a low field. Simulated spectra with c_{i} varied between zero (no interfaces) and one (complete intermixing) are given in figure 6.9. The spin asymmetry at the interface, γ, is assumed to have not changed. Increasing c_{i} causes the spectral minimum to shift towards the near-IR, whilst the MRE magnitude, the difference between the MRE at 4 μm and the location of the spectral minimum, is almost constant. Neither of these traits are consistent with the trends observed experimentally, so the variation is not a result of increased intermixing at the interface.

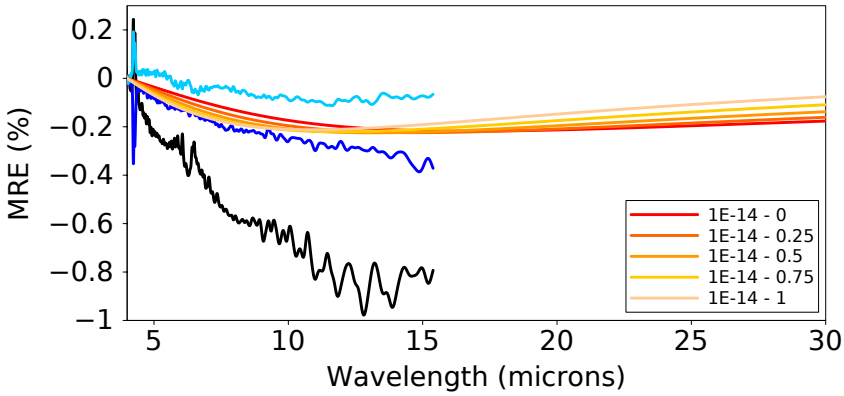

Figure 6.9: Simulated MRE spectra where c_{i} has been varied between 0 and 1 and $\tau_{\mathrm{i}} = 1 \times 10^{-14}$ s. The simulated spectra do not show the significant variation in MRE magnitude of the experimental spectra, whilst there is a shift to the near-IR of the spectral minimum that is not present in the experimental spectra.

6.5.2 Modelling the variation in MR as a variation in interfacial scattering time

The value of τ_{i} was varied across a range of reasonable scattering times for a metal, 1×10^{-13} s and 1×10^{-17} s, while c_{i} and m_1 were kept constant. The previous modelling demonstrated that there was no appreciable difference to the MRE spectra due to varying

c_i, so a degree of intermixing was allowed, setting $c_\mathrm{i} = 0.25$. The simulated spectra with varying τ_i are shown in figure 6.10. The shape of the spectra varies significantly with τ_i, the spectral minimum moving towards the near-IR as τ_i is made shorter. This does not agree with the experimental spectra, where the spectral minima appear to be at or just beyond 15 μm.

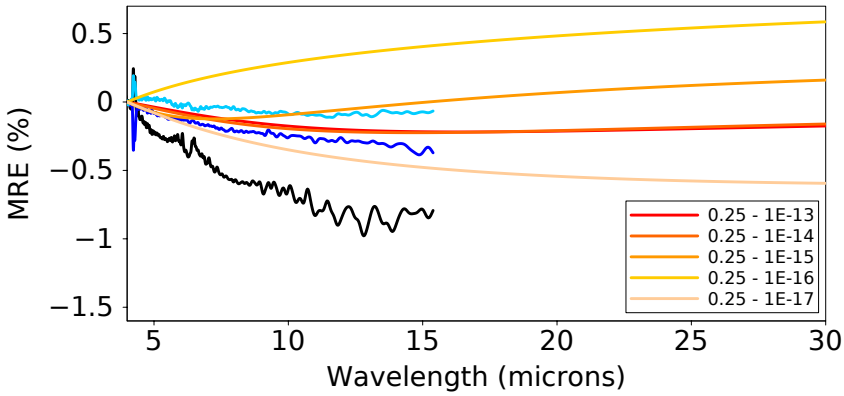

Figure 6.10: Simulated MRE spectra where the τ_i has been varied and $c_\mathrm{i} = 0.25$. The spectral minimum of the simulated spectra moves towards the near-IR as τ_i is shortened. This does not agree with the experimental spectra, where the minima are at or beyond 15 μm.

6.5.3 Modelling the variation in MR as a variation in layer switching in a 900 Oe magnetic field

The previous two attempts at modelling the MRE involved varying the ratio $c_\mathrm{i}/\tau_\mathrm{i}$ in order to change the value of β_SAL and therefore the MRE. Instead, the variation in the MR was assumed to be due to variations in the amount of layer switching occurring across the sample. Where the sample has experienced greater damage the magnetically active layers become disorded, causing layers to reverse magnetisation in lower fields. In areas of the sample with significant damage, a high MR in a lower field is expected as more layer switching has occurred. This translates into the model as a variation in m_1, the fraction of m_s in a given field. Figure 6.11 shows the result of using m_1 as a fitting parameter. The simulated spectra are in excellent agreement with the experimental spectra with m_1 as a fitting parameter. The simulated spectra have spectral minima outside the bolometer's detection range. However, these minima have been observed in previous work by Mennicke *et al.*[82], supporting the argument that the variation in MR is due to changes in the degree of layer switching across the sample. Simulated spectra using m_1 as a fitting

parameter are shown in figure 6.11, showing that the experimental MRE spectra can be well reproduced by assuming there is a variation in the amount of layer switching across the multilayer. The value of m_1 required to reproduce the spectra at points 1, 2 and 3 was $m_1 = 0.25$, 0.5 and 0.8 respectively. A simulation where $m_1 = 1$ (ideal) is also shown for comparison. As variations in τ_i and c_i are unable to explain the variation in MR, it can be stated with confidence that the variation in MR is due to a variation in m_1, the degree of layer switching due to disorder within the magnetic layers in a given field.

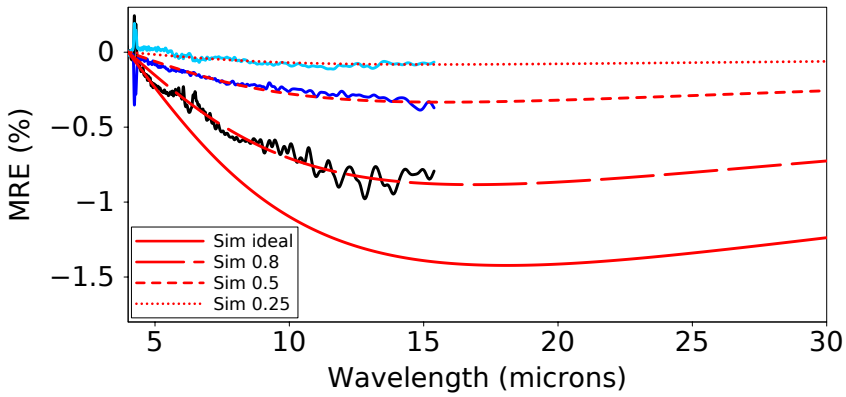

Figure 6.11: Simulated MRE spectra with m_1 as a fitting parameter. The simulated spectra fit well to the experimental spectra, strongly indicating that increased layer switching due to disorder in the magnetic layers in damaged parts of the sample is causing local increases in MR.

6.6 Conclusions

A spatial MR gradient across a CoFe/Cu multilayer was established by attaching a heat sink to one end of the multilayer and heating it in a furnace. Electrical four-point probe measurements of the MR of the multilayer, as well as an as-deposited multilayer, demonstrated that the annealing causes a substantial drop in MR at 12 kOe. At 900 Oe, the maximum achievable field in the MRE experiments, the annealed multilayer displayed a greater MR than the as-deposited multilayer. This was shown through modelling of the MRE spectra of the annealed multilayer to be due to increased layer switching in a 900 Oe field, due to damage to the magnetically active layers caused by heating the sample. The alternative proposals, that the reduction in MR was due to variations in intermixing at the interface or a change in the interfacial scattering time, were found to be incorrect through MRE modelling. Simulated MRE spectra with varying interfacial parameters were unable to reproduce the shape of the experimental MRE spectra. Changing the thickness of the

interface had very little effect on the spectral shape and varying the interfacial scattering time caused a shift of the spectral minimum towards the near-IR, which is not physical. The electrical MR measurements are not spatially resolved as they average over a large area of the sample. Spatial resolution was achieved using an IR microscope and scanning stage, clearly showing a variation in MRE of $\sim$0.7% and therefore a variation in MR across the sample. This was the first time both spatial resolution and the spectral resolution necessary to model the system were obtained simultaneously in a single MRE measurement, establishing the MRE as a powerful remote sensing technique for probing MR.

Chapter 7

Utilising Far Infrared Synchrotron Radiation to Correlate the MRE With the MR of Spin Valves

In chapter 6 it was demonstrated that the MRE can be used as a method of remotely probing the MR of a material. However, no attempt was made to make a quantitative connection between the magnitude of the MRE and the magnitude of the MR. There has been some successful effort in making this connection in the mid-IR, although these correlations are complicated phenomenological formulae consisting of several fitting parameters. Previous theoretical work has outlined a correlation between the MRE and the MR, with the correlation predicted to be simpler in the far-IR. Using far-IR radiation from the SOLEIL synchrotron, the correlation was examined experimentally for the first time using a series of spin valves with different MR values. It was also possible to gain insight into the magnetic properties of the spin valves by modelling the MRE spectra.

7.1 Spin valve structure and composition as well as its link to the MR

7.1.1 Structure and composition of the spin valves

The spin valves used in this experiment were grown by HGST and have the structure shown in table 7.1. They have a typical spin valve structure; a CoFeGe ferromagnetic layer pinned to an IrMn layer separated from a free CoFeGe ferromagnetic layer by a non-magnetic metallic copper spacer. Figure 7.1 shows a schematic of this structure. Five

Ta	4.0nm	
Ru	2.0nm	Capping layer
Cu	1.0nm	
$(CoFe)_{1-x}Ge_x$	6.0nm	Free ferromagnetic layer
Cu	3.5nm	Non magnetic spacer layer
$(CoFe)_{1-x}Ge_x$	3.0nm	Pinned ferromagnetic layer
CoFe	2.0nm	Pinned ferromagnetic layer
IrMn	6.0nm	Antiferromagnetic pinning layer
Ru	2.0nm	Orientation layer
Ta	3.0nm	Seed layer
Glass		Substrate

Table 7.1: The general structure and composition of the HGST spin valves.

A11	$x = 0\%$
A12	$x = 5\%$
A13	$x = 10\%$
A14	$x = 20\%$
A15	$x = 30\%$

Table 7.2: Germanium content of the five spin valve samples.

spin valve samples were produced with different concentrations of germanium in the magnetically active layers. The germanium causes an increase in the resistance of the layer, causing a decrease in the spin diffusion length in the magnetically active layers[83], reducing the CIP MR and enhancing the CPP MR. The germanium concentrations of the five samples, A11-A15, with percentage germanium concentrations ranging from 0% to 30%, are shown in table 7.2.

7.1.2 MR of the spin valve samples

These spin valves were chosen for this experiment because they are known to have different values of MR whilst retaining a very similar structure. The plot of MR against germanium concentration in figure 7.2 shows that there is a very rapid drop off of the CIP MR with increasing germanium concentration, caused by the increase in resistance as the spin diffusion length decreases.

Figure 7.3 shows the in plane MH loop for spin valve A11 near the switching point of the free magnetic layer. It takes a relatively modest field of $\sim$150 Oe to fully reverse

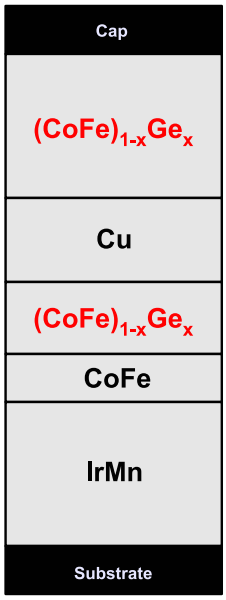

Figure 7.1: Structure of the spin valve samples, with layer thickness approximately to scale.

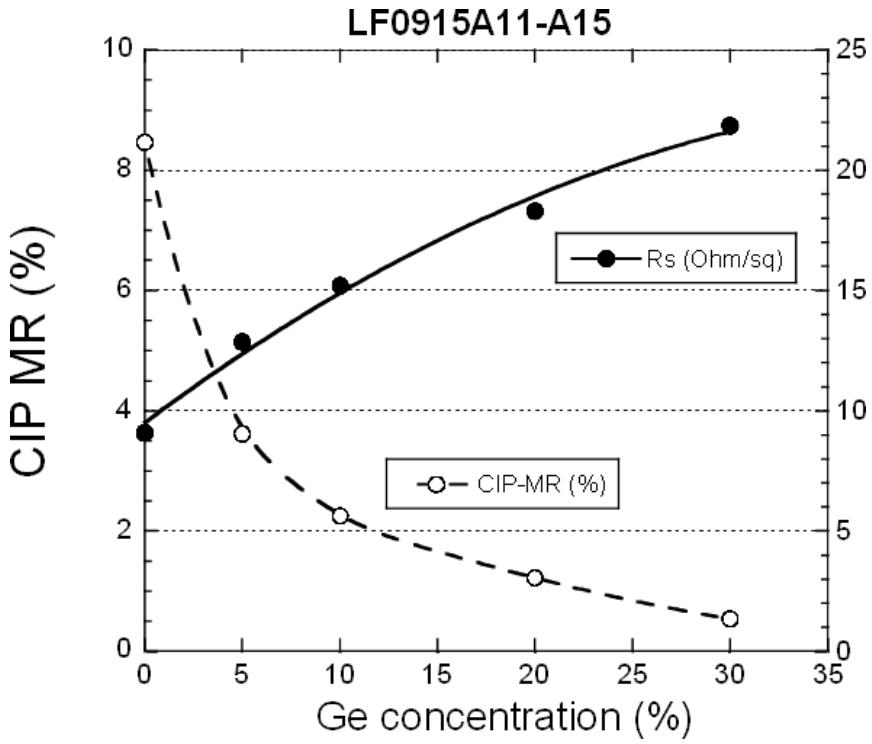

Figure 7.2: CIP MR for the spin valve samples decreases as a function of germanium concentration in the magnetically active CoFe layers. Data and image courtesy of HGST.

the free layer, well below the 900 Oe maximum of the electromagnet. This is beneficial as there will be good reproducibility between repeat measurements as there will be no variation in layer saturation between the measurements. The smaller, flatter curve is the out of plane MH loop, which is not relevant here. Figure 7.4 shows the complete exchange biased MR curve for sample A11. A large change in resistance, and therefore a large change in MR, occurs when the free layer switches. For the MRE to be sensitive to this change in resistance, a reflection spectrum must be taken at a magnetic field value either side of the switch. For these experiments, these field values were -500 Oe and 300 Oe. The magnetic field was swept between the maximum achievable field of ± 900 Oe so that the measurement has good reproducibility, minimising hysteretic effects.

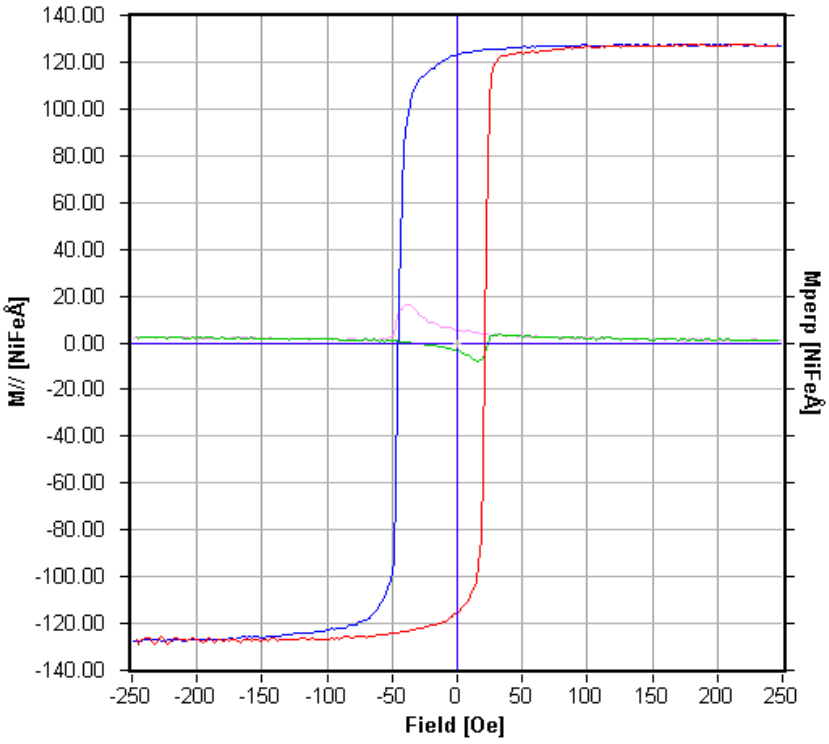

Figure 7.3: In plane MH curve for spin valve A11, showing the magnetisation of the free CoFeGe layer saturating in $\sim$150 Oe. The smaller, flatter curve is the out of plane MH loop, which is not needed in this analysis. Data and image courtesy of HGST.

7.2 MRE spectra of spin valves in the far-IR

MRE spectra were collected from each of the spin valve samples using the techniques outlined in section 3.3. A mid-IR MRE spectrum was obtained for each spin valve using

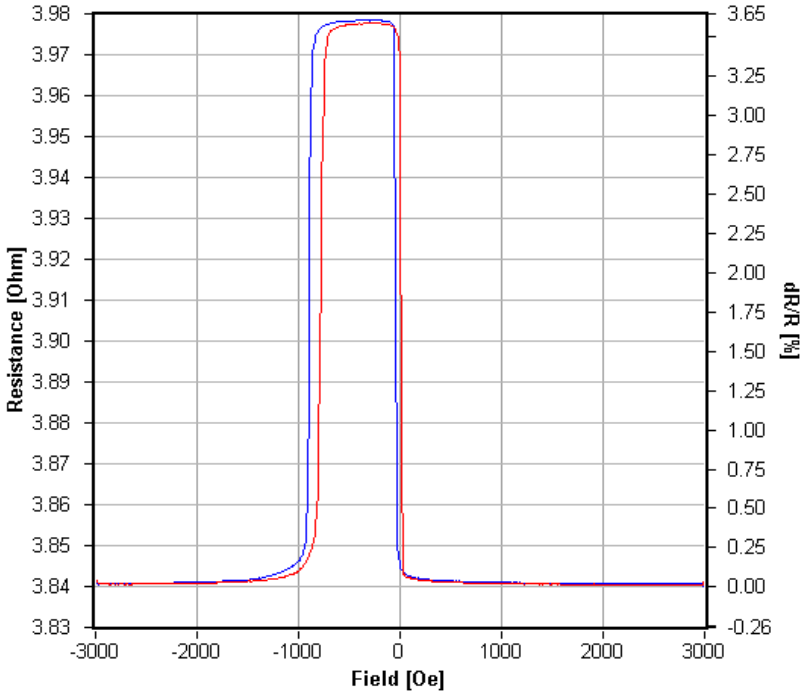

Figure 7.4: Exchange biased MR curve for spin valve A11. The maximum resistance change is either side of the switch of the free layer. Data and image courtesy of HGST.

an MCT detector sensitive in the range $\sim 1.5 - 20.0$ μm (in York) whilst a far-IR spectrum was obtained for each sample using a bolometer sensitive in the range $\sim 14.5 - 50.0$ μm (at SOLEIL). Figure 7.5 shows the MRE spectra for the five spin valves. The magnitude of the MRE, the difference between the highest and lowest MRE values for each spectrum, decreases with increasing germanium concentration. The spin valves with the higher CIP MR also have the largest MRE, so the trend of the MRE spectra agrees with the trend of the electrical MR results. The black vertical line at 14.5 μm is the boundary between the mid-IR and the far-IR. Although the detection ranges of the two detectors overlap, the data is statistically insignificant towards the edges of the range for both detectors. At 14.5 μm the data from both detectors is still good, so the spectra are combined at this wavelength. Data from the bolometer is discarded below 14.5 μm as is data from above 14.5 μm from the MCT detector. The MCT and bolometer data match up well at the boundary, suggesting that there was no drift and that the far-IR data is accurate. This experiment is the first to demonstrate the MRE this far in to the far-IR and reconcile that data with data from the near-IR.

Figure 7.6 shows the magnitude of the MR plotted against the magnitude of the MRE.

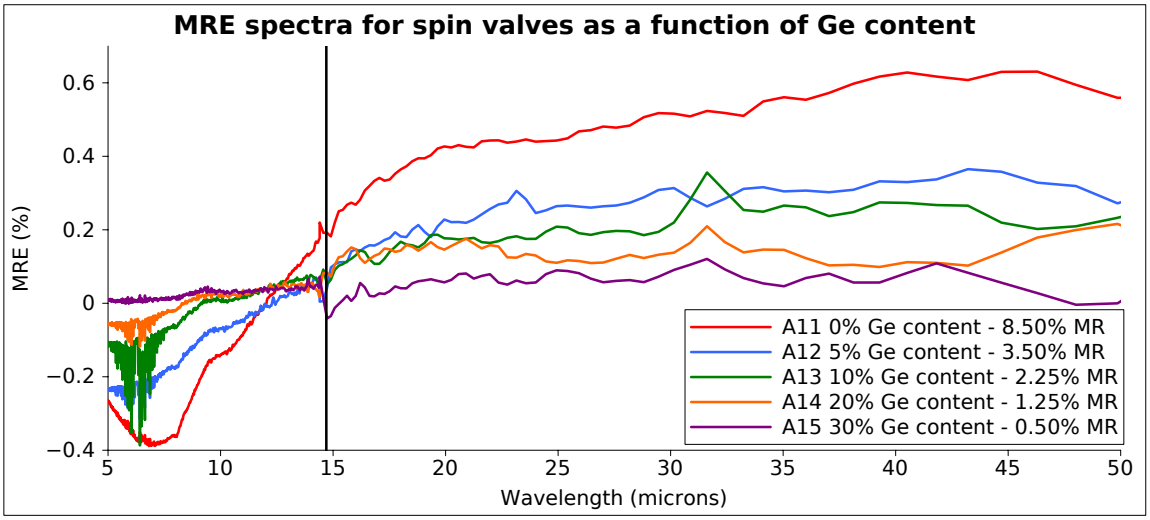

Figure 7.5: The Ge content of the spin valve decreases the spin diffusion length, leading to a much reduced CIP MR, which is observable here as a reduction in the absolute magnitude of the MRE. The far-IR MRE, to the right of the black vertical line, is presented experimentally for the first time and agrees with the near-IR data where the MCT and bolometer detection ranges overlap.

The trend is roughly linear so it should be expected that any correlation between the MR and MRE should be linear in form.

7.3 Modelling the MRE in the far-IR using the Jacquet-Valet model

The MRE spectra were modelled in a similar way to the CoFe/Cu multilayers discussed in the previous chapter. The parameters used for the spin valves are shown in table 7.3 below. The aim here is to model the reduction in the MR between the different samples due to the germanium doping and two models are proposed. Firstly, as the resistance increases due to the increasing germanium concentration, the scattering time in the ferromagnetic layer could be shortened. Reducing the scattering time means an increase in the number of spin-independent scattering events, causing a decrease in spin polarisation; leading to a reduction in MR in a CIP geometry. The effect is much less in the CPP case as the average electron experiences many layers and the spin polarisation and MR are not dominated by the effects in a single layer. The parameter that controls the scattering time in the CoFeGe is τ_{FM}, so this is used as the fitting parameter. The second proposal is that the addition of germanium dopant atoms decreases the spin diffusion length in

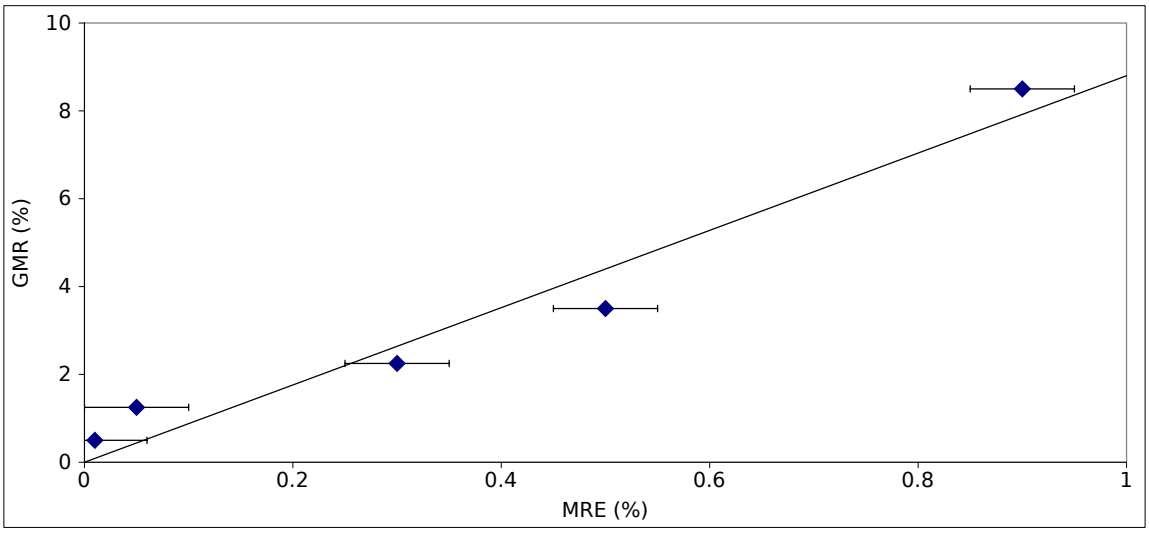

Figure 7.6: The magnitude of the MRE of the spin valves increases linearly with MR, implying that the correlation between the MR and MRE should be linear in form.

the ferromagnetic layers, causing an increase in the amount of interfacial scattering as it is now more likely that electrons will scatter to the interface from the ferromagnetic layers, leading to a reduction in spin polarisation at the interface. This will reduce the CIP MR as electrons passing near interfaces will experience increased spin-independent scattering and therefore the MR will be reduced. This effect is even more prominent in the CPP geometry as the average electron will cross many interfaces and will experience proportionally more spin-independent scattering events; reducing the MR. The value of γ, the interfacial spin asymmetry coefficient, is used as a fitting parameter in order to fit the reduction of MR. Reducing γ should reduce the MR as the model predicts MR $\propto \beta_{\mathrm{SAL}}^2$ and $\beta_{\mathrm{SAL}} \propto \gamma$. Varying γ is in essence the same as varying the ratio $c_{\mathrm{i}}/\tau_{\mathrm{i}}$ in order to change the value of β_{SAL} like in the previous chapter. It is worth noting here that the model used only calculates the CIP GMR. Experimental evidence suggests that there is actually an increase in CPP MR with the addition of germanium which this model does not account for.

Figure 7.7 shows the simulated MRE spectra for the spin valves using τ_{FM} as a fitting parameter. As τ_{FM} decreases, the magnitude of the MRE increases. This suggests that the shortening of the scattering time is increasing the MR, which does not agree with the experimental observation, so this interpretation must be incorrect. Figure 7.8 shows the simulated MRE spectra for the spin valves using γ as a fitting parameter. The magnitude of the MRE of the simulated spectra (the difference between the maximum and minimum value of the MRE) reduces very quickly as γ decreases, as the magnitude of the experimental MRE spectra drops with MR. The simulated spectra also fit closely to their

Parameter	Description	Value
c_{FM}	Fraction of the spin valve which is ferromagnetic	0.65
c_{NM}	Fraction of the spin valve which is non-magnetic	0.32
c_{i}	Fraction of the spin valve which is an interface	0.03
τ_{FM}	Relaxation time in ferromagnetic layers	sample dependent
τ_{NM}	Relaxation time in non-magnetic layers	1.49×10^{-14} s
τ_{i}	Relaxation time at FM/NM interfaces	3×10^{-17} s
β	Bulk spin asymmetry coefficient	0.71 [83]
γ	Interfacial spin asymmetry coefficient	fitting parameter
ε_∞	Static dielectric constant	3.5
ϕ	Angle of incidence of incident radiation	80 °
N_{FM}	Average conduction electron number density	sample dependent
N_{NM}	Average conduction electron number density	3.77×10^{29} m^{-3}
m_0	Fraction of m_s in 0 Oe	0
m_1	Fraction of m_s in 900 Oe	1

Table 7.3: Model parameters for the spin valve samples. To attempt to model the variation in MR with germanium concentration, the interfacial spin asymmetry coefficient, γ, and the scattering time in the ferromagnet, τ_{FM}, were used as fitting parameters in independent models. The value of N_{FM} was calculated by taking the value of N for CoFe and germanium and taking an average N weighted by how much germanium was present. This was then used to calculate τ_{FM} for each sample. Values of c were calculated from the relative thicknesses of the layers and values of N were calculated from the molar mass, density and valency of each atom. $m_0 = 0$ and $m_1 = 1$ as the spin valve goes from antiparallel to parallel alignment, a full switch of magnetisation in 900 Oe.

experimental analogues, as demonstrated in figures 7.9 through 7.13, indicating that the choice of fitting parameter was sound.

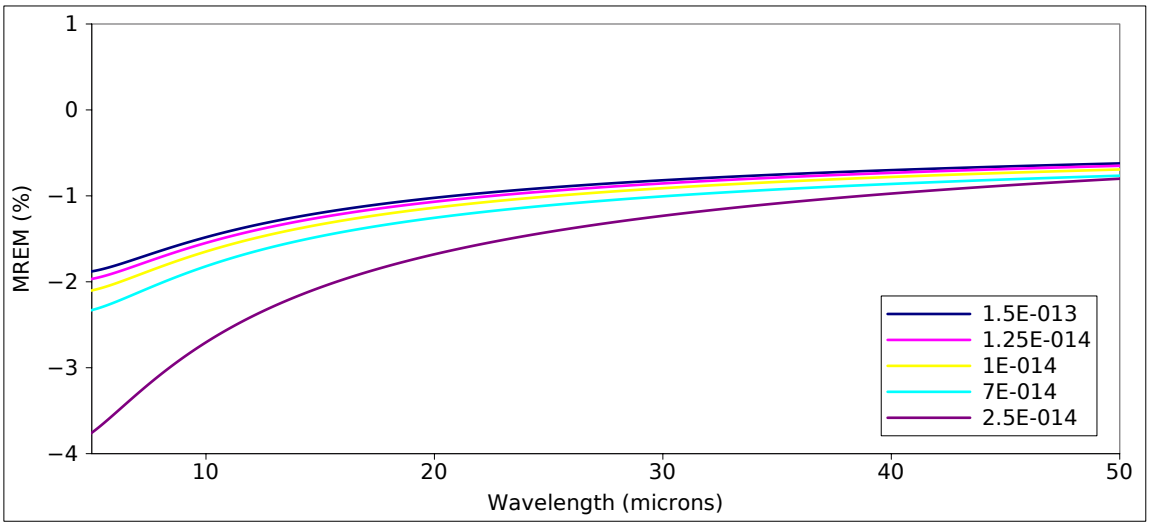

Figure 7.7: Simulated MRE spectra for the spin valves with τ_{FM} as a fitting parameter. The shortening of the scattering time in the ferromagnet leads to an increase in the MR rather than a decrease, suggesting this interpretation is incorrect.

7.4 Investigating the correlation between the MRE and the MR of the spin valves

7.4.1 Relating the simulated MR to the experimental MR

It was stated in the previous section that MR $\propto \beta^2_{\mathrm{SAL}}$. The MR was plotted against β^2_{SAL}, shown in figure 7.14 to determine if this relationship is true and to determine the proportionality constant if so. The figure shows that the relationship between the MR and β^2_{SAL} is indeed linear with a constant of proportionality of 2.7.

7.4.2 Relating the MR to the MRE in the mid-IR

Previous theoretical work by Dr. Ralph Mennicke[84] had shown that the MR is related to the spectral minimum of the MRE, λ_{min}, the magnitude of the MRE at the spectral minimum, $\mathrm{MRE}_{\mathrm{min}}$ and the conduction electron number density N. Equation 7.1 shows this phenomenological correlation between the MR and the MRE, where C, α and η are fitting parameters.

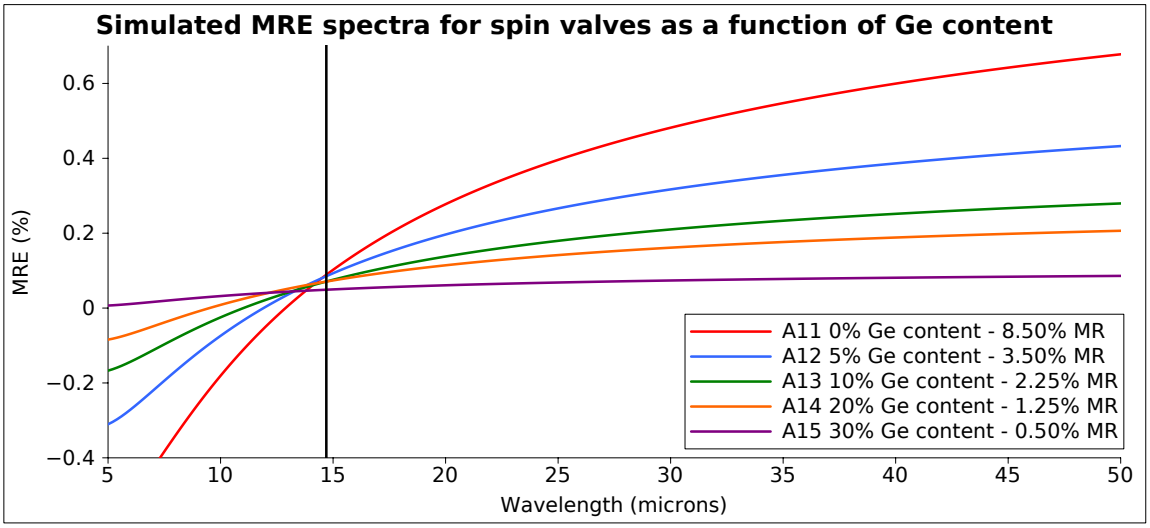

Figure 7.8: Simulated MRE spectra for the spin valves with γ as a fitting parameter. The rapid drop off in MRE due to the lowering of γ is consistent with that found experimentally where the drop off in MR was caused by an increase in germanium contaminant concentration.

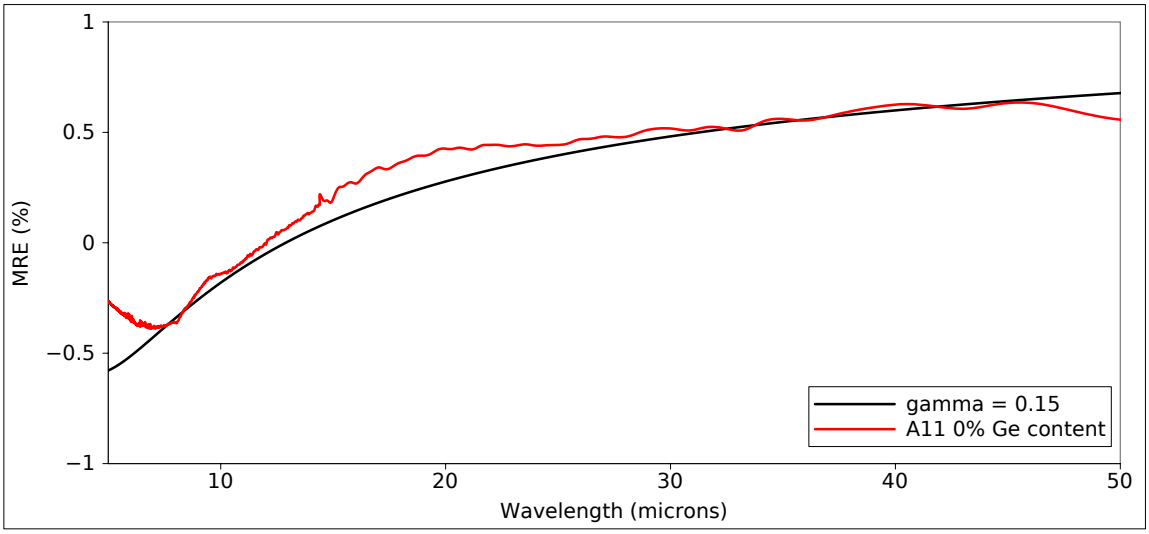

Figure 7.9: Simulated and experimental MRE spectra for spin valve A11 - 0% Ge content.

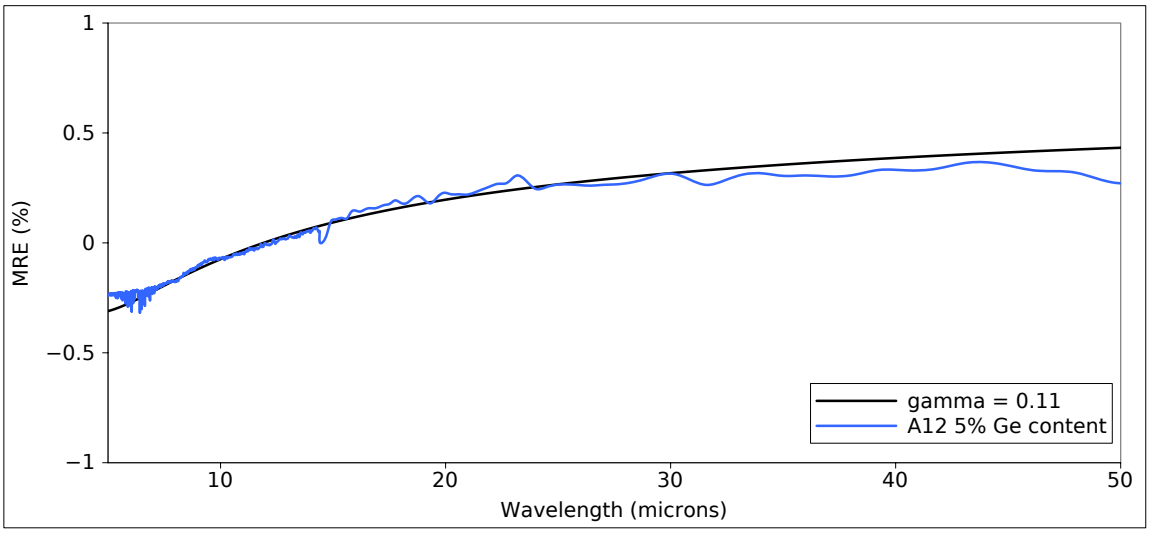

Figure 7.10: Simulated and experimental MRE spectra for spin valve A12 - 5% Ge content.

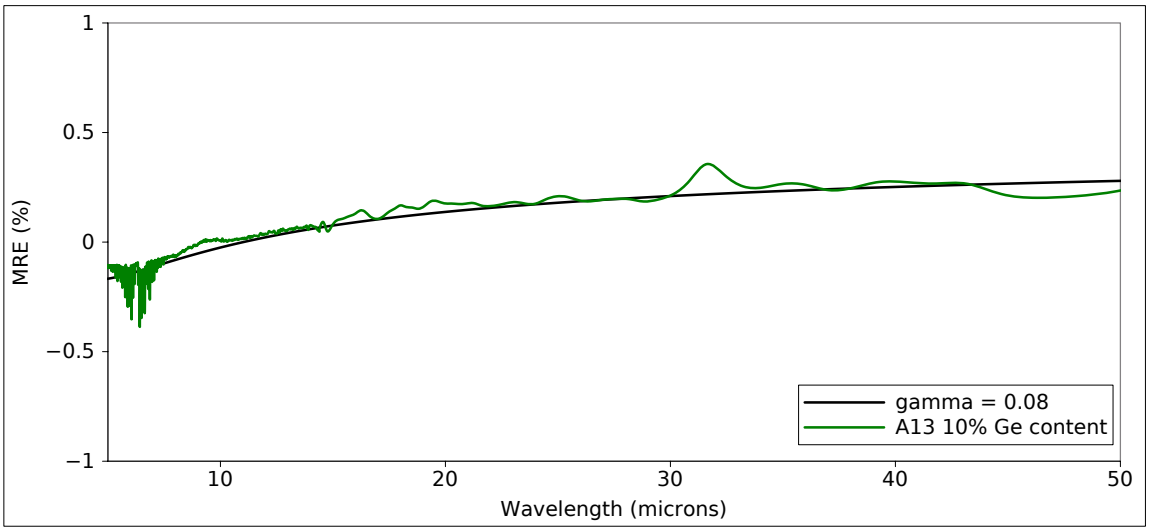

Figure 7.11: Simulated and experimental MRE spectra for spin valve A13 - 10% Ge content.

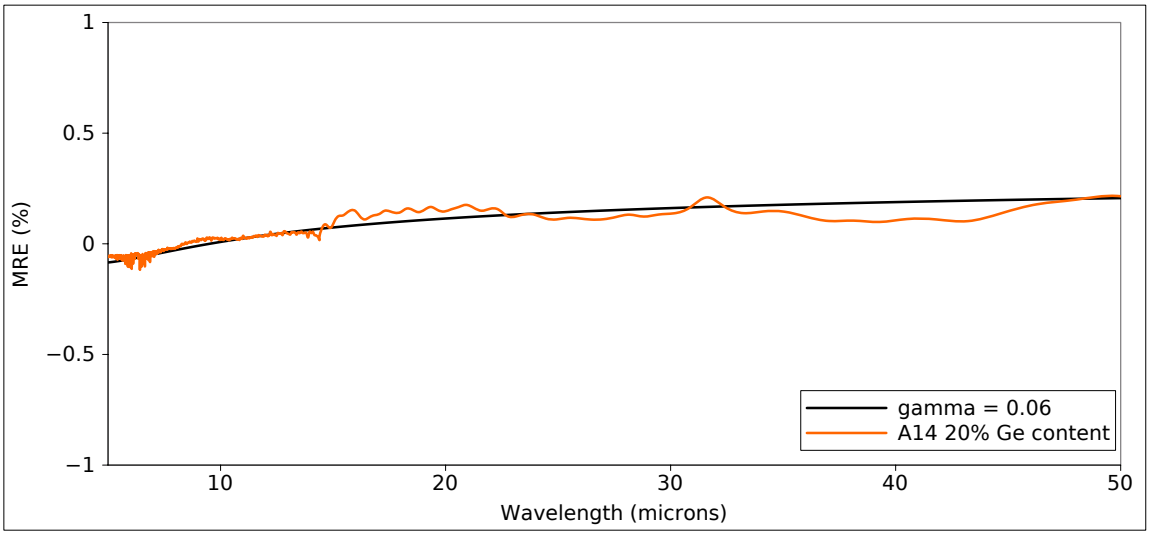

Figure 7.12: Simulated and experimental MRE spectra for spin valve A14 - 20% Ge content.

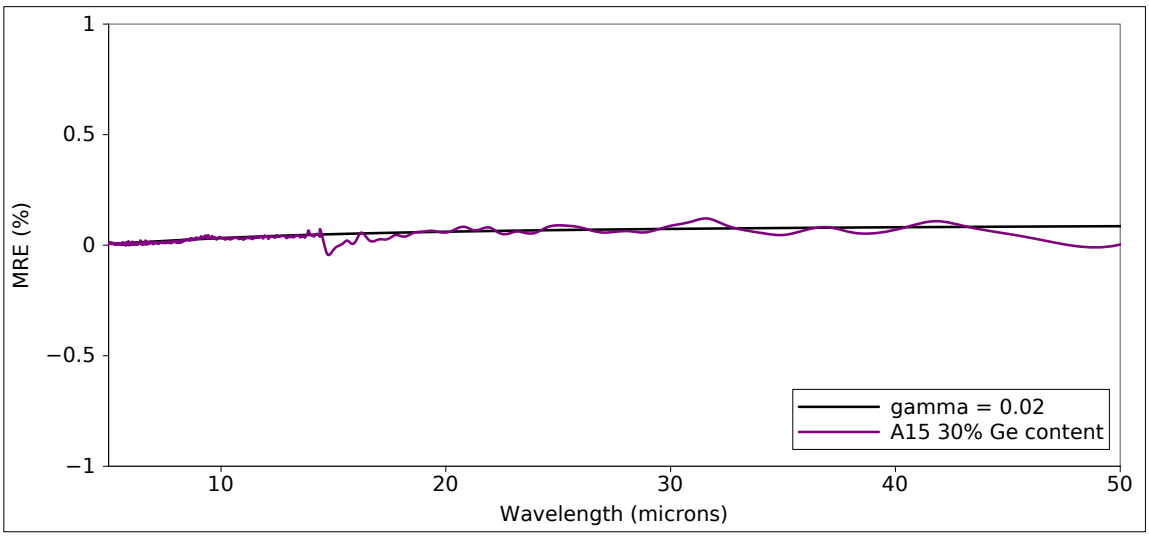

Figure 7.13: Simulated and experimental MRE spectra for spin valve A15 - 30% Ge content.

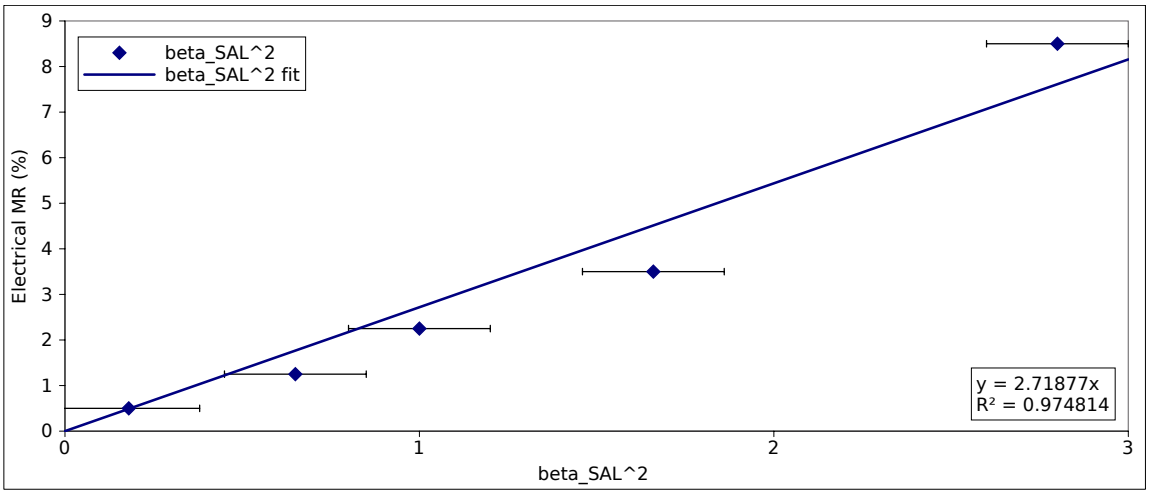

Figure 7.14: Plot of electrical MR against β^2_{SAL} for each of the spin valve samples. There is a linear relationship between the MR and β^2_{SAL}, demonstrating that the prediction that MR $\propto \beta^2_{\text{SAL}}$ holds.

$$\text{MR}\,(\%) = C \cdot N^{\alpha} \cdot [\lambda_{\text{min}} \cdot \text{MRE}_{\text{min}}\,(\%)]^{\eta} \tag{7.1}$$

Using the fitting parameters from Dr. Mennicke's thesis[84], $C = 1.46$, $\alpha = 0.45$ and $\eta = 0.93$, an estimate for the MR was obtained for each of the spin valve samples. The electrical MR was plotted against the MR estimated from the MRE, shown in figure 7.15, using equation 7.1. The correlation, which is meant to be linear in form, does not hold with error for four of the five spin valves; giving the relation $\text{MR}\% = 3.6 \times \text{MRE}\%$. The correlation formula is a complex phenomenological function of the spectral features, with several fitting parameters. It is based on difficult to measure parameters of the spectra, such as the location of the spectral minimum, leading to a large degree of inaccuracy. In order to correlate the MR to the MRE well, a new approach is necessary.

7.4.3 Relating the MR to the MRE in the far-IR

Previous theoretical work by Mennicke *et al*[84], shown in figure 7.16, has shown that in the far-IR the correlation between the MR and MRE is much simpler, depending only on material constants and $\omega^{-0.5}$:

$$\text{MR}(\%) \approx \frac{\text{MRE}(\%)}{\sqrt{2\epsilon_0\rho_0\omega}} \tag{7.2}$$

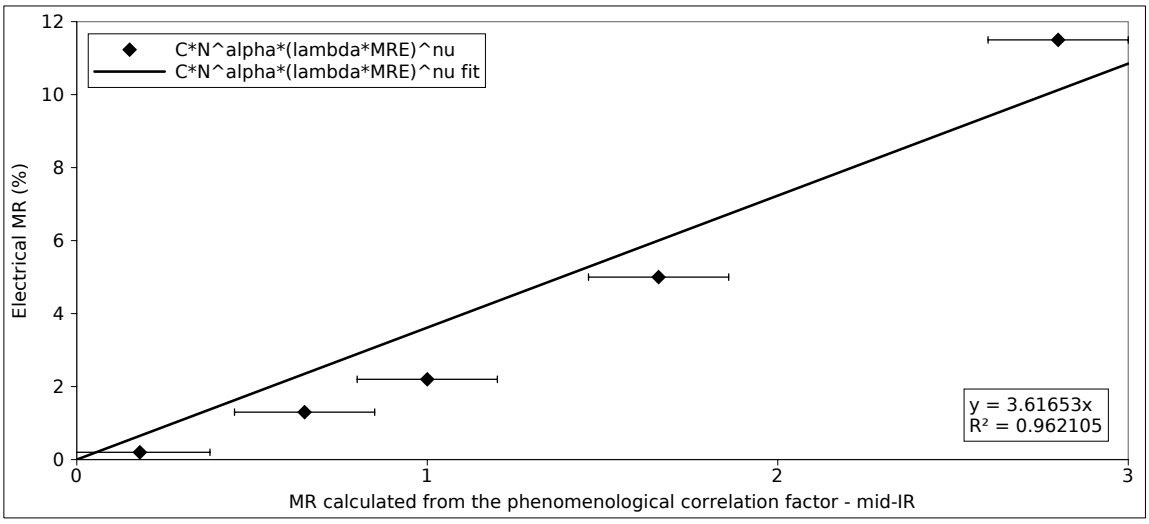

Figure 7.15: Plot of electrical MR against MR estimated from the MRE in the mid-IR. The correlation between the MR and the MRE is poor in the mid-IR due to the large uncertainties in the correlation formula.

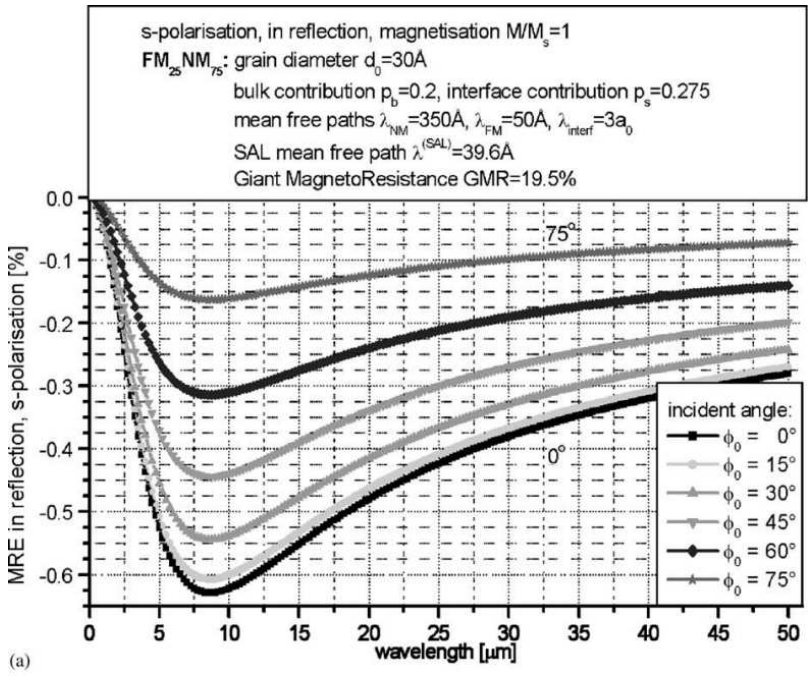

Figure 7.16: Previous theoretical work showing the MRE out into the far-IR. The spectra flattens out as $\omega^{0.5}$, allowing for a much simpler correlation[84].

This correlation is much simpler and contains no fitting parameters, in principle giving a direct correspondence between the electrical MR measurement and the MRE in the far-IR. The MRE was measured at 27.5 μm where there is not much noise in the far-IR spectra and the spectral shape is clearly has a $\sqrt{\omega}$ dependence. The plot of MR against the values calculated from this correlation factor are given in figure 7.17. The correlation between the MR and the MRE is strongly linear, with a correlation factor of 0.64. This shows an almost direct correspondence of the MR to the MRE, experimentally confirming the theoretical prediction that the MR and MRE correlate strongly in the far-IR for the first time. However, the correlation factor is supposed to be unity, so there is an additional unexpected correlation factor, the origin of which is unclear.

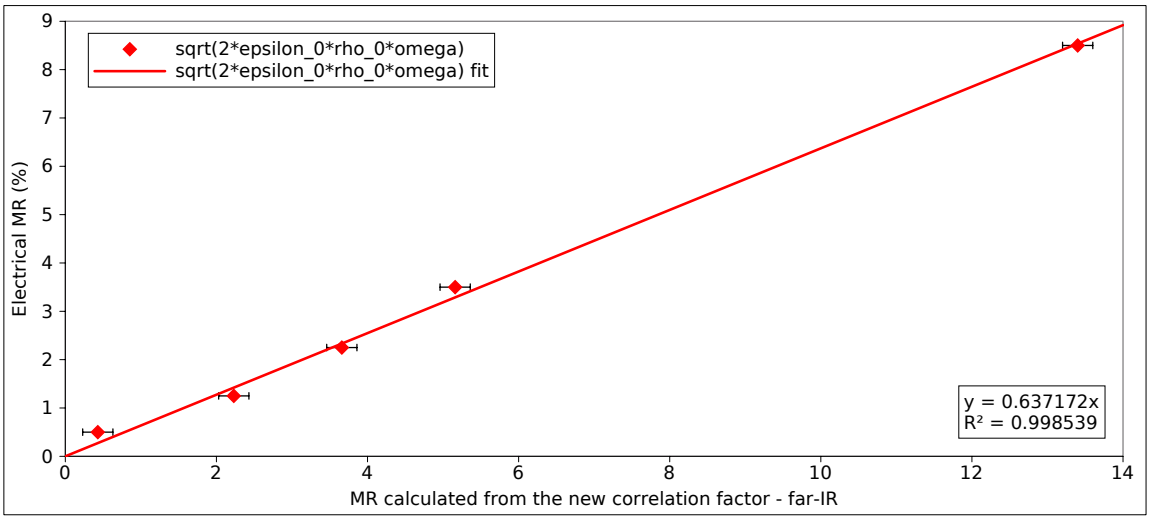

Figure 7.17: Plot of electrical MR against MR estimated from the MRE in the far-IR. The correlation between the MR and the MRE is good in the far-IR, with an almost direct correlation observed. This is the first time the predicted correlation between the MR and the MRE has been observed in the far-IR.

7.5 Conclusions

Experimental MRE spectra were obtained for five spin valves of different MR out to $\sim 50\,\mu$m, the longest wavelength MRE measurement with spectral resolution ever performed. The MRE spectra from the far-IR compliment their mid-IR counterparts well. A significant variation in MRE, and therefore MR, between the spin valves was observed. Previous theoretical work had predicted the MRE spectra to take a $\sqrt{\omega}$ dependence in the far-IR and the experimental spectra appear to follow this predicted trend. Simulated MRE spectra were obtained for all the spin valves, using the reduction in spin polarisation at

the interface due to germanium contamination as a fitting parameter, in order to obtain a lowering of the MR. The simulated spectra demonstrated the same $\sqrt{\omega}$ dependence as the experimental spectra and the fit between the simulated and experimental spectra was excellent. The model used predicted the MR to depend on the electrical properties of the spin valve as MR $\propto \beta_{\mathrm{SAL}}^2$. Taking the MR values for the spin valves and plotting them against the corresponding β_{SAL}^2 values showed that this relationship holds with a constant of proportionality equal to 2.7. The phenomenological correlation formula used for previous mid-IR measurements was shown to result in a poor correlation, with too much error introduced when measuring parameters of the MRE spectra. In the far-IR, the previously untested correlation formula, which is much simpler in form was shown to give an excellent correlation between the electrical MR measurements and the MRE measurements. The correlation is almost direct, of the form $\mathrm{MR}\% = 0.64 \times \mathrm{MRE}\%$. The correlation factor is supposed to be unity, so there is an additional unexpected and unexplained contribution to the correlation. As the measurements and model focussed only on one kind of system it is still unknown whether this analysis can be trivially generalised to other systems. It will also be necessary in future work to resolve the problem of making choices of parameters that reduce the CIP MR when it has been shown to increase. This will involve significantly modifying the current model to include CIP MR or will require the development of a new model. This result provides the first experimental observation of this predicted correlation and demonstrates the promise of far-IR MRE measurements for making accurate, quick, non-invasive MRE measurements, which can also be spatially resolved, unlike electrical measurements of MR.

Chapter 8

Conclusions

IR microspectroscopy and the MRE have been shown to be powerful, versatile techniques for the characterisation of the structural, chemical and magnetic properties of magnetic thin films. The main conclusions drawn from the research performed are now summarised.

A series of Fe_3O_4/MgO thin films of thickness 10, 18, 37, 64, 110 nm were grown by MBE. The shape of the reflectivity spectra of these Fe_3O_4 films was successfully reproduced using a multiple reflection model as a function of thickness, although the reflectivity magnitude is underestimated for all film thicknesses. There was a phonon absorption, predicted to be at 18.5 μm, that occurred at shorter wavelengths in these films, linearly approaching the bulk value as the film thickness increased. This is potentially due to a strained portion of the film near the interface with the substrate resulting in a different phonon energy and therefore position. As more Fe_3O_4 is deposited on top the contribution of the strained portion of the film decreases in importance and the location of the absorption shifts towards the far-IR, reaching the bulk value at ~ 145 nm. This effect could be used in the future to make quick estimates of the thickness of Fe_3O_4, or potentially as a method of identifying and quantifying strain in the lattice.

The MRE spectra of the films could be reproduced with a reasonable conductivity variation and the fitting parameter, used to fit the magnetic field dependence, was $\eta \sim 1$. As the magnetisation of the film was never saturated it is not possible to say that $\eta = 1$ but the close match between the experimental and theoretical magnitudes of the MRE strongly suggests that it is true. An additional shift in the phonon absorption position was also observed to occur in the magnetic field, potentially due to the field slightly modifying the

bond lengths in the lattice, causing a change in the phonon energy. The MRE was demonstrated to be a useful technique for probing the magnetoelectronic properties of iron oxide thin films in a quick and non-destructive way. The next stage of this research would be to uncover the reason why the magnitude of the reflectivity in the simulations is always less than the experimental reflectivity. With this problem overcome, an experiment could be designed where the reflectivity spectra are used to estimate the thickness of some films so determine whether the technique is accurate enough to extract film thickness in this manner. It would also be beneficial to perform electrical MR measurements at a high-field lab in order to determine whether the fitting parameter η is truly unity. It would also be interesting to perform a more detailed TEM analysis of the films to see whether the argument that there is an increase in strain at the interface holds.

Three Fe_3O_4 films were produced by post-oxidation, one by simultaneous-oxidation and one by PLD. Reflectivity spectra from several positions on each sample were recorded on the SMIS beamline at the SOLEIL synchrotron. This was done in an attempt to identify the chemical composition of the samples as well as to determine whether this composition was varying across any of the samples. The sample post-oxidised for 15 minutes was shown to be composed of $\sim$75% iron with $\sim$25% Fe_3O_4 at the surface with VSM and TEM data which was consistent with the spectroscopic results. No variation in composition was detected across the samples. The sample deposited by simultaneous-oxidation showed significant variation in sample composition across the sample. By modelling the reflectivity of the spectrum taken at a point, it was possible to estimate the film composition to be Fe(35%)γ-Fe_2O_3(15%)Fe_3O_4(50%). The trends in the variation of reflectivity across the sample could be reproduced by varying the ratio of iron to iron oxide from 65%/35% to 80%/20%, while keeping the ratio of Fe_3O_4 to γ-Fe_2O_3 constant. The film deposited by PLD had a strong Fe_3O_4 absorption and showed no spatial variation in reflectivity. This was confirmed with TEM data, showing a highly ordered Fe_3O_4 film down to an atomically sharp substrate.

Post-oxidation was shown to be useful only if the thickness of Fe_3O_4 film required is less than $\sim 5\,$nm. Above this thickness the film is not completely oxidised, compromising the magnetic properties of the film. Simultaneous oxidation was shown to produce films which had variable sample composition. It may be possible to grow uniform Fe_3O_4 films with this technique although not with these growth conditions. PLD was shown to produce high quality, uniform Fe_3O_4 thin films that would be ideal for use in devices. IR

microspectroscopy was shown to be a powerful technique for determining the composition and quality of magnetic thin films. This study could be expanded by performing a systematic study of the post-oxidised growth technique to see if it possible to grow magnetite thin films in that manner. It would also be interesting to perform this kind of measurement on a patterned sample, for example, to see if it is possible to determine the composition of individual devices.

A spatial gradient in MR was established across a CoFe/Cu multilayer by attaching a heat sink to one side of the multilayer and heating it in a furnace at 450 °C. Electrical MR measurements showed that the annealing caused a substantial drop in the MR across the sample in a 12 kOe magnetic field. At 900 Oe, the maximum field achievable in the MRE experiments conducted at SOLEIL, the annealed multilayer had a greater MR than the as-deposited multilayer. Through MRE modelling, this was shown to be due to increased layer switching caused by damage to the sample from the annealing. It was also shown that variations in interfacial properties were unable to explain this effect through MRE modelling. A spatial variation in MR was observed across the sample by performing the measurement with an IR microscope, which is impossible with a conventional electrical MR measurement. This was the first time both the spectral resolution needed to model the system and spatial resolution were obtained in a single measurement, showing that the MRE is a powerful technique for remote sensing the MR. This work could be extended by designing a more powerful electromagnet to be incorporated around the microscope, which would facilitate measurements on other materials such as Fe_3O_4, or devices where Fe_3O_4 is a spin injector. It would also be interesting to perform this experiment on a patterned samples to see if the MR of a single device can be determined in this way.

Experimental MRE spectra were obtained for five CoFeGe based spin valves samples with different MR out to $\sim$50 μm, the longest wavelength spectrally resolved MRE measurement ever performed. The MRE data in the far-IR obtained with a bolometer was shown to compliment the mid-IR data collected with an MCT detector. A significant variation in MRE was observed between the samples in both the mid-IR and far-IR, consistent with there being a variation in MR between the samples. Previous theoretical work had shown that the MRE has a $\sqrt{\omega}$ dependence in the far-IR, which should lead to a much stronger correlation between the MR and the MRE than exists in the mid-IR. The $\sqrt{\omega}$ dependence was observed in the experimental MRE spectra in the far-IR. Simulated spectra were produced for the five samples, with the reduction in spin polarisation at the interface

as a fitting parameter, which are in excellent agreement with the experimental spectra. The MRE model used predicted that the MR depends on the electrical properties of the spin valve as MR $\propto \beta^2_{\mathrm{SAL}}$. This dependence was observed and the proportionality constant determined to be MR $= 2.7 \times \beta^2_{\mathrm{SAL}}$, showing that it is possible to probe the underlying physics contributing to the MR of the system with this model. The correlation in the mid-IR was shown to be poor, MR$\% = 3.6 \times$ MRE$\%$, while the correlation in the far-IR was shown to be much better; where the measured MR was 0.64 times the theoretical MR which was close to what was predicted. The correlation factor is shown to be 0.64 for the far-IR correlation, when it is theoretically predicted to be 1. More work needs to be done in order to uncover why there is a constant of proportionality and not a direct correlation as predicted.

The MRE is a powerful technique for the remote sensing of MR and can be used to obtain a diverse array of information about magnetic materials, as has been demonstrated in this thesis. The advances made in this research highlight the advantages of performing IR measurements of MR over electrical measurements of MR; the sample is unharmed, spatial resolution can be obtained and the underlying mechanisms behind the MR can be explored. This serves to demonstrate that the MRE and related magneto-optical techniques are valuable assets for researchers in spintronics and that there is a promising future in using the technique to perform cutting edge research in the field.

Bibliography

1. Žutić, I., Fabian, J., and das Sarma, S. *Rev. Mod. Phys.* **76**(2), 323–410 (2004).
2. Wolf, S. A., Awschalom, D. D., Buhrman, R. A., Daughton, J. M., von Molnár, S., Roukes, M. L., Chtchelkanova, A. Y., and Treger, D. M. *Science* **294**(5546), 1488–1495 (2001).
3. Bader, S. D. and Parkin, S. S. P. *Annu. Rev. Condens. Matter Phys.* **1**, 71–88 (2010).
4. Sanvito, S. *Nat. Mater.* **6**, 803–804 (2007).
5. Sanvito, S. *Chem. Soc. Rev.* **40**, 3336–3355 (2011).
6. Awschalom, D. D. and Flatté, M. E. *Nat. Phys.* **3**, 153–159 (2007).
7. Meier, F., Levy, J., and Loss, D. *Phys. Rev. Lett.* **90**(4), 7901 (2003).
8. Kohda, M., Ohno, Y., Takamura, K., Matsukura, F., and Ohno, H. *Jap. J. App. Phys.* **40**(12), 1274 (2001).
9. Wang, B., Wang, J., and Guo, H. *Phys. Rev. B.* **67**(9), 2408 (2003).
10. Huai, Y. *AAPPS Bulletin* **18**(6), 33–40 (2008).
11. Parkin, S. S. P., Hayashi, M., and Thomas, L. *Science* **320**(5873), 190–194 (2008).
12. Kryder, M. H., Gage, E. C., McDaniel, T. W., Challener, W. A., Rottmayer, R. E., Ju, G., Hsia, Y.-T., and Erden, M. F. *Proc. IEEE* **96**(11), 1810–1835 (2008).
13. Baibich, M. N., Broto, J. M., Fert, A., Van Dau, F. N., Petroff, F., Etienne, P., Creuzet, G., Friederich, A., and Chazelas, J. *Phys. Rev. Lett.* **61**, 2472–2475 (1988).
14. Binasch, G., Grünberg, P., Saurenbach, F., and Zinn, W. *Phys. Rev. B* **39**, 4828–4830 (1989).

15. Thompson, S. M. *J. Phys. D* **41**(9), 093001 (2008).

16. Mott, N. F. *Proc. Roy. Soc. Lond. A* **156**, 368–382 (1936).

17. Hirota, E., Sakakima, H., and Inomata, K. *Giant Magneto-resistance Devices*. Springer-Verlag Berlin, illustrated edition, (2002).

18. Daughton, J. M. and Chen, Y. J. *IEEE Trans, Mag.* **29**(6), 2705 (1993).

19. Peng, X., Kolbo, P., Nikolaev, K., Chen, S., Wang, Z., Boonstra, T., Anderson, P., Kalderon, S., Czoschke, P., Morrone, A., Dimtrov, D., Xue, S., and Chen, Y. *J. Magn. Magn. Mater.* **321**(12), 1889–1892 (2009).

20. Hill, A. F., Nor, A., Birtwistle, J. K., and Parker, M. R. *Sens. Actuators, A* **59**(30), 37 (1997).

21. Fert, A. and Jaffrès, H. *Phys. Rev. B* **64**, 4420 (2001).

22. Granovsky, A., Sukhorukov, Y., Gan'shina, E., and Telegin, A. Springer Series in Materials Science, 1st edition, (2013).

23. Jacquet, J. and Valet, T. *MRS Symp. Proc.* **348**, 477 (1995).

24. Caicedo, J. M., Arora, S. K., Ramos, R., Shvets, I. V., Fontcuberta, J., and Herranz, G. *New J. Phys.* **12**, 103023 (2010).

25. Telegin, A. V., Bessonov, V. D., and Sukhorukov, Y. P. *J. Supercond. Nov. Magn.* **26**(5), 1437–1440 (2013).

26. Lobov, I. D., Kirillova, M. M., Makhnev, A. A., Romashev, L. N., and Ustinov, V. V. *Phys. Rev. B* **81**, 134436 (2010).

27. Bozec, D., Kravets, V. G., Matthew, J. A. D., Thompson, S. M., and Kravets, A. F. *J. Appl. Phys.* **91**, 8795 (2002).

28. Worledge, D. C. and Trouilloud, P. L. *Appl. Phys. Lett.* **83**(1), 84–86 (2003).

29. Stirk, S. M., Thompson, S. M., Mennicke, R. T., Matthew, J. A. D., and Lee, A. F. *Appl. Phys. Lett.* **88**(2), 022502 (2006).

30. Vopsaroiu, M., Bozec, D., Matthew, J. A. D., Thompson, S. M., Marrows, C. H., and Perez, M. *Phys. Rev. B* **70**, 214423 (2004).

31. Mennicke, R. T., Bozec, D., Kravets, V. G., Vopsaroiu, M., Matthew, J. A. D., and Thompson, S. M. *J. Magn. Magn. Mater.* **303**(1), 92–110 (2006).

32. Harrison, R. J., Dunin-Borkowski, R. E., and Putnis, A. *Proc. Natl. Acad. Sci. U.S.A.* **99**(26), 16556–16561 (2002).

33. Hibma, T., Voogt, F. C., Niesen, L., van der Heijden, P. A. A., De Jonge, W. J. M., Donkers, J. J. T. M., and Van der Zaag, P. J. *J. Appl. Phys.* **85**(8), 5291–5293 (1999).

34. Yanase, A. and Siratori, K. *J. Phys. Soc. Jap.* **53**(1), 312–317 (1983).

35. Eerenstein, W. *Spin-Dependent Transport Across Anti-Phase Boundaries in Magnetite Films*. PhD thesis, Materials Science Centre, Rijksuniversiteit Groningen, (2003).

36. Eerenstein, W., Palstra, T. T. M., Saxena, S. S., and Hibma, T. *Phys. Rev. Lett.* **88**(24), 247204 (2002).

37. Gao, Y., Kim, Y. J., and Chambers, S. A. *J. Mater. Res.* **13**(7), 2003–2014 (1998).

38. Jiles, D. C. *Introduction to Magnetism and Magnetic Materials*. Taylor & Francis Inc., 2nd edition, (1998).

39. Anderson, P. W. *Phys. Rev.* **79**(2), 350–356 (1950).

40. Margulies, D. T., Parker, F. T., Rudee, M. L., Spada, F. E., Chapman, J. N., Aitchison, P. R., and Berkowitz, A. E. *Phys. Rev. Lett* **79**(25), 5162–5165 (1997).

41. Blakemore, J. S. *Solid State Physics*. Cambridge University Press, 2nd edition, (1985).

42. Huang, D. J., Chang, C. F., Jeng, H.-T., Guo, G. Y., Lin, H.-J., Wu, W. B., Ku, H. C., Fujimori, A., Takahashi, Y., and Chen, C. T. *Phys. Rev. Lett.* **93**, 077204 (2004).

43. Arras, R., Calmels, L., and Warot-Fonrose, B. *J. Phys.: Conf. Ser.* **200**(7), 2008 (2010).

44. Julliere, M. *Phys. Lett. A* **54**(3), 225 – 226 (1975).

45. Tsymbal, E. Y. *Handbook of Spin Transport and Magnetism*. Taylor & Francis Ltd, 1st edition, (2011).

46. Versluijs, J. J., Bari, M. A., and Coey, J. M. D. *Phys. Rev. Lett.* **87**(2), 026601 (2001).

47. Huang, D. J., Chang, C. F., Chen, J., Tjeng, L. H., Rata, A. D., Wu, W. P., Chung, S. C., Lin, H. J., Hibma, T., and Chen, C. T. *J. Magn. Magn. Mater.* **239**(1-3), 261–265 (2002).

48. Wang, D., Anderson, J., and Daughton, J. M. *IEEE Trans. Mag.* **33**(5), 3520 (1997).

49. Larson, D. J., Clifton, P. H., Tabat, N., Cerezo, A., Petford-Long, A. K., Martens, R. L., and Kelly, T. F. *Appl. Phys. Lett.* **77**(5), 726–728 (2000).

50. Dieny, B. *J. Magn. Magn. Mater.* **136**, 335–359 (1994).

51. Meiklejohn, W. H. Bean, C. P. *Phys. Rev.* **105**(3), 904–913 (1957).

52. Giri, S., Patra, M., and Majumdar, S. *J. Phys.: Condens. Matter* **23**(7), 073201 (2011).

53. Tsang, C., Fontana, R. E., Lin, T., Heim, D. E., Speriosu, V. S., Gurney, B. A., and Williams, M. L. *IEEE Trans. Mag.* **30**(6), 3801–3806 (1994).

54. Seyama, Y., Tanaka, A., and Oshiki, M. *IEEE Trans. Magn.* **35**(5), 2838 (1999).

55. Lee, H., Wang, Y.-H. A., Mewes, C. K. A., Butler, W. H., Mewes, T., Maat, S., York, B., Carey, M. J., and Childress, J. R. *Appl. Phys. Lett.* **95**(8), 082502–082502–3 (2009).

56. Grant, I. S. and Phillips, W. R. *Electromagnetism*. Wiley, 2nd edition, (2007).

57. Hecht, E. *Optics*. Addison Wesley, 4th edition, (2002).

58. Fox, M. *Optical Properties of Solids*. Oxford University Press, 1st edition, (2001).

59. Jacquet, J. C. and Valet, T. *MRS Proceedings* **384**, 477 (1995).

60. Kittel, C. *Introduction to Solid State Physics*. Wiley, 8th edition, (2005).

61. Degiorgi, L., Wachter, P., and Ihle, D. *Phys. Rev. B* **35**, 9259 (1987).

62. Ahn, J. S., Choi, H. S., and Noh, T. W. *Phys. Rev. B* **53**, 10310 (1996).

63. McIntyre, J. D. E. and Aspnes, D. E. *Surf. Sci.* **24**(2), 417 – 434 (1971).

64. Naughton, J. *A Surface Science and Thin Film Approach to the Development of Functional Materials*. PhD thesis, Department of Chemistry and Department of Physics, University of York, (2012).

65. Cabrera, L. and Mott, N. F. *Rep. Prog. Phys.* **12**, 163–184 (1949).

66. Lide, D. R. *Handbook of Chemistry and Physics*. CRC Press, 88th edition, (2008).

67. Darken, L. S. and Gurry, R. W. *J. Am. Chem. Soc.* **68**(5), 798–816 (1946).

68. Stirk, S. M., Thompson, S. M., and Matthew, J. A. D. *Appl. Phys. Lett.* **86**(10), 102505 (2005).

69. Choi, H. S., Ahn, J. S., Jo, W., and Noh, T. W. *J. Korean Phys. Soc.* **28**, 636 (1995).

70. Šimša, Z. *Phys. Status Solidi B* **96**, 581 (1979).

71. Ihle, D. and Lorenz, B. *J. Phys. C: Solid State Phys.* **19**, 5239–5251 (1986).

72. Zhang, J., Tan, P. H., Zhao, W. J., Lu, J., and Zhao, J. H. *J. Raman Spectrosc.* **42**, 13881391 (2011).

73. Gilks, D., Lari, L., Cai, Z., Cespedes, O., and Gerber, A. *J. Appl. Phys.* **113**, 17B107 (2013).

74. Fonin, M., Dedkov, Y. S., Pentcheva, R., Rũdiger, U., and Gũntherod, G. *J. Phys.: Condens. Matter* **19**, 315217 (2007).

75. Cheng, J. P., McCombe, B. D., Shi, J. M., Peeters, F. M., and Devreese, J. T. *Phys. Rev. B* **48**, 7910 (1993).

76. Matsuzaki, K., Lazarov, V. K., Lari, L., Hosono, H., and Susaki, T. *J. Phys. D: Appl. Phys.* **46**, 022001 (2013).

77. Wang, L., McMahon, W. J., Liu, B., Wu, Y. H., and Chong, C. T. *Phys. Rev. B* **69**, 214403 (2004).

78. Wang, L., Qiu, J. J., McMahon, W. J., Li, K. B., and Wu, Y. H. *Phys. Rev. B* **69**, 214402 (2004).

79. Xiao, J. Q., Jiang, J. S., and Chien, C. L. *Phys. Rev. Lett.* **68**(25), 3749–3752 (1992).

80. Reilly, A. C., Park, W., Slater, R., Ouaglal, B., Loloee, R., Pratt, Jr, W. P., and Bass, J. *J. Magn. Magn. Mater.* **195**(2), L269 – L274 (1999).

81. Pratt, Jr, W. P., Yang, Q., Henry, L. L., Holody, P., Chiang, W. C., and Schroeder, P. A. *J. Appl. Phys.* **79**(8), 5811–5815 (1996).

82. Mennicke, R. T., Matthew, J. A. D., and Thompson, S. M. *IEEE Trans. Magn.* **42**(10), 2627 –2629 (2006).

83. Maat, S., Carey, M. J., and Childress, J. R. *Appl. Phys. Lett.* **93**(14), 3505 (2008).

84. Mennicke, R. T. *Sensing Magnetotransport*. PhD thesis, Department of Physics, University of York, (2007).